UNIVERSITÀ DEGLI STUDI DI PADOVA

Dipartimento di Fisica e Astronomia "Galileo Galilei"

Master Degree in Physics

Final Dissertation

Modelling of plasma expansion and interpretation of measured profiles in a negative ion source

Thesis supervisor

Dr. Gianluigi Serianni

Thesis co-supervisor

Dr. Emanuele Sartori

Candidate

Valeria Candeloro

Academic Year 2019/2020

Abstract

ITER is an international project aiming to demonstrate the feasibility of energy production through controlled thermonuclear fusion. In order to trigger the required fusion reactions, an extremely hot plasma has to be confined for a sufficiently long time. One of the primary methods for plasma heating is the Neutral Beam Injection (NBI), which amounts to depositing additional power in the plasma by means of a highly energetic neutral beam, obtained through the neutralization of a precursor ion beam. The ITER NBI will employ radiofrequency (RF) driven ion sources to generate and extract negative ions; this kind of source displays some important advantages, such as low need for maintenance and moderate energy consumption, even though the research on the application of this technology to fusion experiments is less mature than the more consolidated arc-filament discharge. In this framework, the main purpose of this thesis project is the investigation of the most important physical processes underlying the plasma generation and expansion in a RF negative ion source, with a particular focus on plasma uniformity: indeed, the presence of a magnetic filter field inevitably introduces drift motions inside the source, ultimately affecting several properties of the extracted beam such as current intensity, stability and convergence. A pre-existent Particle-In-Cell simulation code was adapted and developed so as to study the plasma generation and expansion mechanisms in the SPIDER source. The numerical results have been compared with recent experimental measurements obtained with movable electrostatic probes, with the intention of both validating the code and providing an interpretation for the experimental trends, clarifying the relations between plasma properties and variations of the background gas pressure, of the magnetic field and of the voltages of the plasma-facing electrodes.

Sommario

ITER è un progetto internazionale volto a dimostrare la fattibilità della produzione di energia tramite fusione nucleare termocontrollata. Affinché le reazioni di fusione possano avere luogo, è necessario confinare un plasma ad alta temperatura per un tempo sufficientemente lungo. Gli iniettori di neutri sono uno dei metodi più diffusi per il riscaldamento del plasma: in questo caso si utilizza un fascio di neutri ad alta energia, ottenuto tramite neutralizzazione di un fascio precursore di ioni, per depositare potenza nel plasma stesso. Il progetto di ITER prevede sorgenti a radiofrequenza (RF) per la produzione e l'estrazione di ioni negativi; questa tecnologia porta molti vantaggi, come il ridotto bisogno di manutenzione e un moderato consumo di energia ma, d'altra parte, la ricerca sulla sua applicazione a esperimenti di fusione nucleare è ancora in evoluzione. In questo contesto, l'obiettivo principale di questo lavoro di tesi è lo studio dei processi fisici alla base della generazione ed espansione del plasma in una sorgente di ioni negativi a radiofrequenza, con particolare attenzione all'uniformità di plasma: infatti, la presenza di un filtro magnetico introduce inevitabilmente dei moti di deriva all'interno della sorgente e, di conseguenza, comporta l'alterazione di alcune proprietà del fascio come l'intensità di corrente, la stabilità ed anche la convergenza. Un codice Particle-In-Cell già esistente è stato adattato e sviluppato con l'obiettivo di studiare i meccanismi di generazione ed estrazione di plasma nella sorgente SPIDER. I risultati numerici sono stati confrontati con misure sperimentali ottenute tramite sonde elettrostatiche mobili, con l'obiettivo di validare il codice e di analizzare le correlazioni tra le proprietà del plasma e variazioni della pressione del gas di background, del campo magnetico e del potenziale della griglie esposte al plasma.

Contents

Chapter 1

Introduction

A brief introduction to controlled thermonuclear fusion and a concise overview of the currently undergoing experiments are presented in this chapter in order to provide the framework of this thesis. Finally, the motivations and aims of this work are explained.

1.1 The energy problem

Global energy consumption has been growing exponentially since the middle of the 19th century. Together with the industrial development, our life-style is the main reason for the increasing energy demand. As can be seen in Figure 1.1, almost half of the needed energy is still produced from oil or coal; the employment of more sustainable technologies has also grown in the past decade, although they are not yet capable of satisfying the global energy request.

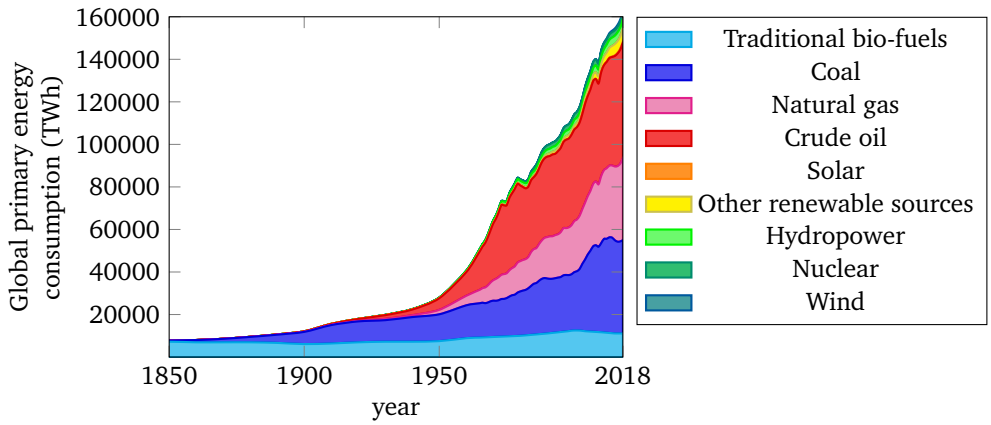

Figure 1.1: Global energy consumption divided by source type. *Source: BP Statistical Review of World Energy*[1].

Human activities can have a considerable impact on the environment, as can be seen in Figure 1.2. The extended use of non-renewable sources causes substantial greenhouse gas emissions, negatively affecting the Earth's climate: for this reason, it is important to find a more efficient and eco-compatible way of producing energy.

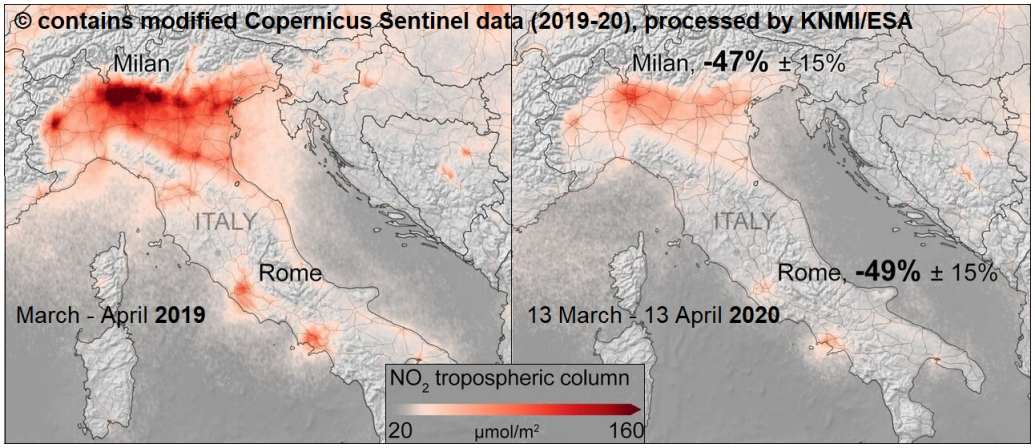

Figure 1.2: NO_2 emission decrease during the COVID-19 emergency. As a result of the early 2020 lockdown, the average nitrogen dioxide concentration has halved with respect to 2019. *Source: European Space Agency*[2].

1.2 Why nuclear fusion?

The research on thermonuclear fusion began in the 1950s with the construction of T1, the first *tokamak* device.

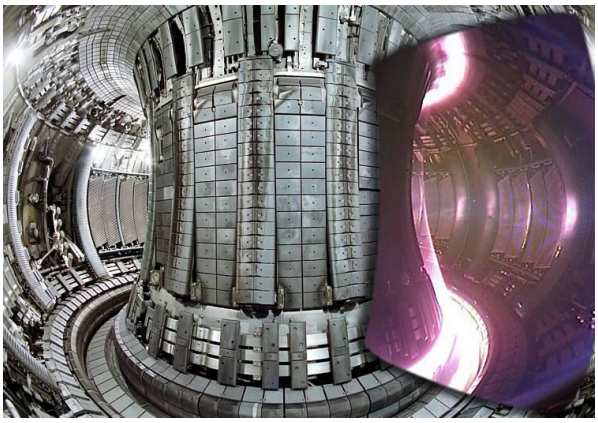

Figure 1.3: The JET Tokamak with (right side) and without plasma. Photo: CCFE, JET.

These machines are able to confine a highly energetic plasma in a toroidal chamber thanks to the action of strong electromagnetic fields, allowing fusion reactions to take place. In order to produce a significative amount of energy, plasma particles need to be confined for a sufficiently long time and, furthermore, energy losses must be covered.

Nuclear fusion could play a key role in the world energy scenario as it might considerably contribute to the global energy production and, more importantly, its impact on the environment would be extremely reduced with respect to today's major energy sources both during operation and in case of accidents.

[2] The word "tokamak" is a Russian acronym for *toroidal chamber with magnetic coils*.

1.3 The ITER project

ITER[3] (**I**nternational **T**hermonuclear **E**xperimental **R**eactor) will be the largest tokamak ever built, aiming to prove the feasibility of large-scale energy production: indeed, it will be able to generate 500 MW of power from 50 MW of input power.

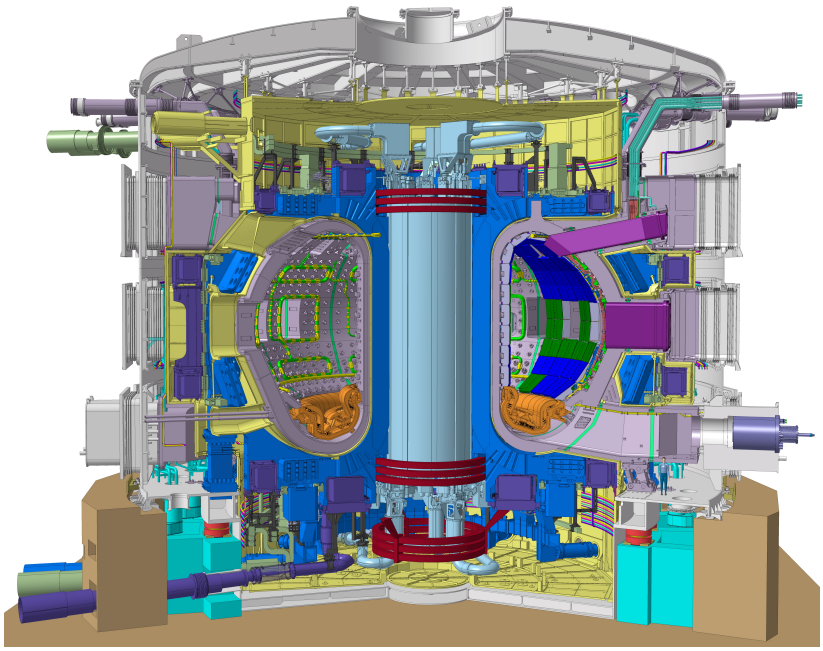

Figure 1.4: Technical design of ITER tokamak (®ITER Design Office, Jan 2013).

A deuterium-tritium (D-T) plasma will be confined in the ITER tokamak through superconducting magnets that will be able to generate a maximum magnetic field of 11.8 T. Deuterium is a widespread hydrogen isotope that can be easily retrieved on Earth, whereas tritium is a radioactive hydrogen isotope which is available in much smaller quantities: for this reason, one of the ITER goals is to test the feasibility of on-site tritium production[4]. The energy will be generated by employing the following D-T fusion reaction

$$^2\mathrm{D} + {}^3\mathrm{T} \rightarrow {}^4\mathrm{He}\,(3.5\,\mathrm{eV}) + n\,(14.1\,\mathrm{eV}) \tag{1.1}$$

which requires plasma particles to have energies ≥ 20 keV. In order to ensure long run operations, the plasma temperature needs to be maintained at high values; in other words, plasma particles need to be repeatedly heated and loss terms need to be counterbalanced. To fulfil these requirements, the ITER project foresees three methods for plasma heating, namely:

- Ohmic heating, which can be defined as "internal" heating as it is provided by the poloidal plasma current induced by the tokamak coils. This method is less effective as the plasma temperature increases, since the plasma resistivity η is proportional to $T^{-3/2}$.

- Radio-Frequency heating, which instead is an "external" heating method consisting in the excitation of the electron or ion cyclotron resonance (ECR or ICR) modes through electromagnetic radiation. In the first case plasma ions are directly heated, whereas in the second case the heated electrons will transfer energy to the ions through collisions. The lower hybrid (LH) mode or low frequency Alfvèn waves can also be excited.
- Neutral beam heating, that is another external heating method as further explained in Section 1.3.1.

1.3.1 Neutral Beam Injection

Neutral Beam Injection (NBI) is an external plasma heating technique which requires highly-energetic neutral particles to enter the plasma chamber, where they are ionized by the plasma particles and they subsequently transfer their kinetic energy to the plasma itself by collisions.

It is important to consider a neutral beam as the latter is not affected by the electromagnetic fields, therefore it can travel longer distances and, more importantly, it can penetrate the plasma confinement. Energetic neutral beams are created through the neutralization of a precursor ion beam which can be composed either of positive or negative ions. The principal components of a NBI system are:

- Ion source, where the chosen ions are generated by a low pressure cold plasma;
- Accelerating column, where the extracted ions are accelerated by properly polarised grids;
- Neutralization chamber, where the accelerated ions interact with a previously injected gas and they are subsequently neutralized;
- Residual Ion Dump (RID), where the remaining ions are removed from the obtained neutral beam.

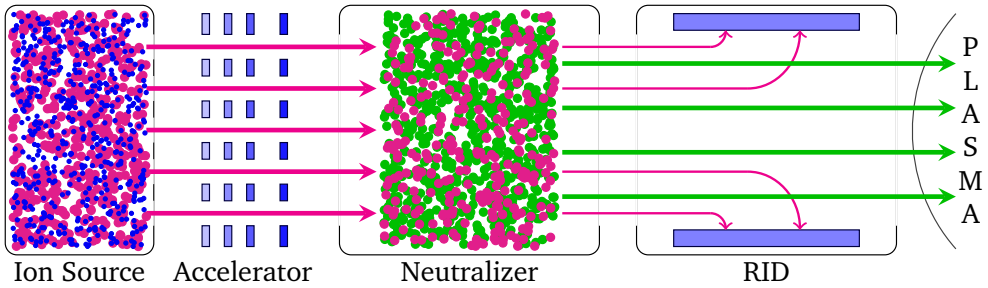

Figure 1.5: Scheme of a NBI system. Magenta and blue points represent ions and electrons respectively, green points instead represent fast atoms.

Positive-NBI is much more simple than Negative-NBI from the technical point of view: in fact, as the accelerated ions carry a positive charge, there is no risk of simultaneously extracting plasma electrons. In the N-NBI case instead the amount of co-extracted electrons is not negligible and it constitutes an important issue that has to be addressed. However, negative ions feature a much higher neutralization rate

as the bond energy of the additional electron is only 0.75 eV and, for this reason, N-NBI is much more efficient.

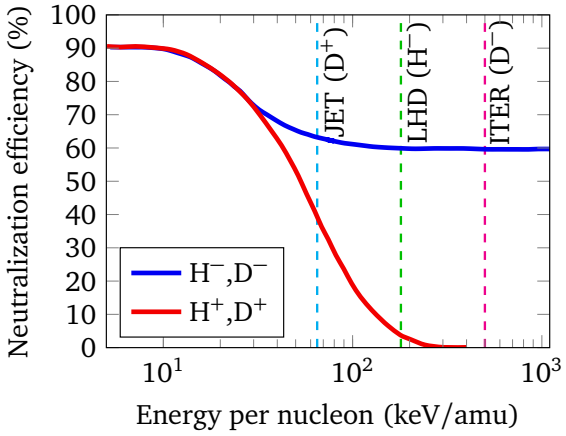

Figure 1.6: Neutralization efficiency of H,D ions as a function of the neutralized atom energy per nucleon[5].

The ITER project includes two extremely powerful N-NBI for plasma heating. The neutral beam needs to reach 1 MeV energy, hence the choice of using negative ions: as can be seen from Figure 1.6, the neutralization efficiency for positive ions is extremely low for ITER-relevant energies. Some specific design parameters for the ITER NBI are listed in Table 1.1.

Parameter	Value
Beam energy	870 keV H_2; 1000 keV D_2;
Max source filling pressure	0.3 Pa
Beamlet divergence	$\leq$ 7 mrad
Accelerated current	46 A H_2; 40 A D_2
Beam-on time	1000 s H_2; 1 h D_2
Co-extracted electron fraction	$<$ 0.5 H_2; $<$ 1 D_2

Table 1.1: Design parameters for the ITER NBI system.

The extracted current will be of 40 A, and the injected beam needs to be extremely focused: these requirements have never been simultaneously satisfied in past experiments.

1.3.2 Ion sources for fusion experiments

The most used ion sources for NBI systems are arc sources and Radio-Frequency (RF) driven sources. The main difference between these two technologies is the electron heating mechanism; in both cases, the plasma is generated through electron impact ionization of the background gas.

Experiment	Used species	Source type
JET	H^+/D^+	Arc source
JT-60U	H^+/D^+ and H^-/D^-	Arc source
TFTR	H^+/D^+	Arc source
LHD	H^-	Arc source
ASDEX	H^+/D^+	Arc/RF source
W7-X	H^+/D^+	RF source
ITER	H^-/D^-	RF source

Table 1.2: Source types used in currently undergoing fusion experiments.

As can be seen from Table 1.2, the arc technology is significantly widespread and its understanding has been fine-tuned and strengthened over the years for both positive and negative ion production. On the other hand, the research on RF sources as a significant alternative to filament-based sources has only recently started: nevertheless, the ITER NBI system will employ this kind of source as it provides some important advantages (Section 2.1.2).

1.3.3 Neutral Beam Test Facility (NBTF)

The Neutral Beam Test Facility (NBTF)[6] aims at investigating all the possible issues related to the ITER neutral beam injectors, before the actual installation in the ITER tokamak. The facility is hosted at Consorzio RFX, in Padova, where two experiments are currently underway:

- SPIDER (**S**ource for the **P**roduction of **I**ons of **D**euterium **E**xtracted from a **R**F plasma), that is the full-scale prototype of the ITER negative ion source. SPIDER has been operating since 2018 and it is in its optimization phase;
- MITICA (**M**egavolt **ITER** **I**njector and **C**oncept **A**dvancement), i.e. the full-scale prototype of the entire neutral beam injector. MITICA is still under construction.

1.4 Thesis motivation

The aim of this thesis work is the investigation and analysis of the physical processes involved in a negative ion source, with a particular focus on the plasma properties, via numerical simulations. More precisely, a two-dimensional PIC-MCC code has been developed to reproduce the plasma generation and expansion processes, while comparing the obtained results with the experimental measurements performed in SPIDER.

One of the main purposes is to investigate the non-uniformities arising in the SPIDER source, with the aim of defining which physical processes have the strongest influence and, possibly, how they can be countered. The comparison between the measured properties and the simulation results will serve as both a validation and a benchmark for the code, ultimately refining the analysis.

The PIC-MCC algorithm allows to follow the particle motion and to extract the plasma properties. It is therefore a useful tool to analyse the plasma density and temperature profiles inside the source and to provide an estimation of the drift motions, which are strictly related to non-uniformities. Furthermore, it is possible to achieve a more comprehensive understanding of the acquired data and also to foresee the source behaviour in inaccessible experimental conditions, as the simulation results allow to make up for possible lack of information caused by technical or physical limitations.

PIC-MCC refers to **P**article-**I**n-**C**ell-**M**onte **C**arlo **C**ollisions.

Chapter 2

Negative ion sources for fusion applications

The main features of ion sources for fusion experiments and the most important differences between radio-frequency driven and arc-based sources are described within this chapter. Some insights on the physical processes taking place in a RF source for the production of negative ions are provided. The final Section is dedicated to the SPIDER experiment.

2.1 Ion sources

Ion sources are the primary components of neutral heating systems: indeed, most of the extracted beam properties such as its intensity, shape, emittance and also the operation method (continuous or pulsed) are determined by the source itself. For this reason, the characterization of the source operation and the improvement of its technical limits are of utmost importance with a view to fulfil the ITER NBI requirements.

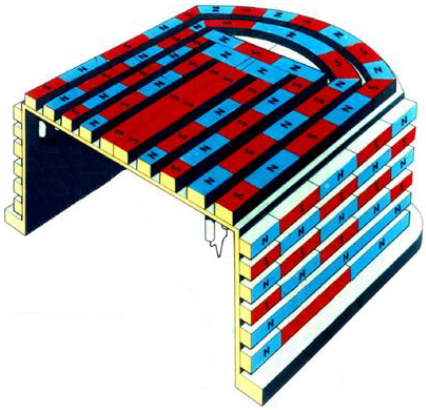

Figure 2.1: Permanent magnets multipole configuration in the JET ion source.

Fusion relevant sources are basically composed of a plasma chamber, where a cold hydrogen or deuterium plasma is generated by ionization of a neutral gas, and an ion extractor. The source plasma is magnetically confined by some permanent magnets attached on the outer vessel surfaces, forming a multipole configuration as the one shown in Figure 2.1. The confining field intensity is stronger in front of the walls, then decreasing towards the plasma bulk in very short distances.

In order to sustain the discharge, plasma electrons need to be maintained at relatively high temperatures. Two kinds of sources can be distinguished on the basis of the electron heating mechanism:

- Filament-based sources, in which fast electrons are obtained by thermionic emission of appropriately heated filaments;
- Radiofrequency (RF) sources, in which electrons are heated by oscillating electromagnetic fields.

The involved physics is significantly different depending on the source type, as further explained in the following sections.

2.1.1 Filament-based sources

Arc discharges are possibly the most direct way to trigger gas ionization. Metallic filaments are heated up to $T \propto 1000\,\mathrm{K}$ in such a way that a fraction of their electrons gain enough thermal energy to overcome the potential barrier set by the work function of the filament material. This is indeed a threshold process called *thermionic effect* and the extracted current density is given by Richardson's law

$$j = A T^2 \exp\left\{-\frac{e\phi}{k_B T}\right\} \tag{2.1}$$

where ϕ is the work function, T is the absolute temperature, A is expressed in $[\mathrm{Am^{-2}K^{-2}}]$ and its value depends on the filament material. Among all metals, tungsten (W) is preferable as its fusion temperature is very high, thus it can resist a strong thermal stress and release many electrons.

Filaments are heated either by a direct or an alternating current $\propto 100\,\mathrm{A}$. Some of the primary electrons are deflected by collisions with the gas molecules. If the applied voltage between the filament (hot cathode) and the source vessel (anode) is large enough, these electrons acquire sufficient kinetic energy to escape from the filament and to ionize the gas, generating the plasma. As soon as the plasma density increases, a sheath forms around the filament and the following emitted electrons will face a stronger local field, so they will easily leave the arc region.

Although they are very simple, arc sources do have some drawbacks such as the high need of maintenance and impurity production, since filaments can break and they are exposed to the plasma itself. Furthermore, they require a significant amount of energy as they need to reach very high temperatures.

2.1.2 Radio-frequency sources

The ionizing discharge in RF sources is induced by an external coil, also called *antenna*, wrapped around the source vessel. The antenna acts as the primary circuit of a transformer: when an oscillating current flows through the coil, a time-varying electromagnetic field is induced in the plasma, which instead can be thought of as the secondary circuit. The electrons are then accelerated by the electric field.

The main advantage of RF sources is the lower need for maintenance: this is extremely important for reliability, as filaments are subject to wear and they are more liable to sudden break-up. Furthermore, the arc response to current variations is slowed down by the thermal inertia of the filament, whereas the plasma response to injected power variations in RF sources is much faster.

2.2 Physics of RF based negative ion sources

As already said in the introduction, ITER will employ RF driven sources for the production of negative ions, despite the deeper knowledge acquired for arc sources and for positive ion RF sources; indeed, the beam energy required for the ITER NBI can be obtained only with a negatively charged precursor ion beam and, still in the ITER case, long run operations would not be possible with arc sources as the filaments should be much too frequently replaced, increasing the maintenance downtime. Figure 2.2 shows a simplified scheme of a RF negative ion source.

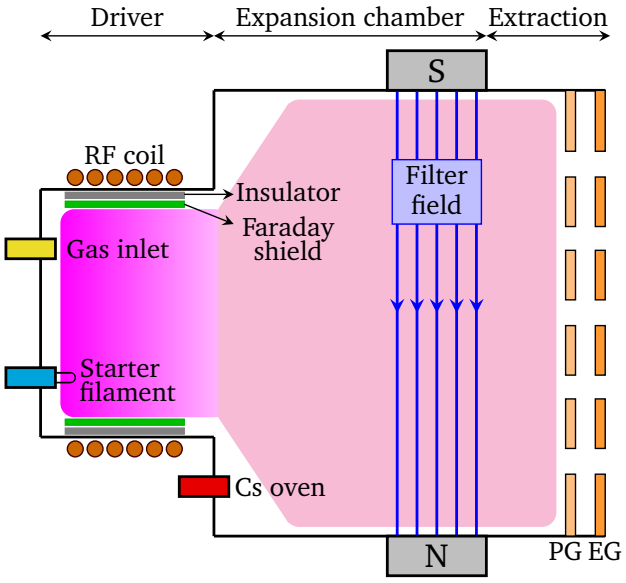

Figure 2.2: Basic example of a RF negative ion source.

The main source parameters are:

- Injected RF power, that affects both plasma generation and heating;
- RF frequency, i.e. the operating frequency of the RF generators supplying the antenna;
- Gas pressure, that determines the plasma generation rate and has to be chosen with the aim to prevent Paschen discharges.

2.2.1 Plasma generation

In RF sources, the plasma generation takes place in a defined region of the vessel called *driver*. A coil is wrapped around an insulating layer lying on the outer surface of the driver walls; as soon as an oscillating current flows along the coil, an electromagnetic field is induced into the plasma. A Faraday shield is usually present to prevent capacitive coupling between the coil and the plasma itself (see Figure 2.3). The coil is supplied by a RF generator and the injected power P_{inj} ranges from 50 kW to 100 kW for fusion experiments. Roughly speaking, the higher P_{inj}, the denser and hotter the plasma; however, possible losses due to the transmission

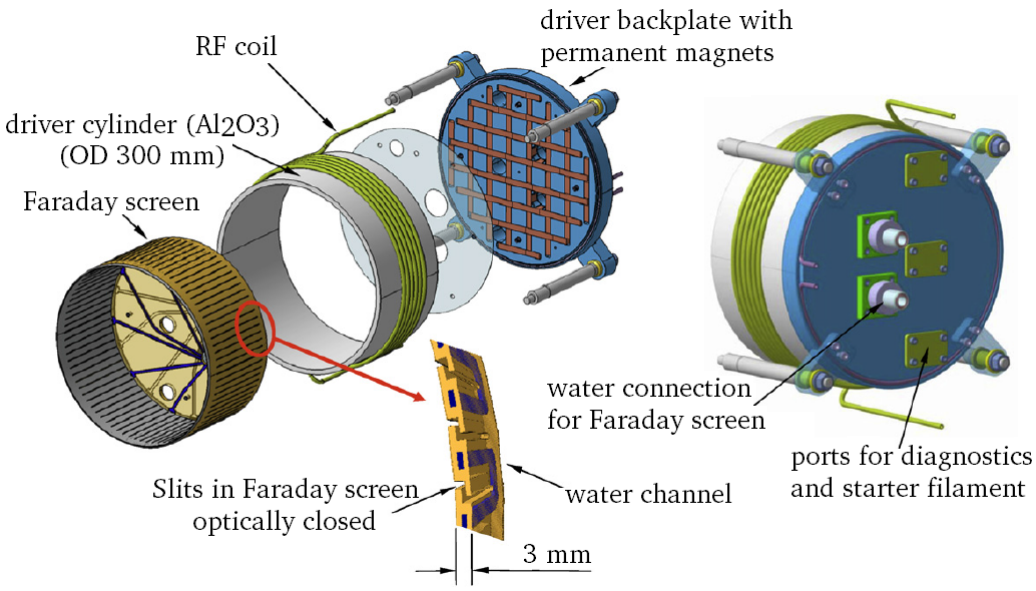

Figure 2.3: Exploded view of the SPIDER drivers.

line or to resistive components of the matching RF network should be taken into account[7]. The effectively absorbed power can be defined as

$$P_{abs} = P_{inj} - R_{loss} I_{rms}^2 = \eta P_{inj} \tag{2.2}$$

where R_{loss} is an effective resistance, I_{rms} is the root mean square value of the induced current and η can be defined as the power transfer efficacy. The induced field oscillates with the same frequency of the generator, ν_{RF}, that is approximately 1 MHz; this choice is dictated by the need to excite plasma electrons also at the early stages of the discharge, when the plasma density is not high: indeed, for densities of the order of $10^{12}\,\mathrm{m}^{-3}$, the plasma electron frequency f_{pe} is roughly 10 MHz. If $\nu_{RF} > f_{pe}$, the RF field will propagate without being absorbed by the plasma.

The induced magnetic field is directed along the driver axis, whereas the electric field oscillates along the poloidal direction. As the plasma density increases, the induced fields are more and more localized towards the outer region of the plasma: this phenomenon is called skin effect[8]. The field intensity decays exponentially towards the plasma bulk over a characteristic length, δ, called *skin depth*. The electrons in the outer region are accelerated by the poloidal electric field and their motion is periodically reversed with frequency ν_{RF}: this is a de-maxwellizing process which is counterbalanced by the $e^- - e^-$ Coulomb collisions, that indeed favour thermalization (see Appendix A). For low pressures, the two processes are approximately balanced and the measured EEDF (Electron Energy Distribution Function) was found to follow a double Maxwellian distribution[9], with a high energy tail due to the inductive coupling.

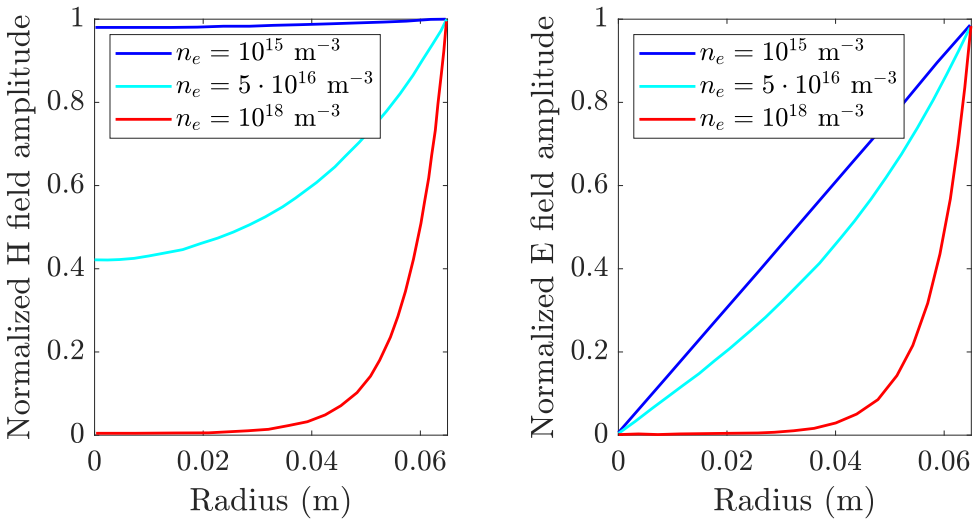

Figure 2.4: Normalised complex amplitudes of the E, H fields as a function of the distance from the plasma bulk[8].

As can be seen from Figure 2.2, some starter filaments are also included: the latter are needed to generate the primary electrons, that are subsequently accelerated by the induced electric field. As the plasma density increases and electrons are heated, new plasma particles are created by electron impact ionization of the background gas, that is a threshold process which requires T_e to be larger than 10 eV.

2.2.2 Plasma expansion and negative ion production

The generated plasma will flow out of the driver region, completely filling the *expansion chamber*. The expansion mechanism is mainly driven by the density gradient, by the action of the electromagnetic field and by the plasma-gas interaction. The obtained plasma should be as "uniform" as possible in order to improve the overall source performance; however, this requirement is not completely satisfied for several reasons, as further described in Section 2.3.

The beam ions are created within the expansion region. Two main processes can be distinguished, namely *volume* and *surface* production. In the first case, negative ions are generated by collisions in the plasma bulk, whereas in the second case they are produced by fast H/D positive ions or atoms impacting on the source walls. The main channel for volume production is the electron dissociative attachment (DA)

$$e^- + H_2[v > 3] \rightarrow H + H^- \tag{2.3}$$

that involves vibrationally excited molecules with $v > 3$, produced by fast electron impact. These molecules account for approximately 3% of the entire population[10]. On the other hand, one of the main channels for negative ion destruction is electron detachment (ED)

$$e^- + H^- \rightarrow e^- + H + e^- \tag{2.4}$$

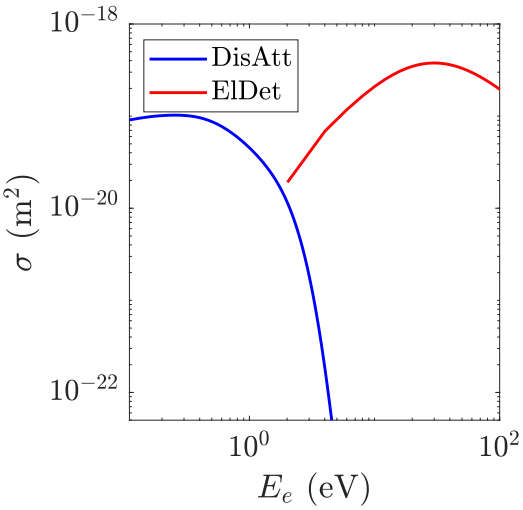

Figure 2.5: Cross sections of (e^-, H_2) dissociative attachment and (e^-, H^-) electron detachment.

The cross sections of DA and ED processes are comparable, even though they are related to different electron energies (see Figure 2.5): this implies that the produced negative ions are easily destroyed by fast electrons and, as a consequence, it is necessary to restrain highly energetic electrons produced in the driver from the expansion chamber. This is done by imposing an additional magnetic field, called *filter field*, that hinders fast electron transport. The mobility and diffusion coefficients are consequently modified as

$$D_\perp = \underbrace{\frac{k_B T}{m\nu_c}}_{D_\parallel} \frac{1}{1+\left(\frac{\omega_c}{\nu_c}\right)^2} \qquad \nu_\perp = \underbrace{\frac{q}{m\nu_c}}_{\nu_\parallel} \frac{1}{1+\left(\frac{\omega_c}{\nu_c}\right)^2} \tag{2.5}$$

where the parallel and perpendicular directions are referred to the magnetic field lines. If the cyclotron frequency ω_c is much larger than the collision frequency, the particle transport along the perpendicular direction is strongly reduced with respect to the parallel one. This indeed helps to reduce the electron temperature inside the expansion chamber and, more importantly, in the extraction region. Generally speaking, the magnetic field alters both electron and ion transport causing particle gyration: however, as the ion Larmor radius is much larger than the electron one, ions can be assumed to be unmagnetised.

While volume production is exploited in both positive and negative ion sources, the surface production mechanism is a defining feature of the latter. In this case, fast atoms or single-charge ions gain additional electrons by impacting on the source walls. In order to enhance the probability of electron gain, the surface work function is lowered by depositing a layer of caesium (Cs), which is usually vaporised by some dedicated ovens. By doing so, the local negative ion density increases and an

ion-ion plasma layer is formed. The main production channels are

$$\begin{aligned} H + e^-_{wall} &\rightarrow H^- \quad (1) \\ H^+ + e^-_{wall} &\rightarrow H \quad (2a) \\ H + e^-_{wall} &\rightarrow H^- \quad (2b) \end{aligned} \tag{2.6}$$

A single-step process is sufficient for neutral atoms, whereas two steps are required for protons. The fraction of dissociated molecular neutrals and ions will also contribute to these processes, together with the particles generated by collisions.

As the first ionization potential for caesium is 3.8 eV, previously vaporised neutral atoms are easily ionized and subsequently redistributed by the plasma. A thin caesium layer allows to lower the surface work function down to 2 eV, providing a significant increase in the H^- production rate. However, in addition to the ED (2.4), there are several other destruction processes that can take place, namely

$$\begin{aligned} H^- + H &\rightarrow e^- + H_2 \\ H^- + H^+ &\rightarrow H + H \\ H^- + H_2 &\rightarrow H_2 + H + e^- \\ H^- + H_2^+ &\rightarrow H_2 + H \\ H^- + H_3^+ &\rightarrow H_2 + H_2 \end{aligned} \tag{2.7}$$

and, for this reason, the negative ion mean free path cannot be very large. Therefore, only the ions produced in the very proximity of the beam apertures are likely to be extracted.

2.2.3 Beam extraction

In negative ion sources, surface production is the main generation mechanism for beam ions. However, as the ions are reflected back from the surface, their initial velocities are on average opposite to the beam extraction direction; moreover, the source plasma is electropositive and, as a consequence, there is tendency to trap negative ions. Nonetheless, ions manage to leave the source volume as both the magnetic field and the collisions contribute to deflect their trajectories towards the extraction region. In this case, space charge compensation is due to slow ions rather than fast electrons, as in positive ion sources. The beam extraction takes place between the source wall located on the side opposite to the driver, usually called plasma grid (PG), and the extraction grid (EG), which is positively biased with respect to the PG. The potential drop between these two grids should not be larger than 10 kV in order to prevent excessive thermal load on the source components.

All the grids feature several round apertures of a few mm diameter. When crossing the PG, the extracted ions enter a vacuum region where they are accelerated by the voltage drop between the PG and the EG. The transition layer between the source and the extraction grid is called *meniscus*: it usually has a convex profile and it acts as an electrostatic lens for the beamlets.

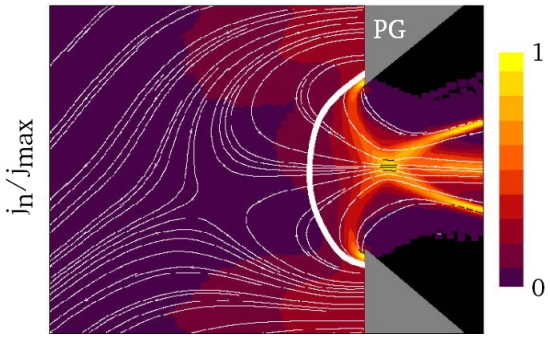

Figure 2.6: Normalised negative ion current density profile obtained with a 2D PIC-MCC simulation[11]. The plasma meniscus is highlighted by the white line.

The correlation between plasma parameters and meniscus shape is still not completely determined for negative ion sources[12]. The beamlets were found to be composed of a highly focused core and a peripheral external layer with larger divergence, called *halo*. The latter is probably caused by the shape of the plasma meniscus itself[13]: the ions extracted from the outer region of the meniscus are over-focused, thus yielding the beam halo formation. While core ions manage to cross the apertures, halo ions might be intercepted by the grids and some additional heat might be deposited on their surfaces.

The maximum current that can be extracted from each beamlet is limited and it is given by the Child-Langmuir law

$$I = \pi R^2 j = \frac{4\pi\varepsilon_0}{9}\sqrt{\frac{2Ze}{m}}\frac{R^2}{d^2}U^{3/2} = \mathbb{P}U^{3/2} \tag{2.8}$$

where U is the extraction voltage, d is the length of the plane diode representing the beamlet and $\mathbb{P}$ is defined as the beam *perveance*. The parameter $\mathbb{P}$ depends on the extracted species mass m and atomic number Z, on the aperture radius R^2 and also on d. The beam divergence shows a minimum as a function of $\mathbb{P}$.

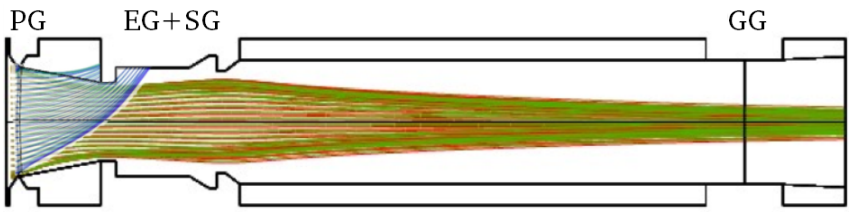

Figure 2.7: Simulation of particle trajectories in the LHD N-NBI[14].

Together with the negative ions, there is also a non-negligible fraction of co-extracted electrons. This contribution is usually damped with an additional magnetic field before the final accelerating stage, as represented from the blue trajectories in Figure 2.7. The PG is usually positively biased with respect to the source itself, in order to further reduce the amount of co-extracted electrons. In some sources, this effect is enhanced by another grid located next to the PG.

2.3 Plasma uniformity

Having briefly described the plasma extraction mechanism, it is easier to understand the meaning of "uniform" source plasma: the negative ion flux reaching the PG has to be equal for all the grid apertures. There are several reasons for non-uniformities to arise; for instance, the plasma density is determined by the so-called *source function*[15], that is the ionization rate as a function of the position in the source itself, so it will depend on the source geometry and also on the background gas density distribution.

In a first approximation, the plasma expansion towards the extraction region is a diffusive process, hence its flux is proportional to the density gradient. In particular, the plasma density in the expansion chamber is typically one order of magnitude lower than in the driver region mainly because of the magnetic filter field, which causes plasma particles to be confined inside the driver. A typical density profile in the SPIDER negative ion source is shown in Figure 2.8.

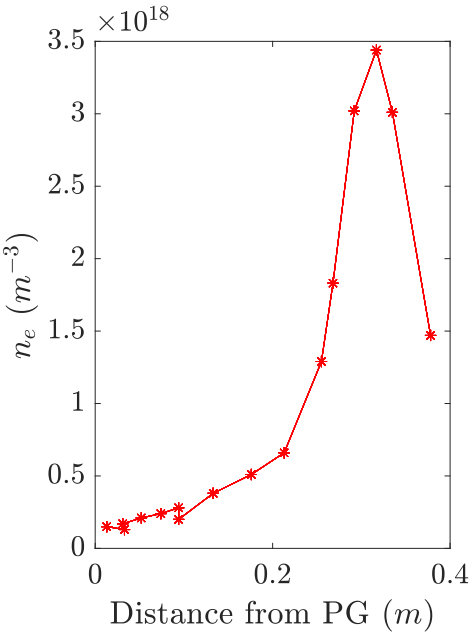

Figure 2.8: Typical density profile along the driver axis measured in the SPIDER source.

Two main causes for plasma asymmetry can be identified:

- Drift motions, namely both the $\vec{E} \times \vec{B}$ and the diamagnetic drift;
- Plasma potential oscillations, possibly enhanced by the RF coupling.

Both these contributions will be further described in the following sections.

2.3.1 Drift motions

The presence of the magnetic filter field inevitably introduces an $\vec{E} \times \vec{B}$ drift. The additional velocity is defined as

$$\vec{v}_{\vec{E}\times\vec{B}} = \frac{\vec{E} \times \vec{B}}{|B|^2} \tag{2.9}$$

and it is independent of the particle charge, therefore no separation is induced. As briefly mentioned in Section 2.2.2, the magnetic filter field hinders electron transport across the field lines: fast electrons are consequently reflected back in the driver region. This results in a strong density gradient, ultimately leading to the rise of a diamagnetic drift. In this case, the additional velocity is defined as

$$\vec{v}_{diam} = \frac{\vec{B} \times \nabla_\perp p}{nq\,|B|^2} \tag{2.10}$$

and depends on the particle charge. However, only the transport along the perpendicular direction to the magnetic field is altered: indeed, the particle equation of motion reads

$$mn\left[\frac{\partial \vec{v}}{\partial t} + (\vec{v}\cdot\nabla)\,\vec{v}\right] = qn\left(\vec{E} + \vec{v} \times \vec{B}\right) - \nabla p - mn\nu_c\vec{v} \tag{2.11}$$

which in the stationary state becomes

$$0 = qn\left(\vec{E} + \vec{v} \times \vec{B}\right) - k_B T\nabla p - mn\nu_c\vec{v} \tag{2.12}$$

The motion along the parallel direction to $\vec{B}$ will be described as

$$\begin{aligned} 0 &= qn\vec{E}_\parallel - k_B T\nabla_\parallel p - mn\nu_c\vec{v}_\parallel \\ \vec{v}_\parallel &= \mu_\parallel\vec{E}_\parallel - D_\parallel\frac{\nabla_\parallel n}{n} \end{aligned} \tag{2.13}$$

where $\mu_\parallel$ and $D_\parallel$ are defined as in Equation 2.5. Equation 2.13 implies that the transport along the parallel direction is not affected by the magnetic field. On the other hand, the motion along the perpendicular direction will be described as

$$\begin{aligned} 0 &= qn\vec{E}_\perp - qn\vec{v}_\perp \times \vec{B} - k_B T\nabla_\perp p - mn\nu_c\vec{v}_\perp \\ \vec{v}_\perp &= \frac{q}{m\nu_c}\vec{E}_\perp - \frac{k_B T}{m\nu_c}\frac{\nabla_\perp n}{n} + \frac{q}{m\nu_c}\vec{v}_\perp \times \vec{B} \end{aligned} \tag{2.14}$$

The cross product of $\vec{v}_\perp$ times the magnetic field yields

$$\vec{v}_\perp \times \vec{B} = \frac{q}{m\nu_c}\vec{E}_\perp \times \vec{B} - \frac{k_B T}{m\nu_c}\frac{\nabla_\perp n}{n} \times \vec{B} + -\frac{q}{m\nu_c}\left(|B|^2\,\vec{v}_\perp - \vec{B}\left(\vec{v}_\perp \times \vec{B}\right)\right) \tag{2.15}$$

and by substituting Equation 2.15 in 2.14 one obtains

$$\begin{aligned} \vec{v}_\perp &= \nu_\perp\vec{E}_\perp - D_\perp\frac{\nabla_\perp n}{n} + \frac{\omega_c^2}{\nu_c^2 + \omega_c^2}\left(\frac{\vec{E}_\perp \times \vec{B}}{|B|^2} - \frac{k_B T\nabla_\perp n \times \vec{B}}{qn\,|B|^2}\right) \\ &= \nu_\perp\vec{E}_\perp - D_\perp\frac{\nabla_\perp n}{n} + \frac{\omega_c^2}{\nu_c^2 + \omega_c^2}\left(\vec{v}_{\vec{E}\times\vec{B}} + \vec{v}_{diam}\right) \end{aligned} \tag{2.16}$$

Thus the presence of the magnetic filter field alters plasma transport along the perpendicular direction to $\vec{B}$. With reference to Figure 2.13, the diamagnetic contribution introduces a vertical drift with maximum intensity at the driver exit, whereas the $\vec{E} \times \vec{B}$ drift depends on the $\vec{E}$ field direction.

2.3.2 Potential oscillations

A time-varying meniscus shape might worsen the beamlet convergence, causing the extracted beam current to oscillate in time. Indeed, variations of the extracted beamlet profiles were found to be significantly correlated with the RF induced fluctuations in the source plasma[16]; in particular, the beam core was also found to be affected. This phenomenon might be enhanced and further complicated in a multiple-driver source as SPIDER, where superposition effects might arise since the induced oscillations are not necessarily synchronous between one driver and the other.

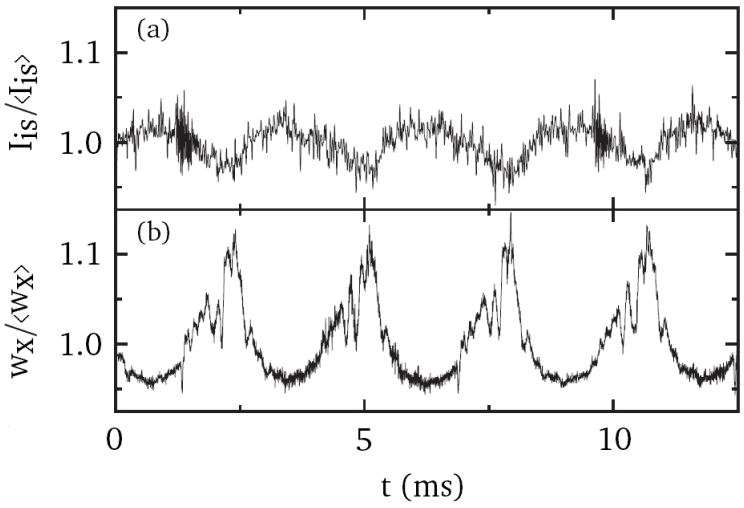

Figure 2.9: Normalised ion saturation current (a) and normalised beamlet width in the x-direction (b) as a function of time[16].

2.4 The SPIDER experiment

SPIDER[17] is a RF driven, caesium-assisted negative ion source. It is composed of 8 drivers, each one of them supplied with up to 100 kW power at 1 MHz frequency. All drivers are connected to a single expansion chamber of size 80 × 160 × 25 cm. The design parameters are listed in Table 2.1.

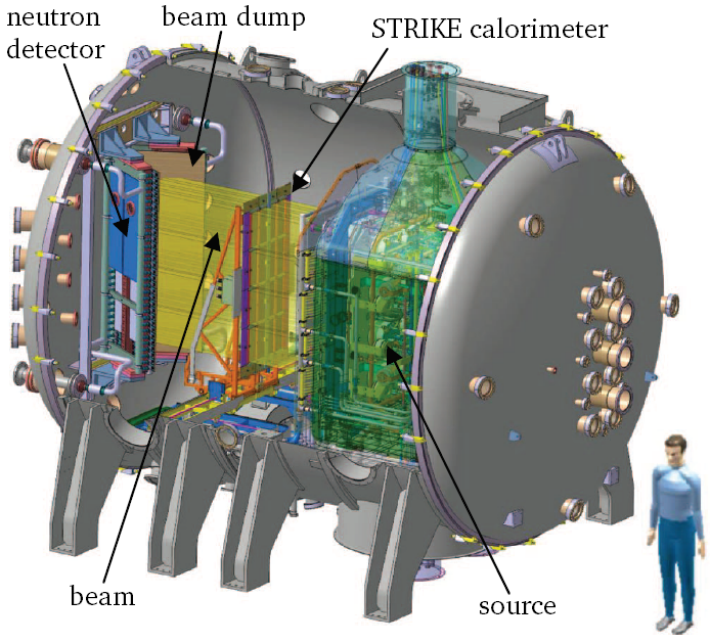

Figure 2.10: Schematic view of the SPIDER negative ion source[18].

Parameter	Value
Beam energy	100 keV
Max source filling pressure	0.3 Pa
Max deviation from beam uniformity	±10%
Extracted ion current density	$> 355\,A/m^2$ H_2; $> 285\,A/m^2$ D_2
Beam-on time	1 h
Co-extracted electron fraction	< 0.5 H_2; < 1 D_2

Table 2.1: Design parameters for the SPIDER source.

The accelerating column is composed of three grids, each one providing a total of 1280 apertures, arranged in 4 × 4 groups of 5 × 16 apertures:

- Plasma Grid (PG), which is exposed to the plasma;
- Extraction Grid (EG), biased at 12 kV with respect to the PG so as to allow ion extraction;
- Grounded Grid (GG), which is the final acceleration stage and it is biased at 100 kV with respect to the EG.

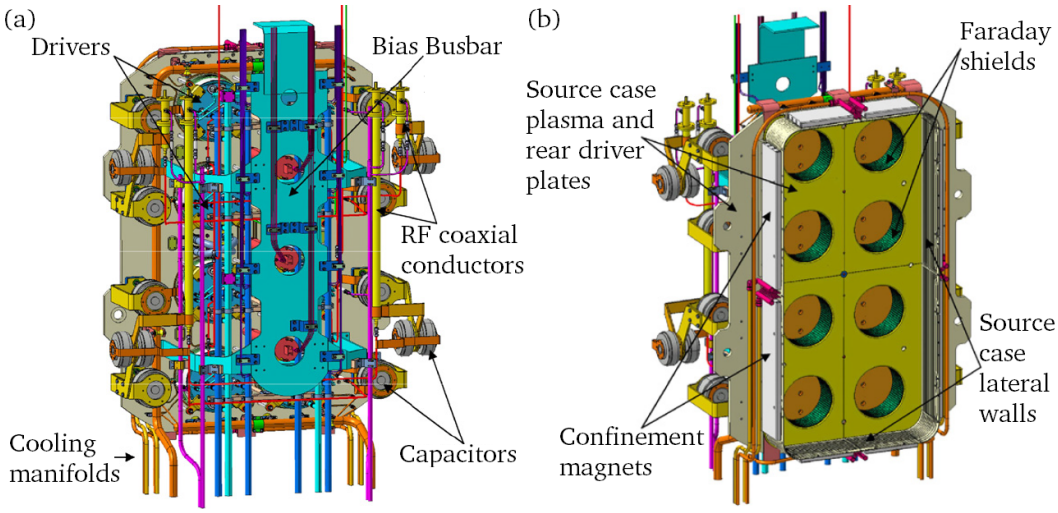

Figure 2.11: Schematic view of the drivers region, front and rear of the source.

Both the EG and GG feature a set of permanent magnets: in the first case, the generated field is used to dump the co-extracted electrons, whereas in the second case it helps to counteract the ion trajectory deflection introduced by the EG magnets. The PG surface is partially covered by the Bias Plate (BP), a grid with wider openings of the same size of the beamlet modules. The magnetic filter field is generated by currents flowing in the PG and in some additional busbars, as shown in Figure 2.12.

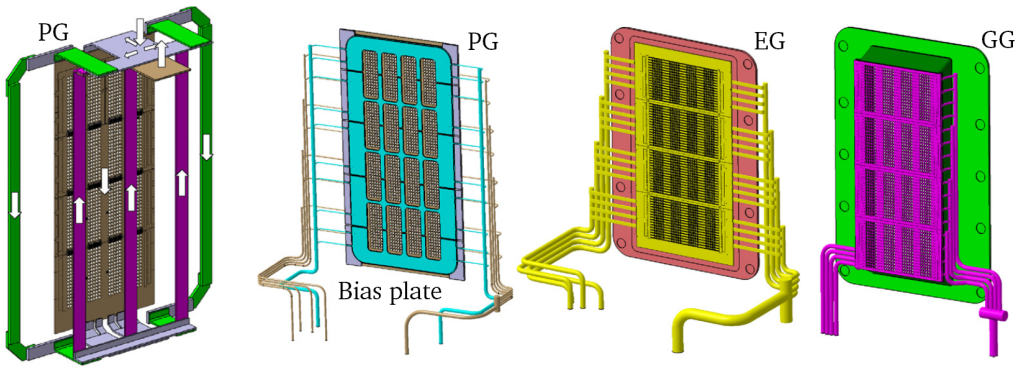

Figure 2.12: Schematic view of the SPIDER accelerating grids, Bias Plate, and the busbars used to generate the magnetic filter field[19,20].

Chapter conclusion

Some insights on the advantages and drawbacks of RF negative ion sources with respect to arc sources and positive ion sources have been provided in this chapter, together with a description of the most relevant features of RF ion sources operation. To conclude, figure 2.13 shows a schematic overview of all the aforementioned physical processes.

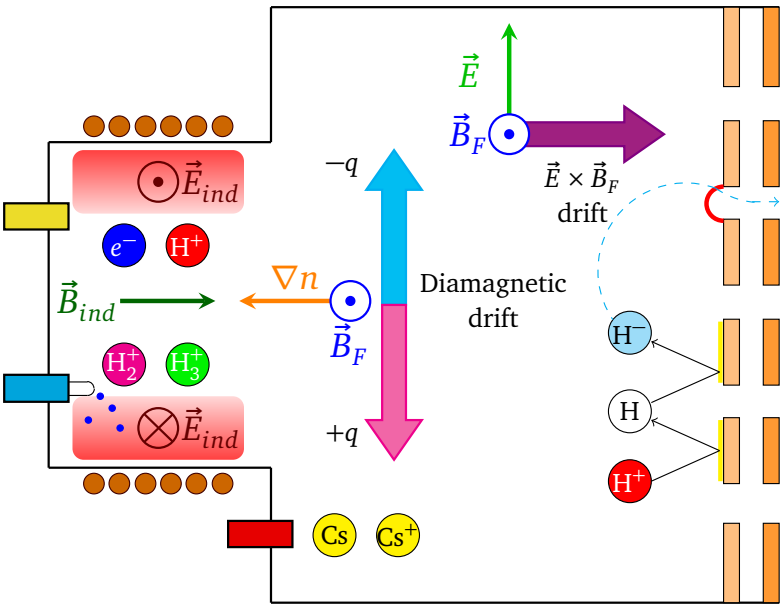

Figure 2.13: Overview of the most important physical processes in a RF negative ion source. The red areas inside the driver are the electron heating regions. Recall that the induced fields periodically reverse their direction.

Chapter 3

GPPIC

This chapter provides a brief introduction on the Particle-In-Cell method for plasma simulation. The PIC-MCC numerical code used in this thesis work is described, with a particular focus on the involved collision processes, on the simulation convergence towards a stationary state and on the scaling laws used for the adaptation of a many-particle three-dimensional system to a reduced two-dimensional domain. Finally, the overall algorithm scheme is shown for the sake of completeness.

3.1 Particle-In-Cell fundamentals

The **P**article-**I**n-**C**ell (PIC) method[21] is a widespread Lagrangian scheme for plasma simulation. The system is described as a finite collection of charged particles which can move inside a defined simulation domain. The particle dynamics are determined by both the self-induced and external electromagnetic fields and the macroscopical properties of the system are derived from the particle positions and velocities. The time evolution of the chosen system can be achieved by repeating a sequence of operations in an iterative fashion: at each step, the particle positions are updated according to their velocities which, in turn, are given by the force acting on them. For a simple electrostatic system, the force can be derived by solving the Poisson equation, that depends on the particle charge density

$$\nabla^2 \phi = -\frac{\rho}{\epsilon_0} \tag{3.1}$$

and the electric field can be subsequently derived as

$$\vec{E} = -\vec{\nabla}\phi \tag{3.2}$$

Finally, if one assumes that the particle motion is driven by the electrostatic force only, the new particle positions and velocities can be obtained by solving Newton's equations of motion

$$\frac{d\vec{v}}{dt} = \frac{q}{m}\vec{E} \qquad \frac{d\vec{x}}{dt} = \vec{v} \tag{3.3}$$

At this point, the system density can be calculated and the whole cycle can be repeated iteratively until a stationary state is reached.

3.1.1 Physical properties extrapolation

The macroscopical properties of the system are calculated on a discretized domain, called *mesh*. For PIC simulations, the mesh is usually structured and constant over time. At each timestep, the simulation domain is divided in *cells* that will contain a certain number of particles. The physical properties are obtained for each cell by means of linear interpolation.

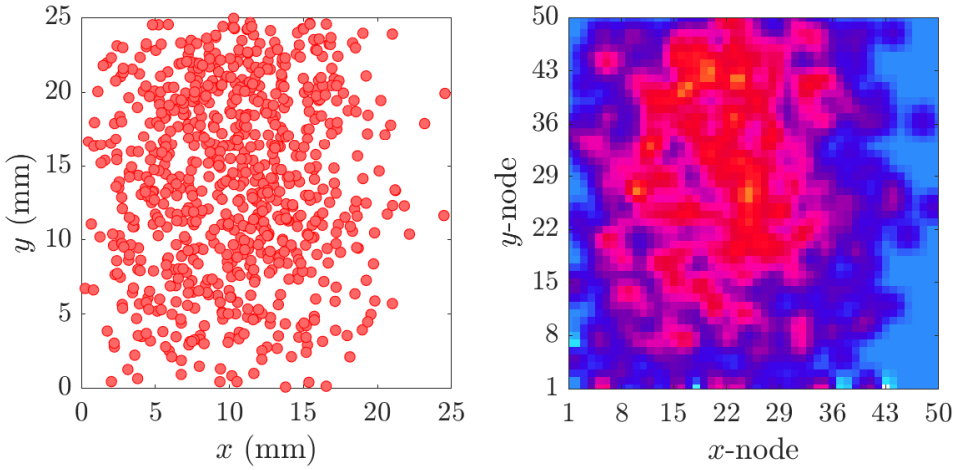

Figure 3.1: Example of density interpolation from particle positions in a simple squared domain.

The domain in Figure 3.1 is a square with sides of 25 mm, whereas the numerical density is calculated on a simple mesh composed of 50 × 50 squared cells of size 0.5 mm.

3.1.2 Density scaling, time interval and characteristic length

The densities of a real physical system are usually extremely high and, for this reason, it would be unfeasible to follow the time evolution of each single particle. It is therefore necessary to reduce either the simulation domain or the degrees of freedom of the system by "grouping" the real particles. In the second case, the system dynamics are described in terms of *macroparticles* (MP), each one of them representing a given number of "physical" particles. This number is usually called *macroparticle weight* (MPW) and it can be defined as the ratio between the total number of real particles and the number of simulated macroparticles

$$\mathrm{MPW} = \frac{n_0}{V_d} N_{\mathrm{MP}}$$

where n_0 and V_d are the real system density and volume, whereas N_{MP} is the MP number.

The ratio between the MP density and the real particle density defines the density scaling factor, β: the simulated densities can be of several orders of magnitude smaller than the real ones and this effect must be taken into account when analysing the simulation results.

Both the time interval of the simulation step and the characteristic dimension of the mesh cells should be chosen with the aim of achieving the best compromise between high precision and reasonable computational time; speaking of plasma simulation, these quantities are limited by the plasma frequency, ω_{pe}, and the Debye length, λ_{De}, as follows

$$dt < \frac{1}{\omega_{pe}} \qquad dx < \lambda_{De} \tag{3.4}$$

These constraints must be fulfilled in order to correctly reproduce the plasma properties: indeed, if $dt > (\omega_{pe})^{-1}$ the simulation would not be capable of describing a complete plasma oscillation, whereas if $dx > \lambda_{De}$ the effect of electrostatic fields on plasma particles would be screened.

3.2 gppic

The simulation tool used in this thesis work is a 2D-3V electrostatic PIC-MCC code called gppic[22], written in C++/CUDA. The aim of gppic is to reproduce the plasma generation and expansion mechanisms in the SPIDER source, so as to analyse the drift motions arising both in the drivers and in the expansion chamber and, possibly, to investigate the plasma properties dependence on different parameters such as the background gas pressure or the magnetic field intensity. The program was not designed from the ground up as several key implementation issues have already been addressed, developed and validated for different applications: the original code has therefore been repurposed and some new features have been included.

The simulation domain is a two-dimensional plane lying on a vertical section of the source volume. The x axis represents the beam axis, whereas the y axis is referred to the source vertical dimension, as shown in Figure 3.2. The bias plate areas (orange) are of size 10 mm×25 mm, whereas the magenta surface represents the plasma grid (PG), with no apertures. The light blue regions below and over the driver are not accessible by the plasma.

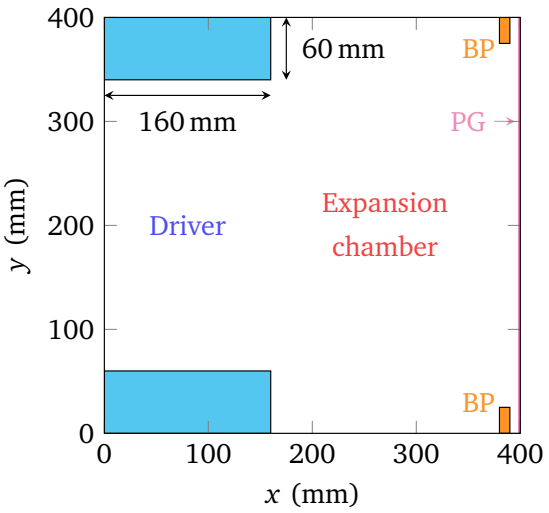

Figure 3.2: Representation of the simulation domain.

Only one driver is considered in the simulation: this choice stems from the need to avoid possible complications that might arise while simulating two or more drivers because of superposition effects. Furthermore, a single-driver simulation is sufficient for providing data that can be compared with the experimental measurements taken in SPIDER, as the latter have been performed while operating one generator at a time.

The extraction grid and the apertures on the PG surface are not reproduced since the analysis of the plasma extraction mechanism is not covered in this thesis work. No periodicity conditions were included on any domain wall.

3.2.1 Basic algorithm steps

At first, some basic properties such as the timestep value, the dimensions and shape of both the domain and the mesh, the most used physical constants and some macroscopic properties are given as input, together with some variable parameters such as magnetic field intensity, background gas pressure or wall potentials. The most relevant simulation parameters are listed at the end of this chapter (Table 3.8), together with a flow diagram (Figure 3.8) that summarises the code algorithm.

The simulated density is of the order of $10^{14}\,\mathrm{m}^{-3}$ and the chosen density scaling factor is $\beta = 10000$, in such a way that βn_{sim} will be comparable to the real plasma density, that in the SPIDER source is expected to fall into the $10^{18}\,\mathrm{m}^{-3}$ to $10^{19}\,\mathrm{m}^{-3}$ range. As already mentioned in section 3.1.2, the simulation timestep and the cell characteristic dimensions have to be chosen while satisfying some physical constraints: as the simulated plasma density is of the order of $10^{14}\,\mathrm{m}^{-3}$, the Debye length will be $\lambda_{De} \geq 0.001\,\mathrm{m}$ if the electron temperature T_e is greater than or equal to 2 eV. It is important to satisfy the $dx \leq \lambda_{De}$ criterion for the lowest expected value of T_e, as the electron temperature inside a negative ion source can drop from tens of to a few eV because of the magnetic filter field. The expected plasma frequency is of the order of 600 MHz and the simulation timestep has to be $\leq 2\,\mathrm{ns}$.

Initialisation

Although the overall dimensions of the simulation domain are already given as input parameters, the actual structure has to be properly defined before the main iteration cycle begins. To do so, the source surfaces seen by the plasma are defined and their potential is set to a fixed value in such a way to provide some boundary conditions for the solution of the Poisson equation.

The background gas can be either molecular hydrogen or deuterium with a fraction of dissociated atoms. The initial plasma composition is arbitrarily chosen while satisfying the quasi-neutrality constraint and the considered species for both H and D are:

$$e^- \quad H^+ \quad H_2{}^+ \quad H_2{}^+ \quad H^- \quad H \tag{3.5}$$

that are electrons, atomic and molecular ions and fast atoms. The latter are produced because of collision processes and, together with H^+ ions, they are the precursor particles for the formation of negative ions. As only the volume production mechanism is considered in this thesis work, there is no need to include caesium ions Cs^+ among the simulated species.

Main iteration cycle

The main iteration cycle can be thought of as a list of operations that can be performed either at each single step or only at a defined iteration, depending on their specific purpose. Once the list is completely checked, the simulation time is updated and the main cycle is repeated iteratively until the step limit is reached.

It is possible to run a simulation either from the start or from a previously saved configuration. In the second case, a list containing all the positions and velocities of the macroparticles is read as input file and its contents are stored in the GPU memory. This option is extremely useful to test the simulation response to different conditions without reproducing the entire expansion process, as this part only can take up to five days.

The first operation in the time cycle is the density calculation, as this quantity is needed for solving the Poisson equation. In the meantime, both the particle velocity and temperature are also obtained. As briefly mentioned in Section 3.1, the plasma properties are calculated on a finite mesh composed of squared cells: to do so, each particle is assigned to a cell and its properties are deposited on the four cell nodes through a first order bi-linear interpolation. As a second step, the Poisson equation is solved on the mesh nodes by applying the finite differences method. Particular care is taken when the considered nodes belong to the domain boundaries or when they are required to satisfy either the Dirichlet or the Neumann condition, that is when they have a fixed potential value or when the potential difference with respect to some other node has to be constant. The Poisson equation is solved iteratively until the obtained solution respects the convergence criterion: more precisely, the difference between the input density and the one obtained with the potential solution has to be smaller than a defined tolerance value, which is usually set to 1×10^{-7}.

Once the potential is known the electric field components can be obtained on the mesh points; however, since the macroparticles will be subject to the local electromagnetic field, it is necessary to use again the bi-linear interpolation method to obtain the local $\vec{E}$ components. While the electric field is derived self-consistently from the electrostatic potential, the local magnetic field is calculated analytically: indeed, as both its direction and intensity are constant over time, it is not necessary to include a self-consistent solution of the Ampère-Maxwell and Faraday laws. Given the electromagnetic field, the new particle velocities are obtained with the Boris[23] algorithm.

The updated particle positions are checked with respect to the domain boundaries and a *flag* is assigned to each one of them on the basis of their new status: particles can either stay within the domain or exit from one of the walls. Furthermore, as the macroparticle motion is three-dimensional, it is necessary to include some constraints also for the unsimulated direction in order to avoid possible problems such as charge accumulation. The implemented algorithm has been proposed in previous works[24] and provides a different criterion for negative and positive charges: in the first case, plasma particles are lost if their kinetic energy along the z direction is sufficient to overcome the potential barrier that rises between the plasma bulk and a fictitious wall along the z dimension

$$\frac{1}{2e} m v_z(x,y)^2 \geq \phi_{bulk}(x,y) - \frac{\mathrm{T}_e(x,y)}{2} \tag{3.6}$$

where both ϕ_{bulk} and T_e are expressed in eV. Otherwise, if Equation 3.6 is not satisfied, negative particles are mirrored. On the other hand, all positive charges

and neutrals reaching the walls along the z direction are lost independently of their energy.

After the particle positions and velocities have been updated and checked, the collision cycle can start. This is one of the most fundamental aspects of the entire simulation code, as the quality of the results is strongly affected by the chosen processes and also by the accuracy of their cross sections. As further explained in Section 3.4, the system evolution is completely determined by the collision rates since there are no constraints on the macroparticle number. The correct implementation of all the included interactions is therefore of primary importance for obtaining a reasonable stationary state.

Final steps

If the simulation does not start from a previous configuration, the domain is populated with new macroparticles: this implies that the first iteration is actually performed with empty domain so as to provide a reference vacuum solution for the Poisson equation. Finally, the output data is copied from the GPU and stored in plain text files.

data type	saving step
MP number and average temperature	each step
collision statistics	each step
density, temperature and potential maps	each 1 or 100 steps
electric field components maps	each 1 or 100 steps
velocity components maps	each 1 or 100 steps
particle trajectories	each step
potential, density and temperature probes	each step

Table 3.1: Output data obtained from the simulation.

3.2.2 CUDA programming

CUDA®[25] is a programming interface developed by NVIDIA for parallel computing on general purpose graphical processing units (GPGPU), which are optimized for multiple-thread performances. GPU computing allows to significantly reduce the simulation time, even though the memory management is slightly more complex with respect to single-thread programming.

The main code is written in C++ and runs on the central processing unit (*host*). It determines the sequence of operations and initialises the instructions on the GPU (*device*), where all the computations are performed: as a consequence, most of the used variables need to be defined both on the CPU and on the GPU and, for the latter, the proper amount of memory has to be allocated.

```
//host initialisation
   float a[3]={0.0};

    //device initialisation and memory allocation
    float *d_a;
    cudaMalloc(&d_a,3*sizeof(float));
```

Listing 3.1: Comparison between CPU and GPU variable initialisation.

The GPU functions are called *kernels*: their definition is qualitatively similar to the standard host functions, even though they need to be qualified as `global`, `device` or `host` functions: the *global* ones are called from the host and executed on the device, whereas the *device* and *host* ones are called and executed on the device and host respectively.

```
    //host function definition
    float sum_vec(float a,float b,int size,float c){
        for (i=0;i<size;i++){
            c[i]=a[i]+b[i];
        }
        return c;
    }

    //device function definition
    __global__ void sum_vec(float*a,float*b,int size,float*c){
        int idx=blockDim.x*blockIdx.x+threadIdx.x;
        if(idx<size){
            c[idx]=a[idx]+b[idx];
        }
    }
```

Listing 3.2: Comparison between CPU and GPU function definition.

Kernels need to return void type and, more importantly, they cannot access host memory: for this reason, CUDA provides some built-in functions that allow to copy data either from the host to the device or viceversa. Both the amount of memory and the transfer "direction" need to be specified at each call.

```
    float c[3]={0.0}; float*d_c;
    cudaMalloc(&d_c,3*sizeof(float));

    //copy value from host to device
    cudaMemcpy(d_c,&c,3*sizeof(float),cudaMemcpyHostToDevice);

    //launch kernel
    sum_vec<<<nBlocks,prop.maxThreadsPerBlock>>>(d_a,d_b,3,d_c);

    //copy value from device to host
    cudaMemcpy(&c,d_c,3*sizeof(float),cudaMemcpyDeviceToHost);
```

Listing 3.3: Example use of the kernel defined in 3.2.

Another main difference between standard functions and kernels stems from the fact that the GPU computation is performed in parallel and, for this reason, the

number of used threads needs to be specified whenever a kernel is launched. With reference to the example 3.3, `nBlocks` is the number of memory blocks dedicated to the computation, `prop.maxThreadsPerBlock` is the maximum number of threads for each block.

Finally, another main feature of GPU parallel computing is that threads operate independently from one another and, moreover, they can operate asynchronously. Nevertheless, if the function `cudaDeviceSynchronize()` is called from the host side, the main cycle operations are suspended until all the previously launched kernels have completed their computation, as to make sure that they all have been completely executed.

3.3 Collisions

Many collision processes have to be considered in order to reproduce the plasma evolution as faithfully as possible. The included interactions can be grouped as follows:

- collisions between plasma particles and background gas;
- collisions between charged particles.

Each process is required to satisfy the energy conservation law. The cross sections are loaded in a dedicated library, called Sammy, which allows to store the cumulative reactivity for each projectile-target pair, the energy thresholds and also the fit coefficients for the cross sections.

Many heavy-particles collisions with molecules were already included in the original `gppic` code, whereas the electron impact processes on molecules and the interaction between plasma particles and atoms have been added during this thesis work.

3.3.1 Plasma-gas interaction

The interaction between plasma particles and the background gas is implemented with the *P-null collision* method[26]. Both molecules and atoms resulting from dissociation are considered as possible targets.

			Process	Reference
$e^- + H$	$\rightarrow$	$e^- + H^+ + e^-$	ionization	[27]
$e^- + H$	$\rightarrow$	$e^- + H[n=2]$	atomic excitation	[27]
$e^- + H$	$\rightarrow$	$e^- + H[n=3]$	atomic excitation	[27]
$e^- + H$	$\rightarrow$	$e^- + H[n=4]$	atomic excitation	[27]
$e^- + H$	$\rightarrow$	$e^- + H[n=5]$	atomic excitation	[27]
$e^- + H_2$	$\rightarrow$	$e^- + H_2$	elastic scattering	[26]
$e^- + H_2$	$\rightarrow$	$e^- + H_2^+ + e^-$	ionization	[28]
$e^- + H_2$	$\rightarrow$	$e^- + H + H$	dissociation	[27]
$e^- + H_2$	$\rightarrow$	$e^- + H^+ + H + e^-$	dissociative ionization	[27]
$e^- + H_2[v>3]$	$\rightarrow$	$H^- + H$	dissociative attachment	[27]
$e^- + H_2[v=1,2]$	$\rightarrow$	$e^- + H_2[v=1,2]$	vibrational excitation	[27]
$e^- + H_2[J=0]$	$\rightarrow$	$e^- + H_2[J=2]$	rotational excitation	[27]

Table 3.2: List of included e^- impact processes and cross section references.

The vibrational energy spectrum of gas molecules is fixed; if a given process involves only some vibrational states, the related cross section will be attenuated so as to consider the proper fraction of molecules. Gas atoms are instead considered to be always at their ground state since their de-excitation time is comparable with the simulation timestep[10].

			Process	Reference
$H^+ + H$	$\rightarrow$	$H + H^+$	charge exchange	[27]
$H^+ + H_2$	$\rightarrow$	$H^+ + H_2^+ + e^-$	ionization	[27]
$H^+ + H_2$	$\rightarrow$	$H + H_2^+$	charge exchange	[27]
$H^+ + H_2$	$\rightarrow$	$H^+ + H + H$	dissociation	[27]
$H^+ + H_2$	$\rightarrow$	$H^+ + H + H^+ + e^-$	dissociative ionization	[27]
$H^+ + H_2$	$\rightarrow$	$H^+ + H_2$	elastic scattering	[27]
$H_2^+ + H$	$\rightarrow$	$H^+ + H + H$	dissociation	[27]
$H_2^+ + H$	$\rightarrow$	$H_2 + H^+$	charge exchange	[27]
$H_2^+ + H_2$	$\rightarrow$	$H_2 + H^+ + H$	dissociation	[27]
$H_2^+ + H_2$	$\rightarrow$	$H_3^+ + H$	particle exchange	[27]
$H_2^+ + H_2$	$\rightarrow$	$H_2 + H_2^+$	charge exchange	[27]
$H_2^+ + H_2$	$\rightarrow$	$H_2^+ + H_2$	elastic scattering	[27]
$H_3^+ + H_2$	$\rightarrow$	H_2^+ (fast)	dissociation	[27]
$H_3^+ + H_2$	$\rightarrow$	H^+ (fast)	dissociation	[27]
$H_3^+ + H_2$	$\rightarrow$	H_2 (fast)	dissociation	[27]
$H_3^+ + H_2$	$\rightarrow$	H (fast)	dissociation	[27]
$H_3^+ + H_2$	$\rightarrow$	$H_3^+ + H_2$	momentum transfer	[27]
$H^- + H$	$\rightarrow$	$H + H^-$	charge exchange	[27]
$H^- + H$	$\rightarrow$	$H + H + e^-$	electron detachment	[27]
$H^- + H$	$\rightarrow$	$e^- + H_2$	associative detachment	[27]
$H^- + H_2$	$\rightarrow$	$H + H_2 + e^-$	electron detachment	[27]
$H^- + H_2$	$\rightarrow$	$H^+ + H_2 + 2e^-$	double electron detachment	[27]
$H^- + H_2$	$\rightarrow$	$H^- + H_2^+ + e^-$	ionization	[27]
$H^- + H_2$	$\rightarrow$	$H^- + H^+ + H^+ + 2e^-$	dissociative ionization	[27]
$H^- + H_2$	$\rightarrow$	$H^- + H^+ + e^- + H$	dissociative ionization	[27]
$H^- + H_2$	$\rightarrow$	$H^- + H_2$	momentum transfer	[27]

Table 3.3: List of included heavy ion impact processes and cross section references.

			Process	Reference
$H + H_2$	$\rightarrow$	$H + H_2^+ + e^-$	ionization	[27]
$H + H_2$	$\rightarrow$	$H^+ + H_2 + e^-$	electron detachment	[27]
$H + H_2$	$\rightarrow$	$H^- + H_2^+$	charge exchange	[27]
$H + H_2$	$\rightarrow$	$H + H^+ + e^- + H$	dissociative ionization	[27]
$H + H_2$	$\rightarrow$	$H + H^+ + H^+ + 2e^-$	dissociative ionization	[27]
$H + H_2$	$\rightarrow$	$H + H_2$	momentum transfer	[27]

Table 3.4: List of included neutral-neutral processes and cross section references.

3.3.2 Pseudo-binary collisions

Interactions between charged particles are implemented as "binary" processes: the projectiles are assumed to collide with a fixed target density and the electrostatic interaction between them is neglected. As each particle is likely to undergo a collision, they all need to be tested. The kernels used to implement these processes share the same structure, shown in Figure 3.3.

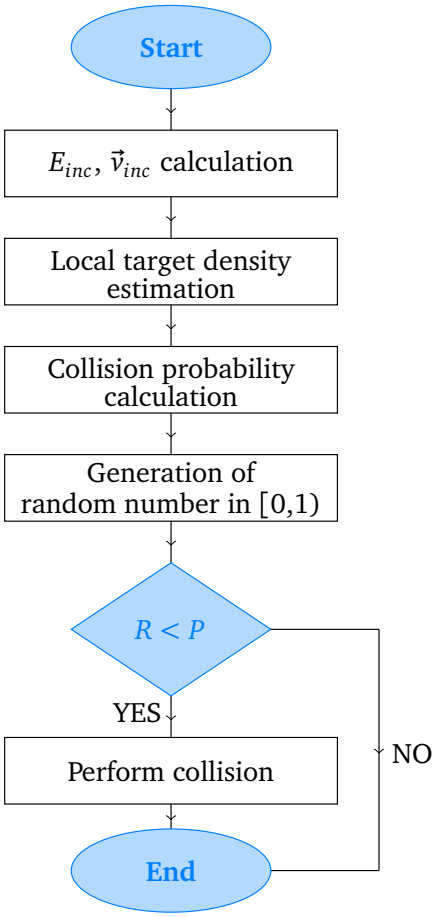

Figure 3.3: Basic common steps for pseudo-binary collisions implementation.

The collision probability is obtained as

$$P = \beta n \, \sigma(E_{inc}) \, v_{inc} dt \tag{3.7}$$

where $\beta n(x, y)$ is the rescaled local density, $\sigma(E_{inc})$ is the collision cross section, E_{inc} and v_{inc} are the kinetic energy and incident velocity of the projectile and dt is the simulation timestep. When the collision takes place, several operations can be performed depending on the considered process: for instance, the projectile can be lost and new particles might be generated.

Coulomb scattering

Coulomb collisions between electrons and ions have been implemented with the cumulative small-angle theory[29]. Due to the numerical complexity required to set up binary collisions by finding, ordering and pairing particles within each cell, a simplified approach considering fixed target particles is used. This approximation does not introduce significant errors in the e^--ion case as the velocity corrections for the ions are proportional to the electron-ion mass ratio.

The latter assumption does not hold for collisions between particles of similar mass; in this case, the same kernel is used two times, firstly to describe the electrostatic interaction felt by the A particles because of the B ones, secondly for the "reciprocal" process, i.e. B interacting with A. This can be done as the projectiles interact with a fixed target density. This simplification, consisting in a reciprocal reiteration of collisions against fixed target, is based on the assumption of a maxwellian distribution for the velocities of target particles; from the statistical point of view, this simplified approach will provide a good approximation if the MP number per cell is sufficiently high.

			Process	Reference
$e^- + H^+$	$\rightarrow$	$e^- + H^+$	Coulomb scattering	[29]
$e^- + H_2^+$	$\rightarrow$	$e^- + H_2^+$	Coulomb scattering	[29]
$e^- + H_3^+$	$\rightarrow$	$e^- + H_3^+$	Coulomb scattering	[29]
$e^- + H^-$	$\rightarrow$	$e^- + H + e^-$	electron detachment	[27]
$e^- + H_2^+$	$\rightarrow$	$e^- + H^+ + H^+ + e^-$	dissociative ionization	[27]
$e^- + H_2^+$	$\rightarrow$	$e^- + H^+ + H$	dissociative excitation	[27]
$e^- + H_2^+$	$\rightarrow$	$H + H$	dissociative recombination	[27]
$e^- + H_3^+$	$\rightarrow$	$e^- + H^+ + H + H$	dissociative ionization	[27]
$e^- + H_3^+$	$\rightarrow$	$H + H + H$	dissociative recombination	[27]
$H^+ + H^-$	$\rightarrow$	$H + H$	recombination	[27]
$H^+ + H^-$	$\rightarrow$	$H_2 + e^-$	associative detachment	[27]
$H^+ + H_2^+$	$\rightarrow$	$H^+ + H + H^+$	dissociation	[27]

Table 3.5: List of included processes between charged particles and cross section references.

3.4 Self-sustaining discharge

Unlike other simulation codes, `gppic` is able to reproduce plasma generation and expansion without any constraint on the macroparticle number: indeed, the final plasma composition is completely determined by the collision processes and their rates, as they are the main channels for the generation and destruction of plasma particles. However, in order to reproduce the experimental results, some feedback controls on the driver electron density and temperature have been implemented.

3.4.1 Thermostat

The electron temperature inside the driver region is kept at a sufficiently high value through a thermostat, which acts at each iteration and re-samples the velocity components of the electrons from a Maxwellian distribution at a defined temperature, T_{heat}, while preserving the motion direction.

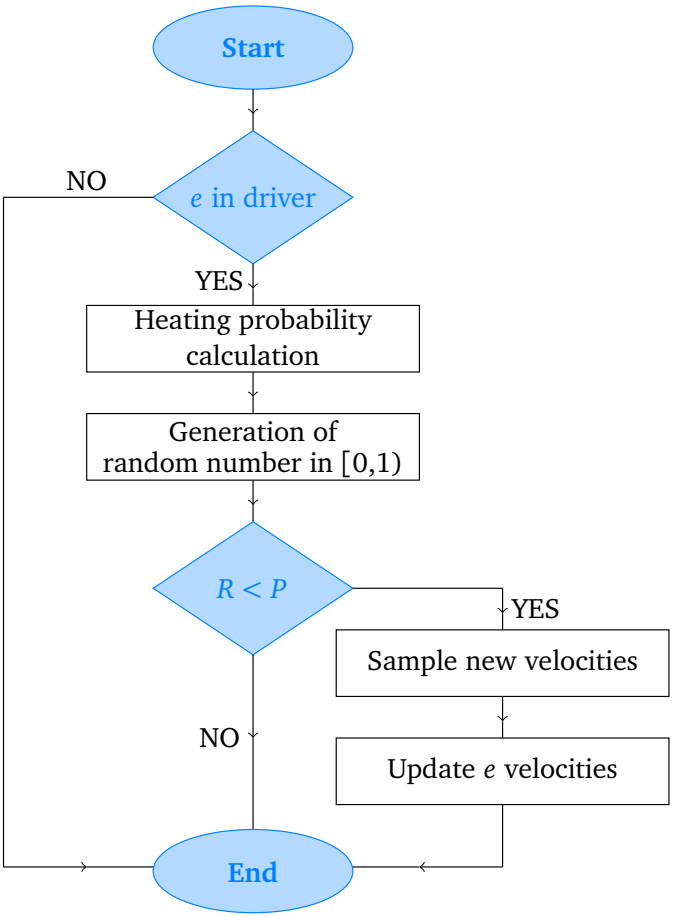

Figure 3.4: Thermostat scheme. All these steps are repeated for each electron inside the simulation domain.

The heating probability is obtained as

$$P = \nu_{heat} \cdot f(x,y) \cdot dt \tag{3.8}$$

where dt is the simulation timestep, ν_{heat} is an artificial frequency which determines how fast electrons are heated or cooled down and $f(x,y)$ is a normalised probability density function which is chosen in such a way that the heating probability at the driver center is maximized. It might be argued that the actual T_e maximum value is localized towards the outer region of the driver because of the skin effect; however, as further explained in Section 4.2, a detailed description of such phenomenon cannot be achieved in this simulation.

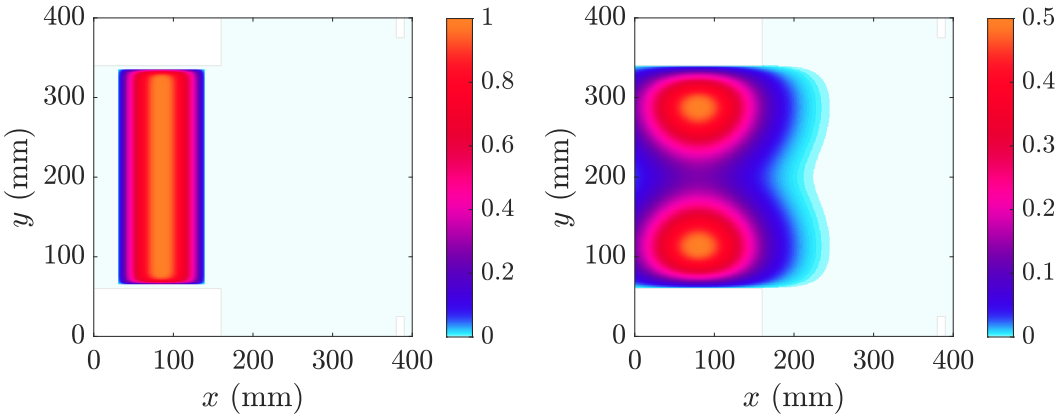

Figure 3.5: Example of a single peak and a double peak probability distribution function for the thermostat.

3.4.2 PI controller

The **P**roportional-**I**ntegral (PI) controller is a new `gppic` feature that allows to vary the background gas density n_{bg} and the driver electron heating frequency ν_{heat} (see Section 3.4.1) so as to tune the electron density n_e and temperature T_e inside the driver region. The n_e and T_e values are spatially-averaged over a small region in the driver center and subsequently time-averaged over the last 200 time cycles. The deviation with respect to the target values is defined as

$$\varepsilon_n = \frac{n_e^{avg} - n_e^{\text{target}}}{n_e^{\text{target}}} \qquad \varepsilon_{\text{T}} = \frac{\text{T}_e^{avg} - \text{T}_e^{\text{target}}}{\text{T}_e^{\text{target}}} \tag{3.9}$$

The new n_{bg}, ν_{heat} values are calculated at each timestep as

$$\begin{aligned} n_{bg}^{\text{new}} &= n_{bg}^{0}\,(1.0 - (K_P^{bg}\,\varepsilon_n + K_I^{bg}\,\text{I}[\varepsilon_n])) \\ \nu_{heat}^{\text{new}} &= \nu_{heat}^{last}\,(1.0 - (K_P^{heat}\,\varepsilon_{\text{T}} + K_I^{heat}\,\text{I}[\varepsilon_{\text{T}}])) \end{aligned} \tag{3.10}$$

where n_{bg}^0 is the initial background gas density, $\text{I}[\varepsilon_n]$ and $\text{I}[\varepsilon_{\text{T}}]$ are the error integrals. The coefficients K_P^{bg}, K_I^{bg}, K_P^{heat} and K_I^{heat} are the PI controller parameters. Notice that the background gas density correction is always referred to the initial

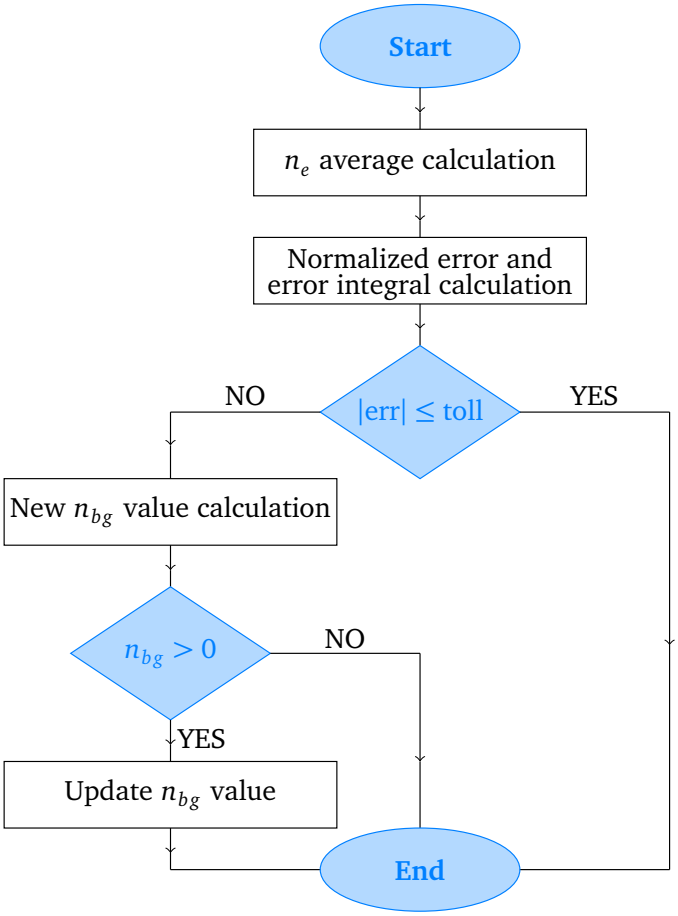

Figure 3.6: PI controller scheme. The same steps apply also for T_e control; in this case, the control parameter is ν_{heat} and the $n_{bg} > 0$ condition is replaced by $\nu_{heat}^{MIN} \leq \nu_{heat} \leq \nu_{heat}^{MAX}$.

value, n_{bg}^0, whereas the heating frequency correction is calculated on the basis of the previously derived value. This solution was found to be the most accurate one.

constant	value
K_P^{bg}	15
K_I^{bg}	0.0025
K_P^{heat}	0.0075
K_I^{heat}	2.5×10^{-6}

Table 3.6: PI controller parameters. Their values are chosen in such a way that the n_e, T_e convergence is optimized.

The values in Table 3.6 have been obtained by reproducing the simulation trends with a MATLAB® code. The electron density and temperature behaviours

were simplified as follows:

$$\begin{aligned} \mathrm{T}_e^{ML}(i) &= 5\,\mathrm{eV} + 20\,\mathrm{eV} \times \left(\frac{\nu_{heat}(i)}{1 \times 10^6\,\mathrm{Hz}} \right) \\ n_e^{ML}(i) &= n_e^{ML}(i-1) + 1.2 \times 10^{15}\,\mathrm{m}^{-3} \times \left(\frac{p_{bg}(i-1) - 0.09\,\mathrm{Pa}}{0.16\,\mathrm{Pa}} \right) \end{aligned} \tag{3.11}$$

where $\nu_{heat}(i)$ and $p_{bg}(i-1)$ are obtained from Equations 3.10. The K_I coefficients are chosen to be three orders of magnitude smaller than the K_P ones as the error integral contribution is a secondary correction. Moreover, $K_P^{bg} \gg K_P^{heat}$ so as to differentiate the response times and limit superposition effects: indeed, T_e affects the collision probabilities and, consequently, the discharge equilibrium.

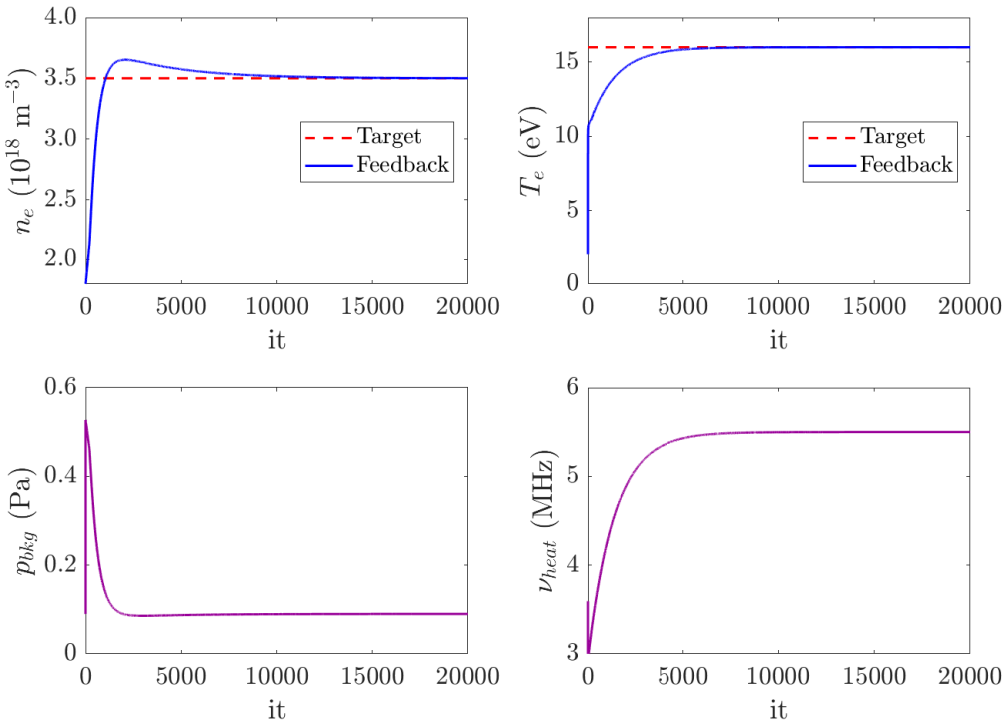

Figure 3.7: PI convergence obtained with the MATLAB code.

The PI coefficients used in `gppic` are very similar to the ones derived in this example; however, as can be seen from the results shown in Section 4.5.1, the real simulation behaviour is much more complex and the PI convergence is not as smooth as the one obtained with the simplified MATLAB code.

3.5 Scaling laws

As briefly mentioned in Section 3.2.1, the simulated plasma density is actually of several orders of magnitude lower than the real plasma density: for this reason, some plasma properties such as the Debye length and the sheath thickness are different, thus the simulation results need to be correctly rescaled. Furthermore, the actual source is a three-dimensional volume whereas the simulation domain is a two-dimensional plane: this inevitably affects the plasma volume generation and surface loss processes.

3.5.1 Background gas pressure

The time evolution of the macroparticle number N reads

$$\frac{dN}{dt} = S - L \tag{3.12}$$

where S and L are the source and loss terms respectively. In this simulation, the main plasma generation channels are the background gas ionization processes, whereas the loss term is given by both collisions and surface losses. In a first approximation, the right hand side of equation 3.12 can be written as

$$\begin{aligned} \frac{dN}{dt} &= N\, n_{bg}\, (\sigma_{ion} v) - N\, \frac{u_{Bohm}}{L_d} \\ &= n_p\, V\, n_{bg}\, (\sigma_{ion} v) - n_p\, V\, \frac{u_{Bohm}}{L_d} \\ &= n_p\, V\, n_{bg}\, (\sigma_{ion} v) - n_p A u_{Bohm} \end{aligned} \tag{3.13}$$

where σ_{ion} is an effective ionization cross section, v is the particle velocity, u_{Bohm} is the Bohm velocity and L_d is the domain characteristic dimension. The stationary state of Equation 3.13 yields two possible solutions: a trivial one $n_p = 0$, which is not physical, and a second one from which the background gas density can be derived as a function of the system volume and external surface

$$n_{bg} = \frac{A}{V} \frac{u_{Bohm}}{(\sigma_{ion} v)} \tag{3.14}$$

By assuming that the Bohm velocity and the reactivity are the same for both the real system and the simulated one, the background gas density is found to be proportional to the ratio A/V. Table 3.7 shows the ratio values for the real source and the simulated domain.

	real source	simulation
A	$3.91\,\mathrm{m}^2$	$1.09\,\mathrm{m}^2$
V	$0.33\,\mathrm{m}^3$	$0.07\,\mathrm{m}^3$
ratio	$11.80\,\mathrm{m}^{-1}$	$15.11\,\mathrm{m}^{-1}$

Table 3.7: Area and volume of the source and simulation domain.

The simulated background gas density inside the driver is then

$$n_{bg}^{PIC} \simeq 0.78\, n_{bg}^{fill} \tag{3.15}$$

and therefore the simulated plasma density should be larger than the experimental one so as to reproduce the actual filling pressure. In other words, the simulated plasma will reach a stationary state at a lower background gas density.

3.5.2 Debye length

The density scaling factor β is equal to 10^4 and, consequently, the simulated Debye length is a hundred times larger than the real one. This inevitably affects the sheath formation, although any correction can be neglected if the sheath thickness is much smaller than the domain characteristic dimension.

Chapter conclusion

The simulation code used in this thesis work was briefly introduced and a detailed description of the newly implemented features was provided. To conclude, a list of the most relevant simulation parameters is shown in Table 3.8, whereas the complete logical scheme is shown in Figure 3.8; in particular, the original, modified and new features are coloured with white, magenta and light blue respectively. The simulation time t is supposed to start either from 0 or from the last instant of the reloaded system.

Parameter	Symbol	Value
x-domain size	-	400 mm
y-domain size	-	400 mm
z-domain size	-	500 mm
timestep	dt	3.5×10^{-10} s
x-cell dimension	dx	0.001 m
y-cell dimension	dy	0.001 m
initial plasma density	n_0	10^{14} m^{-3}
maximum macroparticle number	-	16×10^6
macroparticle weight	MPW	1.6×10^6
density scaling factor	β	10000
left wall potential	-	0 V
right wall potential	V_{PG}	variable
bottom wall potential	-	0 V
top wall potential	-	0 V
bias plate potential	V_{BP}	variable
driver lateral potential	-	0 V
maximum magnetic field intensity	$\|B\|$	0 mT to 7 mT
driver heating temperature	T_{heat}	15 eV to 20 eV
driver heating frequency	ν_{heat}	PI-controlled
background gas density	n_{bg}	PI-controlled
dissociation rate	α	0.3

Table 3.8: Main `gppic` input parameters.

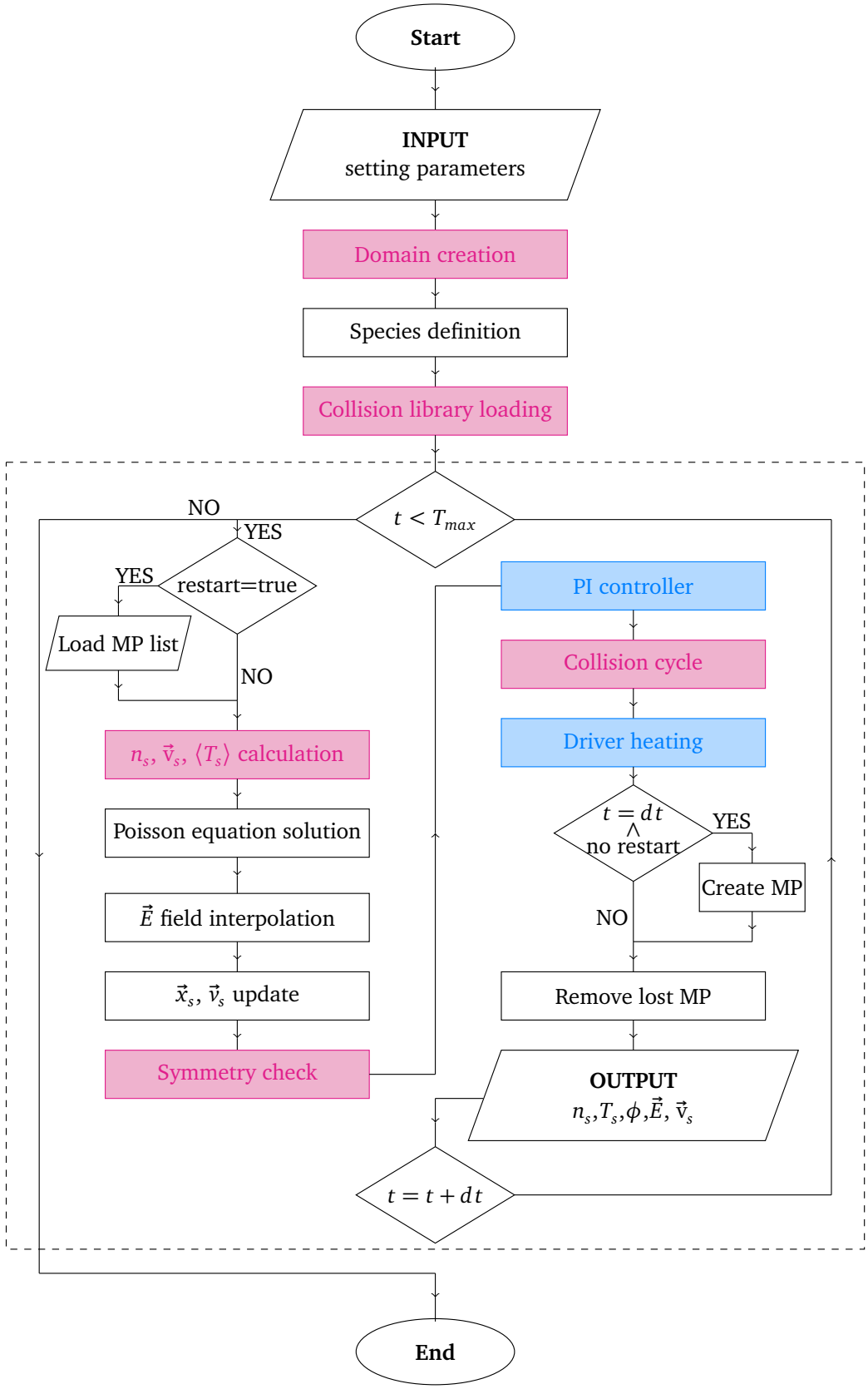

Figure 3.8: Overview of `gppic` logical scheme.

Chapter 4

Steps towards an integrated model

This chapter provides a description of all the physical ingredients needed for the simulation, namely: the magnetic field, which includes both the filter field and the permanent magnets field contributions, the electron heating mechanism and the background gas density. Some further information on the collision processes is given. Finally, the simulation of both the generation and expansion processes are described.

4.1 Magnetic field

As already mentioned in Section 3.2.1, the magnetic field used in these simulations is externally imposed and it is constant over time. Two main contributions are included, namely the *magnetic filter field* and the *confinement field* generated by the permanent magnets on the driver backplate. The physical role of both the aforementioned fields has already been discussed in Chapter 2, whereas their implementation and their effect on the overall simulation behaviour will be described in the following.

4.1.1 Filter field

The magnetic filter field is supposed to reach its maximum and minimum intensity within the expansion chamber and the driver region respectively. Nevertheless, the real filter field has a three-dimensional topology that cannot be reproduced with the simulation: indeed, the actual field lines display some curvature and, moreover, the field intensity is not constant in the source width. Both these 3D effects reduce the ease to choose an appropriate representative profile for the simulation.

The simulated filter field is assumed to be directed exclusively along the z direction so as not to interfere with the solution of the Poisson equation, which

instead is performed on the (x, y) plane. The field intensity is described as

$$B(x, y) = B_{min} + \frac{B_{max} - B_{min}}{2}\left[1 + \tanh\left(\frac{x - x_{half}}{s}\right)\right] \tag{4.1}$$

where B_{min} and B_{max} are the minimum and maximum field intensity respectively, x_{half} is the point along the driver axis in which the field intensity reaches half of its maximum and s defines the width of the intensity increase. As the expression in 4.1 depends explicitly only on the x coordinate, the field intensity is uniform along the y direction.

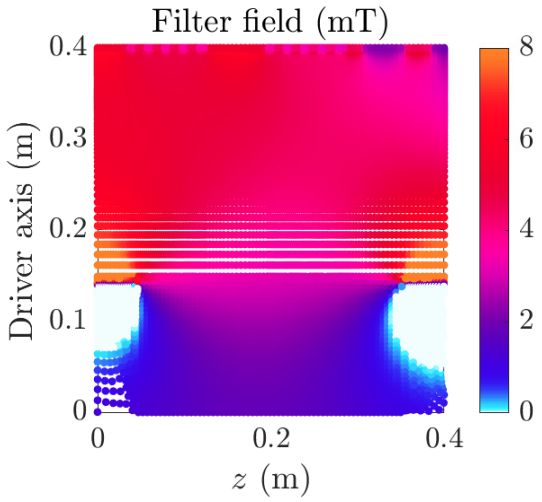

Figure 4.1: 2D-map of the SPIDER magnetic filter field.

Figure 4.1 shows a two-dimensional map of the actual source field. Recall that the simulation plane is perpendicular with respect to the one shown above. As expected, the field intensity is lower in the driver and increases in the expansion chamber, until the PG surface is reached.

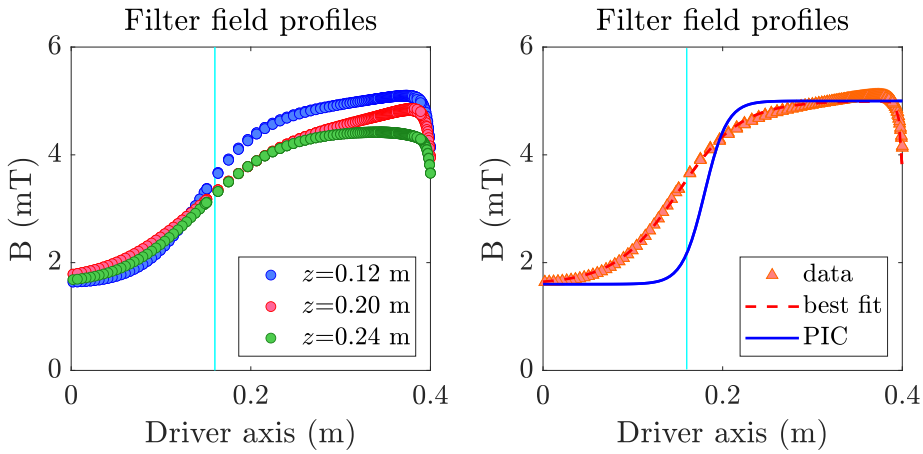

Figure 4.2: On the left: $\vec{B}$ profiles at different z positions taken from Figure 4.1. On the right: simulated field profiles.

The field profile depends on the chosen z position, as can be seen from Figure 4.2. In all three cases, the intensity decays rapidly in front of the PG as the filter currents are flowing in the latter. However, as the PG is not thoroughly reproduced by the simulation, the implemented profile is constant until it reaches the domain wall. The field intensity is not negligible in the driver region, where it also displays a relatively strong gradient along the driver axis.

The analytic function from Equation 4.1 is able to reproduce the profiles from Figure 4.2 with good accuracy. Despite this, the implemented profile is chosen to be slightly different so as to suppress the initial gradient, as the latter yields a wavy behaviour of the discharge in the driver; in order to limit the study to stable plasma regimes, it was decided to implement the blue profile rather than the red one from Figure 4.2, even though this results in worsening the plasma confinement. The filter field profile obtained for $z = 0.12\,\mathrm{m}$ was chosen with the aim of partially counterbalancing this side effect, as the latter displays the highest field value within the expansion chamber.

4.1.2 Driver backplate field

Some permanent magnets are placed on the driver backplate surface for confining the plasma. This effect was reproduced by considering an additional magnetic field contribution.

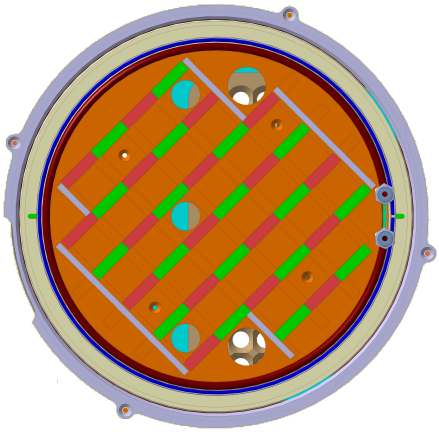

Figure 4.3: Permanent magnets on the driver backplate of the SPIDER source.

Also in this case, the field topology is three-dimensional and the field strength depends on the chosen section of the magnets grid shown in Figure 4.3. The implemented analytic function reads

$$B_{pm}(x,y) = |B|_{pm}^{max} \exp\left[-\pi\left(\frac{x}{0.02\,\mathrm{m}}\right)\right]\sin\left[\pi\left(\frac{y-0.2\,\mathrm{m}}{0.035\,\mathrm{m}}\right)\right] \tag{4.2}$$

where $|B|_{pm}^{max} = 20\,\mathrm{mT}$. The exponential decay along the x direction is needed to damp the field intensity in about 2 cm, whereas the sinusoidal modulation along the y direction allows to avoid possible additional drifts.

4.1.3 Overall magnetic field

The final magnetic field configuration is shown in Figure 4.4. The simulation plane is also represented for the sake of clarity. Recall that the field lines are always directed along the z direction, therefore negative values of B shall be construed as downwards pointing field lines.

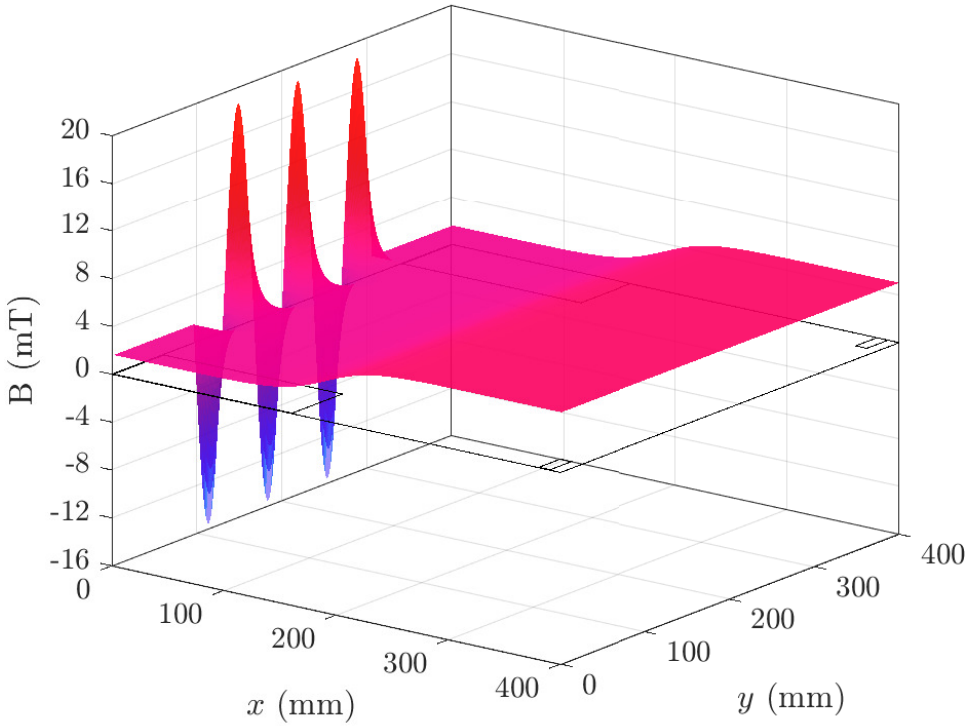

Figure 4.4: Final PIC magnetic field configuration.

4.2 Electron heating

The driver region features the highest values of both electron density and temperature. In the real source, the electrons inside the driver are heated through the inductive coupling between a coil wrapped around the driver vessel and the plasma itself: as a consequence, an oscillating electromagnetic field sets up in the outer layer of the plasma column, causing the electrons to accelerate along the poloidal direction. This de-Maxwellizing process[9] results in a high energy tail in the electron energy distribution function (EEDF), due to the localized heating in the external region of the driver. The deposited power is subsequently re-distributed among the electrons thanks to Coulomb scattering, which counterbalances the de-Maxwellizing effect in such a way that the driver's central region is continuously heated.

In order to describe this mechanism, time-varying magnetic fields should be included in the simulation: if this were to be the case, the used algorithm would be much more complex and the solution of both the Faraday law and the Ampère-Maxwell equation should be included. Furthermore, as Coulomb processes are indeed essential for the energy redistribution, the simulation of the inductive coupling mechanism should go hand in hand with an accurate description of the Coulomb interaction. This being said, it was decided not to thoroughly reproduce the real heating mechanism, as the ultimate goal of this thesis is the analysis of plasma uniformity in the expansion chamber.

The electron temperature inside the driver is determined by the thermostat (see 3.4.1), more precisely by the temperature T_{heat} at which the electron velocities are re-sampled and by the heating frequency ν_{heat}. Another fundamental aspect of the thermostat is its probability density function: an extended central peak as shown in Figure 4.5 has to be considered for reproducing the experimental profiles.

If a double-peak $f(x, y)$ such as the one shown in Figure 3.5 is used without including Coulomb collisions between the electrons, the resulting T_e distribution would be less similar to the measured one (see Section 4.2.2) because the electrons inside the driver would not thermalize and, as a consequence, the central driver region would be at a lower temperature with respect to the sheath region, leading to unlikely results.

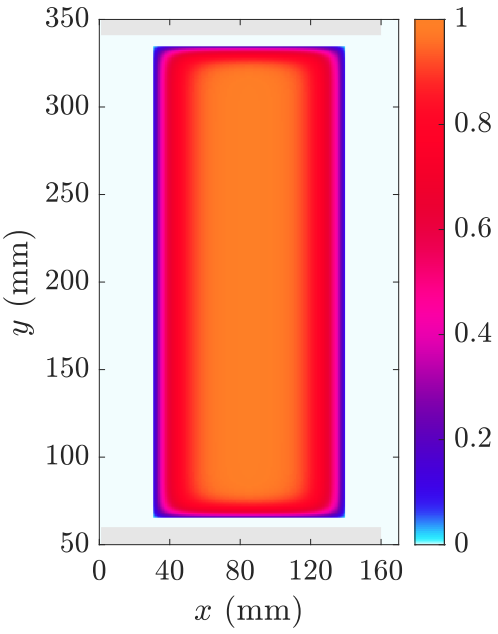

Figure 4.5: Thermostat $f(x, y)$ actually implemented in the simulation.

It was necessary to extend the probability peak as much as possible in such a way that the T_e value was significantly high also at the driver boundaries. As the driver region is small, the potential value is strongly affected by the temperature profile as further explained in Section 4.2.1. The analytic expression for the $f(x,y)$ function shown in Figure 4.5 reads

$$f(x,y) = \left[1 - \exp\left(\frac{|x - 0.085\,\mathrm{m}| - 0.055\,\mathrm{m}}{0.01\,\mathrm{m}}\right)\right] \cdot \left[1 - \exp\left(\frac{|y - 0.2\,\mathrm{m}| - 0.135\,\mathrm{m}}{0.004\,\mathrm{m}}\right)\right] \tag{4.3}$$

4.2.1 Influence on the potential profile

The potential drop across the plasma sheath depends also on the electron temperature as follows

$$\phi_p - \phi_w = \alpha \frac{T_e}{e} \tag{4.4}$$

where ϕ_p and ϕ_w are the plasma bulk and wall potentials respectively, T_e is the electron temperature expressed in eV, e is the elementary charge and α is a numerical constant that depends on the plasma composition; for hydrogen plasmas one obtains $\alpha = 3.3$, whereas for deuterium $\alpha = 3.7$. The potential drop increases for higher T_e values and, for this reason, the potential value at the driver center was found to be larger while extending the heating peak probability towards the driver walls.

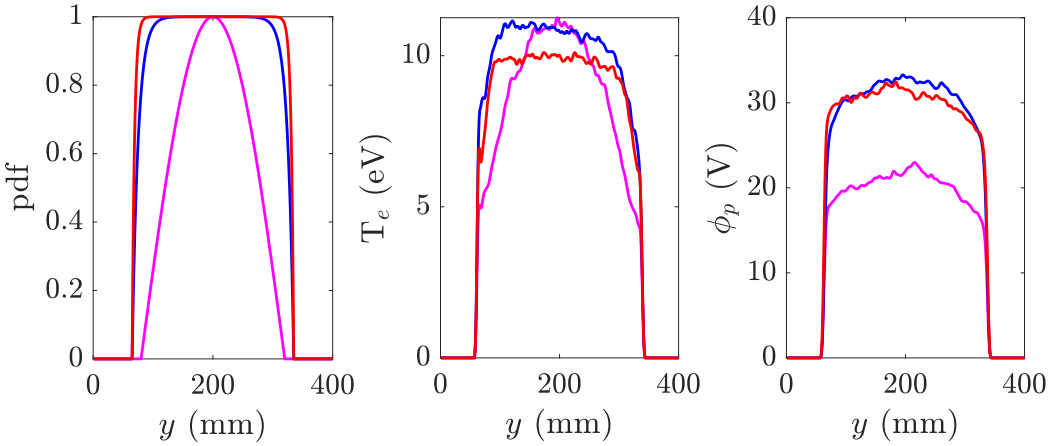

Figure 4.6: Comparison of plasma potential and electron temperature profiles obtained with different $f(x,y)$ shapes. All the profiles refer to $x = 0.08\,\mathrm{m}$.

As can be seen from Figure 4.6, approximately 10 V were gained by turning a cosine profile into an exponential one, while keeping the same central temperature value. As further evidence, it is possible to notice that the central temperature value does not affect the potential peak, as can be seen by comparing the red and blue

profiles from the same Figure. This particular correlation between the plasma potential and the electron temperature at the walls might be due to the simultaneous presence of both the magnetic filter field and the thermostat.

4.2.2 Attempt at reproducing the skin effect

In order to reproduce the skin effect, a double peak $f(x, y)$ distribution such as the one shown in Figure 3.5 was tested. The driver's central region was found not to be correctly heated, probably due to the lack of the description of Coulomb interaction between the electrons. The heating temperature T_{heat} was needed to be significantly high, namely $\geq 20\,\text{eV}$, so as to reach a reasonable temperature value also in the driver center: as a consequence, the plasma potential was found to be much higher with respect to the one obtained with a single peak $f(x, y)$. On this basis, the implementation of the aforementioned double peak distribution was abandoned, also considering that the aim of the thermostat is to reproduce the experimental electron temperature profile rather than the electron heating mechanism.

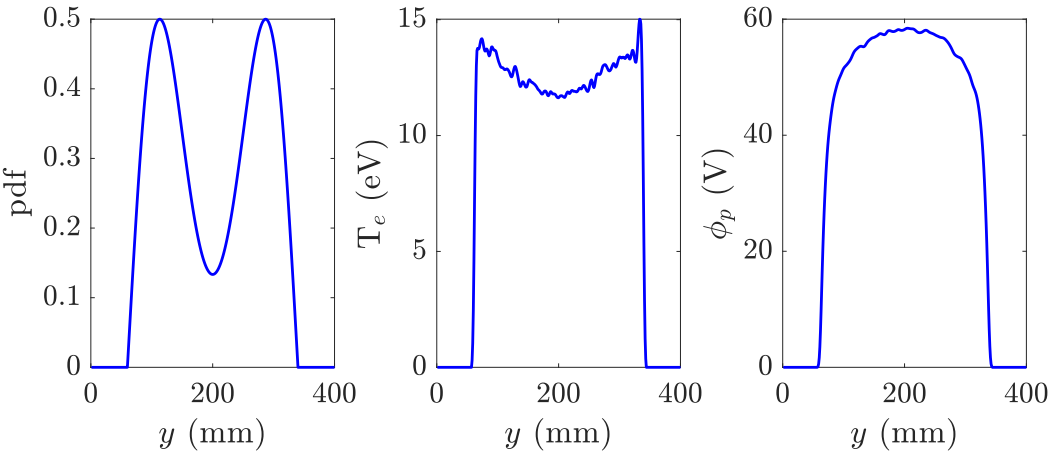

Figure 4.7: Effect of a double-peak thermostat pdf on temperature and potential profiles inside the driver. All the profiles refer to $x = 0.08\,\text{m}$.

4.3 Neutral depletion effect

Before starting the operations, the source vessel is filled with a neutral hydrogen or deuterium gas at a given pressure p_{fill}. However, as soon as the plasma is generated, the background gas temperature increases due to the plasma-gas interaction and, as a consequence, its density will decrease[30]. This phenomenon is called neutral depletion and it must be taken into account when performing a simulation, as the background gas density directly affects the collision rates and thus the discharge equilibrium. According to several measurements performed in the SPIDER source, the gas pressure in the expansion chamber is about 70% of the total filling pressure.

p_{fill} (Pa)	p_p (Pa)	ratio
0.25	0.18	0.74
0.34	0.25	0.73
0.72	0.56	0.78
0.53	0.39	0.74

Table 4.1: Pressure measurements performed in the SPIDER source for different filling pressures.

This being said, it is also true that the plasma density is significantly higher in the drivers and, therefore, the gas temperature in this region will be larger: this results in a non-uniform gas density inside the source. In order to take all the aforementioned effects into account, the simulated gas density is assumed to be analytically described as

$$n(x,y) = n_{fill}\left[\frac{1}{3} + \frac{1}{6}\left(1 + \tanh\left(\frac{x - 0.15\,\mathrm{m}}{0.05\,\mathrm{m}}\right)\right)\right] \tag{4.5}$$

so that $n(x,y)$ will be approximately equal to one third of n_{fill} inside the driver and then doubles in the expansion chamber, as shown in Figure 4.8. Also in this case, Equation 4.5 shows no explicit dependence on the y variable, therefore the density is uniform along the vertical direction. Furthermore, the dissociation rate is assumed to be 0.3 and it is constant over the entire domain.

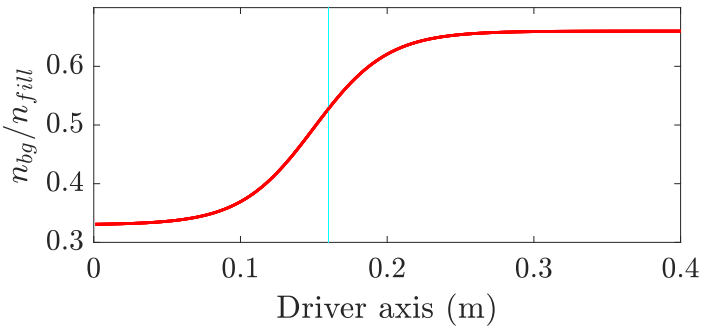

Figure 4.8: Ratio between the source and filling background gas densities as a function of the position along the driver axis.

4.4 Collision rates

In order to obtain a rate driven equilibrium, it is important to describe in as specific a manner as possible all the interaction processes occurring in the real source. The generation and destruction rates need to reach a reasonable balance, so that the simulated discharge can self-sustain. The main generation channels are the ionization of both gas molecules and atoms via electron impact

$$\begin{aligned} e^- + \mathrm{H_2} &\rightarrow e^- + \mathrm{H_2^+} + e^- \\ e^- + \mathrm{H} &\rightarrow e^- + \mathrm{H^+} + e^- \end{aligned} \tag{4.6}$$

whereas other processes such as negative ion or fast atom ionization exhibit significantly lower cross sections, as can be seen from Figure 4.9. Both reactions in Equation 4.6 are threshold processes, as the electrons need to have enough energy to ionize the molecules and atoms respectively: for this reason, it is important to heat the electrons inside the driver so as to trigger plasma generation.

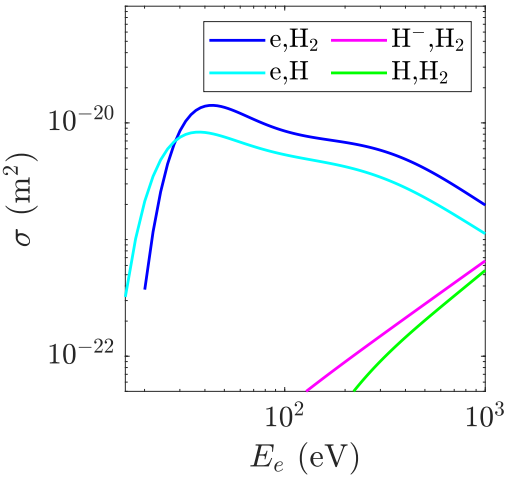

Figure 4.9: Cross sections of the included ionization processes.

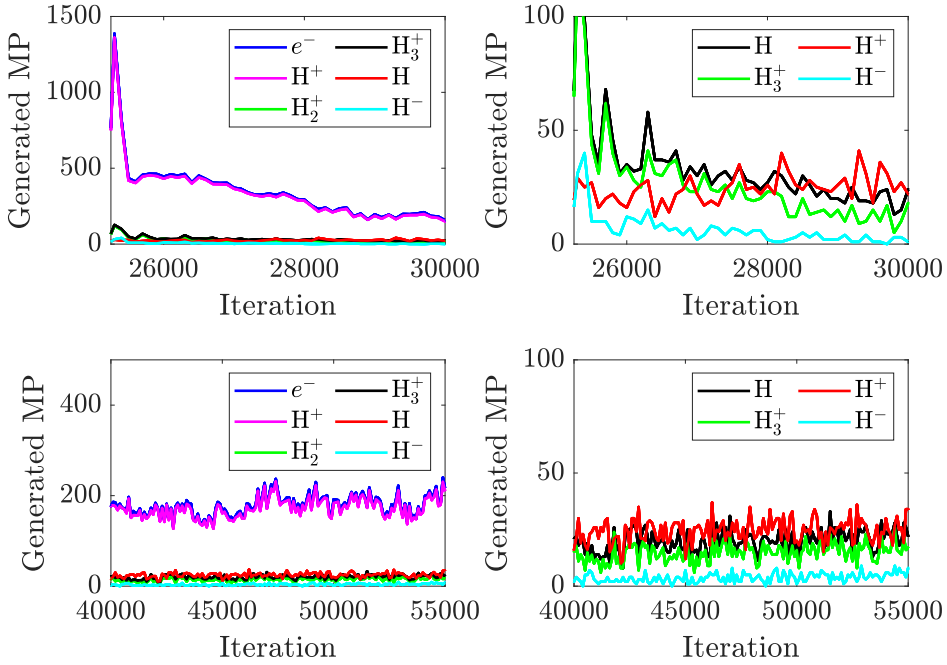

Figure 4.10: MP generation rates during the expansion process (first row) and at equilibrium (second row). The PI control is active.

Figure 4.10 shows the macroparticle generation rates at each iteration. The effect of the PI control can be seen from the high initial rates of e^- and H_2^+ production, which are related to the background gas density increase. As shown in the figures on the first row, the main plasma generation channel is the electron impact ionization of molecular hydrogen, as expected. With the exception of electrons and molecular ions, all the other species are created with a significantly lower probability. The second row in Figure 4.10 shows the generation rates at equilibrium: after the initial transient state, all the rates seem to converge to a stable value. The PI effect is still visible in both the e^- and H_2^+ rates, where some oscillations appear: the latter are strictly related to the background gas density variations, as further explained in Section 4.5.1.

4.4.1 Low-energy electron impact processes

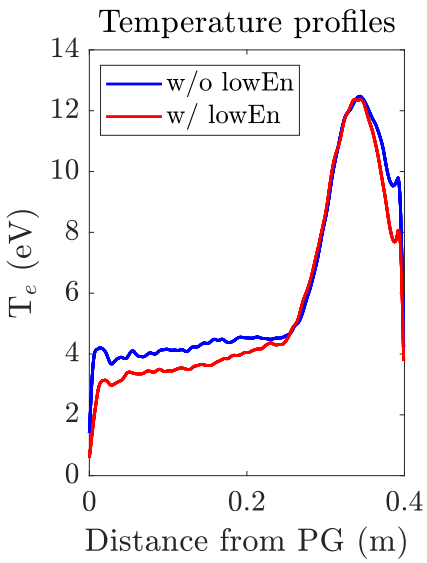

Figure 4.11: Effect of low energy electron impact processes on T_e.

On one hand, highly energetic electrons are of fundamental importance for the ionization processes, hence for plasma generation. On the other hand, it is also important to correctly describe the interaction between the background gas and slow electrons: indeed, these collisions were found to be the main channel for energy loss in the expansion chamber. The considered processes are

$$\begin{aligned} e^- + H_2[J=0] &\rightarrow e^- + H_2[J=2] \\ e^- + H[n=1] &\rightarrow e^- + H[n'] \end{aligned} \tag{4.7}$$

where $n' \in [2,5]$ is an excited atomic state of the hydrogen atom. As can be seen from Figure 4.11, by adding these processes the electron temperature in the expansion chamber decreases by 1 eV. Coulomb collisions between the electrons and plasma ions also contribute to lower the electron temperature.

4.4.2 Generation of fast atoms

Fast atoms can be generated because of collision processes: it is important to keep track of these particles as they are the precursor species for negative ions, which are mainly produced at the PG surface, and also because they are likely to become protons via charge exchange. Nevertheless, the simulation algorithm used in this thesis work does not include caesium and, consequently, there are no significant destruction channels for the newly generated atoms. This might result in a quite rapid depletion of GPU memory, undermining the obtained results. On this basis, not all the atoms are effectively created, although the algorithm keeps track of the total number of newly born neutrals at each iteration.

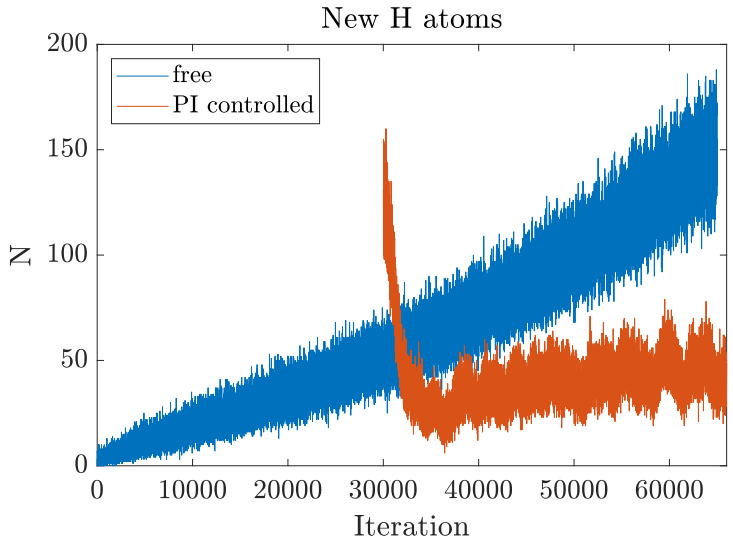

Figure 4.12: Produced H atoms that are not actually included in the simulated plasma. The jump at iteration 30000 is due to the PI control.

Both graphs in Figure 4.12 represent the number of produced H atoms that are not actually included in the simulation. The blue trend is referred to a free evolution, whereas the orange one has been obtained with active PI control. The disconnection at iteration 30000 is due to the PI itself, that increases significantly the background pressure in such a way to favour the plasma generation process, as further explained in Section 4.5.1. Nevertheless, after the initial transient regime, the orange trend reaches a stationary state, whereas the blue one is still growing in an exponential way.

4.4.3 Coulomb collisions

The Coulomb scattering between electrons and plasma ions was included with the aim of lowering the electron temperature in the expansion chamber, so that the experimental results for higher background gas pressures could be better reproduced: indeed, T_e was found to decrease by about 0.5 eV.

An attempt was made to implement Coulomb collisions between particles with the same charge, i.e. e^--e^- and ion-ion interactions. However, these processes were not actually included in the simulations as they provided several issues. Coulomb collisions between the electrons would have been of fundamental importance for simulating the inductive coupling between the antenna and the driver: in any case, as this process is not included in the `gppic` code, the simulation results are not strongly affected.

4.5 Reproducing plasma generation and expansion

When no previously saved configurations are loaded, the simulation starts from an arbitrary plasma distribution with the sole constraint of quasi-neutrality. The plasma generation and expansion mechanism are then self-consistently reproduced, and the plasma particles manage to fill the entire simulation domain.

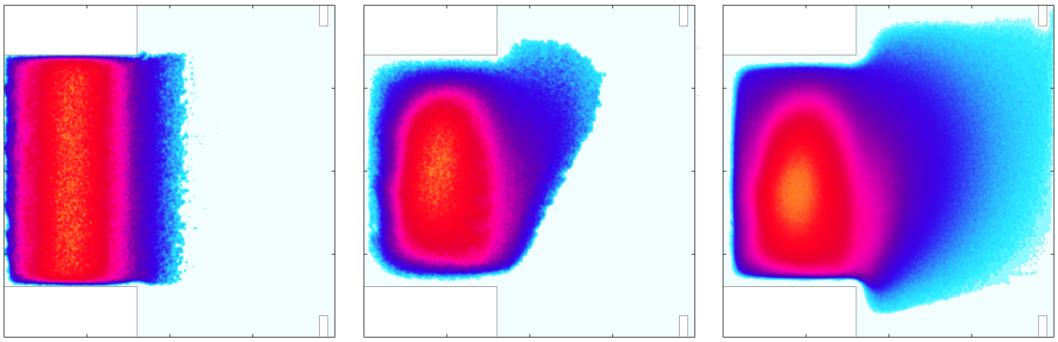

Figure 4.13: Electron density obtained at three subsequent time steps during the generation and expansion process.

As can be seen from Figure 4.13, the particles are initially localized within the driver region. They are gaussian distributed along the driver axis, while they are uniformly distributed along both the y and z directions. The starting plasma composition can be arbitrarily chosen: for instance, it is possible to generate only (e^-, H^+) pairs or to include also some (H^-, H^+) and (e^-, H_2^+) pairs.

The choice of reproducing plasma generation partially stems from the fact that the simulation is not able to work correctly if the entire domain is populated with equal ion density, especially because the characteristic response time of the simulation is much faster in response to particle increase (volumetric production) rather than losses (mostly at walls). In the early simulations, the magnetic filter field separates the driver plasma from the expansion region plasma and, moreover, the discharge is no longer sustained.

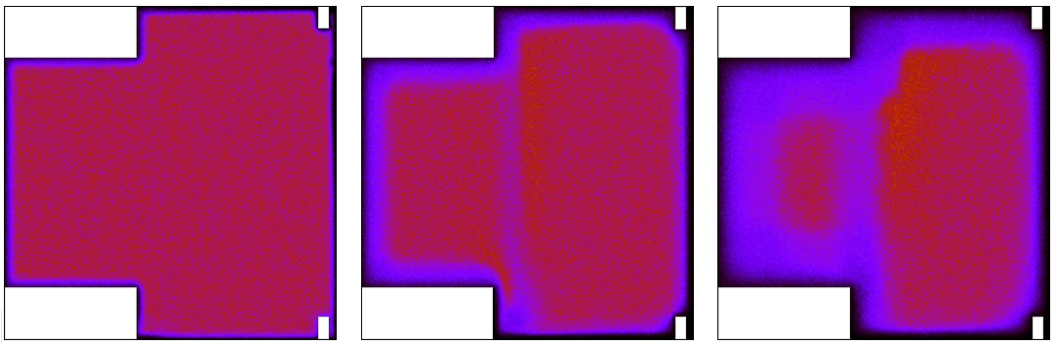

Figure 4.14: Electron density obtained at three subsequent time steps after pre-populating the entire domain.

Nevertheless, by letting the simulation evolve without constraints, the final plasma composition is more likely to be similar to the experimental one, provided that the correct collision processes and cross sections are included.

4.5.1 PI convergence

Once the generation and expansion processes have started, the PI controller can be used to tune the simulated electron density and temperature inside the driver so as to match the experimental values. As already mentioned in Section 3.4.2, the background gas pressure is not limited to a maximum value: for this reason, the simulation evolves freely for a certain number of iterations (>20000). As soon as the central driver density is equal to or greater than 75% of the target value, the PI control starts operating.

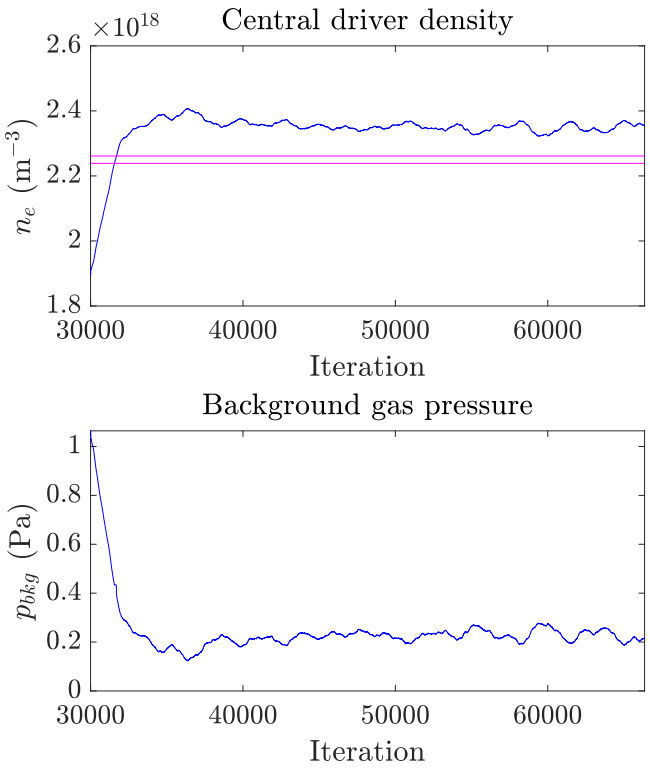

Figure 4.15: Example of PI convergence for the electron density. The magenta lines in the two upper figures represent the tolerance interval.

The examples shown in Figures 4.15 and 4.16 represent the PI convergence of a simulation that started from a previously saved configuration in which the system was allowed to evolve freely. The background gas pressure peak can be explained as follows: as the average driver density is much smaller than the target value, the PI significantly increases p_{bkg} in order to provide higher ionization rates. This peak can be related to the increase in the H atoms number from Figure 4.12, as both trends are obtained from the same simulation.

As soon as the electron density grows, the pressure value starts to decrease until it reaches a stationary state, in this case at $p_{bkg} \approx 0.2\,\text{Pa}$. It might be argued that the amplitude of the pressure oscillations is not negligible; on the other hand, the values shown in Figure 4.15 should be considered as "instantaneous", whereas an actual illustrative quantity would be the p_{bkg} average over a sufficient number of iterations. Furthermore, the simulated filling pressure is approximately equal to 0.6 times the real pressure $p_{fill}^{exp} = 0.34\,\text{Pa}$, not too far from the result obtained in Section 3.5.

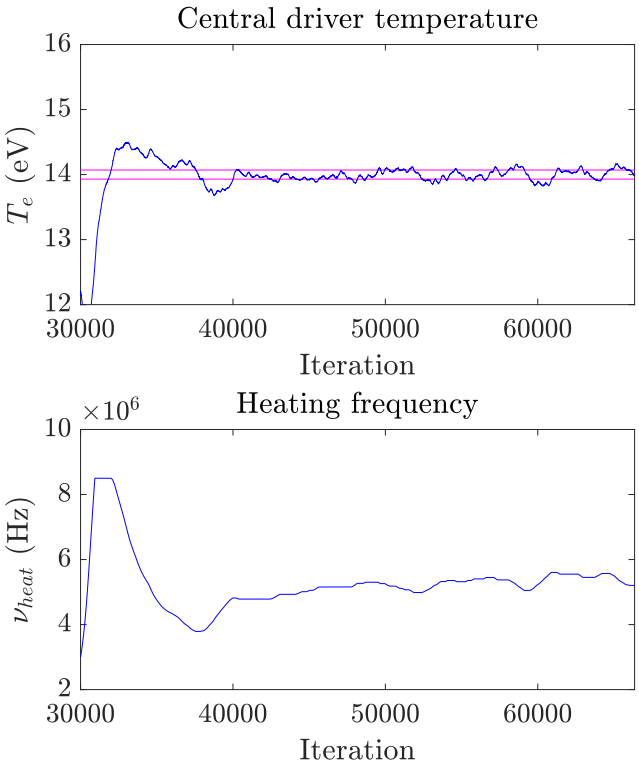

Figure 4.16: Example of PI convergence for the electron temperature. The magenta lines in the two upper figures represent the tolerance interval.

The temperature convergence is considerably better than the pressure one, possibly because of the thermostat: in fact, the driver electron temperature is somehow "artificially" obtained, whereas the density value is mostly determined by the collision processes.

Chapter conclusion

The newly implemented features of `gppic` were discussed and motivated in this chapter. The most important limitations of the simulation code have been described, namely the adaptation of the magnetic filter field profile, the lack of a comprehensive description of the inductive coupling and the drawbacks of the PI controller. Some insights on the possible future improvements will be provided in the last chapter of this thesis. To summarise, the plasma generation and expansion processes can be reproduced with both good accuracy and control. Moreover, the collision rates can be derived and the discharge equilibrium can be analysed. By comparing the simulated profiles with the experimental ones, more information on the involved processes can be obtained and the numerical code can be further improved.

Chapter 5

Comparison with experimental results

A brief overview of the reference PIC simulation codes is provided in this chapter. The simulation results are discussed, together with their analysis and comparison with the experimental data taken from SPIDER. More precisely, the influence of the magnetic filter field, of the background gas density and of the bias plate voltage will be described.

5.1 State of the art

Several PIC codes have been developed in order to investigate the operation of a negative ion source. Most of the existent numerical tools allow to reproduce a single driver source with an externally imposed magnetic filter field. The PG is either described as a plain polarized wall[31] or as a multiaperture grid[32]: in the second case, the plasma extraction and the meniscus formation can be analysed too. A detailed implementation of the inductive coupling mechanism is usually not included, as it would be much more difficult and the final computing time could be much larger.

These codes were already able to highlight non-uniformities in the source and to provide an explanation of the related causes, i.e. drift motions, and to describe the plasma meniscus formation with good accuracy.

The `gppic` code was developed while taking the aforementioned ones as a reference and, furthermore, some new features were introduced with the present work:

- PI control on gas density and heating frequency;
- The neutral depletion effect was included by considering a non-uniform gas density;

- The magnetic filter field was extended also in the driver region, as this contribution is not negligible in the SPIDER case.

In addition, as already mentioned in Section 3.4, a self-consistent description of both the plasma generation and expansion process was achieved, together with a rate-driven equilibrium. The latter are possibly the most interesting aspects of this work.

5.2 Reproducing the SPIDER experimental trends

The experimental data used in this thesis work have been recently measured in the SPIDER source. The plasma properties and uniformity were investigated by means of movable electrostatic probes, properly designed to operate both in the expansion chamber and in the drivers, where the physical conditions can be challenging. The complete set of diagnostics includes 10 Langmuir probes, of which 8 single, 1 double and 1 triple, and a Mach probe. Table 5.1 summarises some of the investigated aspects and the related simulated conditions.

Physical aspect	I Case	II Case
Filter field effect on plasma properties	$\vec{B}_{filt} = 0$	$\vec{B}_{filt} \simeq \vec{B}_{exp}$
Gas density influence on density profiles	$p_{fill} = 0.34\,\text{Pa}$	$p_{fill} = 0.70\,\text{Pa}$
Bias Plate effect on n_e density at the PG	BP=14.3 V	BP=43 V

Table 5.1: Brief overview of the analysed conditions. A comparison with the experimental data has been performed in every case.

5.2.1 Low vs high gas pressure

SPIDER is designed to operate at a gas pressure of 0.3 Pa. Nevertheless, an investigation at higher pressures was carried out to verify whether better operating conditions can be identified, and to test if the usable pressure range could be extended. The reference values were chosen to be 0.34 Pa and 0.70 Pa for the low and high pressure regimes respectively.

Figure 5.1 shows both the experimental and simulated results obtained in the low pressure regime at three different y positions. Both the electron density and temperature profiles match the experimental results. The T_e decrease in the expansion chamber is reproduced with high accuracy, implicitly proving that the chosen filter field profile is appropriate. The density profile instead is qualitatively similar, although both the peak height and position do not perfectly match the experimental points and, furthermore, the simulated density is slightly higher at the driver exit. The time-averaged numerical filling pressure is $\simeq 0.24\,\text{Pa}$, that is slightly smaller than the expected value $80\% \times 0.34\,\text{Pa} = 0.27\,\text{Pa}$. This being said, the plasma potential ϕ_P features the most relevant differences between the numerical and measured profiles. The driver peak at 60 V is missing: this can be related with the results from

Section 4.2.1. As the simulated plasma potential at the driver center strongly depends on the electron temperature at the sheath, the choice of not reproducing the inductive coupling might cause the simulated plasma potential profiles to be lower in this region: indeed, as seen in Figure 4.6, a double-peak electron heating region leads to a maximum potential of $\approx 58\,\mathrm{V}$, that is much closer to the experimental value.

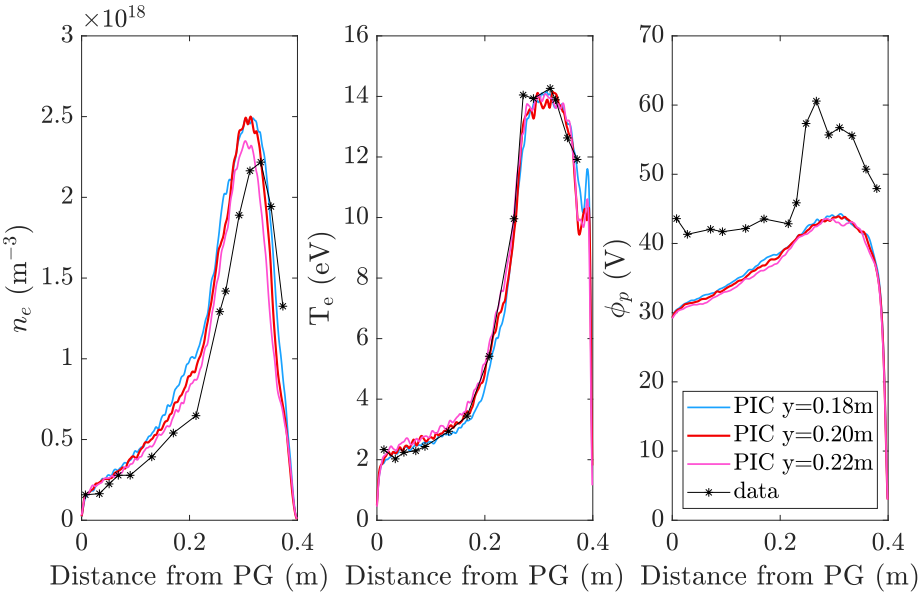

Figure 5.1: Low p_{bg} regime: comparison between simulated and measured n_e, T_e and ϕ_p profiles.

The n_e profiles taken at different heights are not completely overlapping. This is a clear sign of plasma asymmetry in the source, as can be seen from Figure 5.2.

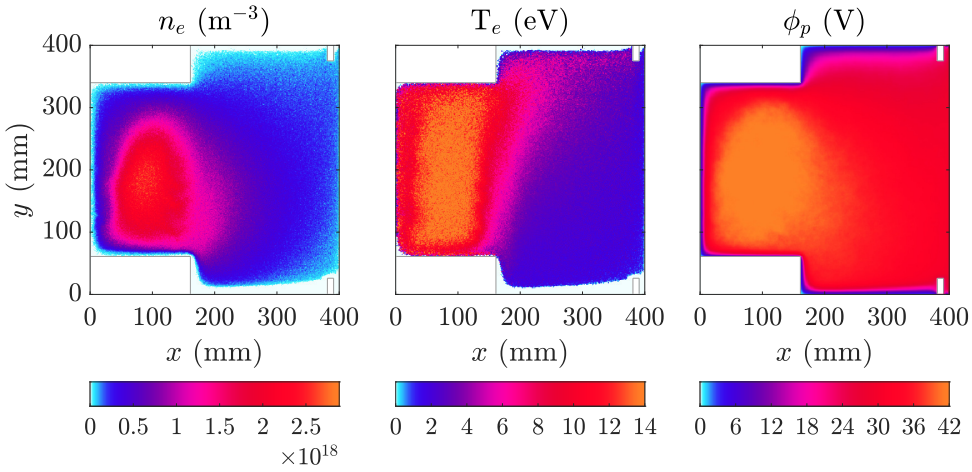

Figure 5.2: Low p_{bg} regime: 2D maps of simulated n_e, T_e and ϕ_p. The vertical asymmetry is evident in the first two maps.

The non-uniformity in the two-dimensional maps is strictly related to drift motions, as shown later in this section. The density peak in the driver is not centered because the magnetic filter field couples with the electric field resulting in a vertical shift for n_e; indeed, $\vec{B}_{filt}$ inside the driver was set to 1.6 mT rather than 0 mT.

Plasma composition

The driver plasma was found to be mainly composed of electrons and H_2^+ ions, as a direct consequence of molecule ionization. On the other hand, within the expansion chamber, H^+ ions account for more than a half of the total ion population (see Figure 5.3).

The H^- density is not high since only volume production is considered. The formation of the ion-ion layer in front of the PG, which in this simulation is polarised to 29 V, is not visible. This can be explained as follows: the PG potential is significantly lower than the plasma potential, therefore negative ions are somehow trapped into the bulk region. Furthermore, as surface production is not included, the number of produced H^- is not sufficient for the anions to become the dominant negatively charged species. If the PG voltage were even slightly higher than ϕ_p, a significant increase of the H^- density would actually ensue.

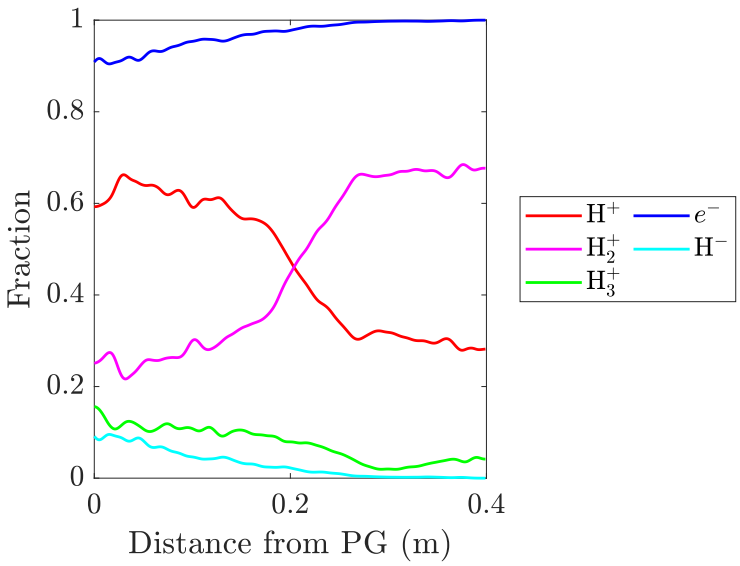

Figure 5.3: Low p_{bg} regime: plasma composition. The H^+, H_2^+ and H_3^+ are calculated with respect to the total positive ion population, whereas the e^- and H^- ones with respect to the total number of negative charges.

Although the trends shown in Figure 5.3 provide some useful information on the plasma properties, it is worth pointing out that there are still some missing mechanisms that might affect these results, which will be further discussed in Chapter 6.

Currents

The effect of the drift motions is clearly visible from the two-dimensional map representing the electron current, as shown in Figure 5.4. The $\vec{E} \times \vec{B}$ drift causes the e^- to form a vortex inside the driver, as the electric field is always pointing outwards. Furthermore, the vertical diamagnetic drift is visible at the driver exit.

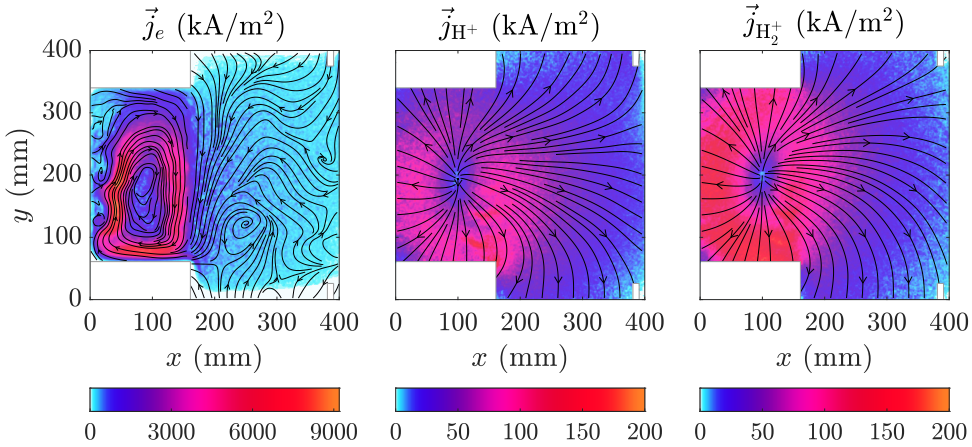

Figure 5.4: Low p_{bg} regime: e^-, H^+ and H_2^+ current direction and intensity.

Both H^+ and H_2^+ ions are repelled from the plasma bulk because of the potential drop. As expected, the current streamlines are approximately symmetric and no drifts are visible since ions are practically unmagnetised.

Figure 5.5 shows the n_e, T_e and ϕ_p maps in the high pressure regime. Also in this case, plasma asymmetry is clearly visible.

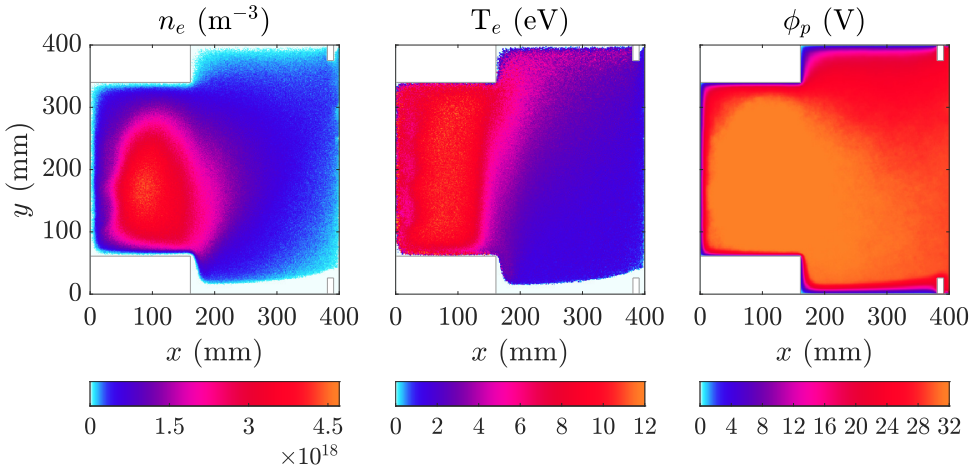

Figure 5.5: High p_{bg} regime: 2D maps of simulated n_e, T_e and V_p. The vertical asymmetry is evident in the last two maps.

Figure 5.6 provides the comparison between the simulated and measured n_e, T_e and ϕ_p profiles at three different y positions in the high pressure regime. The agreement between the numerical and experimental results is fairly good, even though some important differences can be seen in all three profiles. In fact, the simulated T_e in the expansion chamber is almost 1 eV higher than the measured one: this is probably due to some missing low-energy electron processes. The plasma potential is more similar to the measured one with respect to the $p = 0.34$ Pa case, although the driver's central peak is still missing. Finally, the time-averaged numerical filling pressure is $\simeq 0.33$ Pa, smaller than the expected value $80\% \times 0.7$ Pa $= 0.56$ Pa.

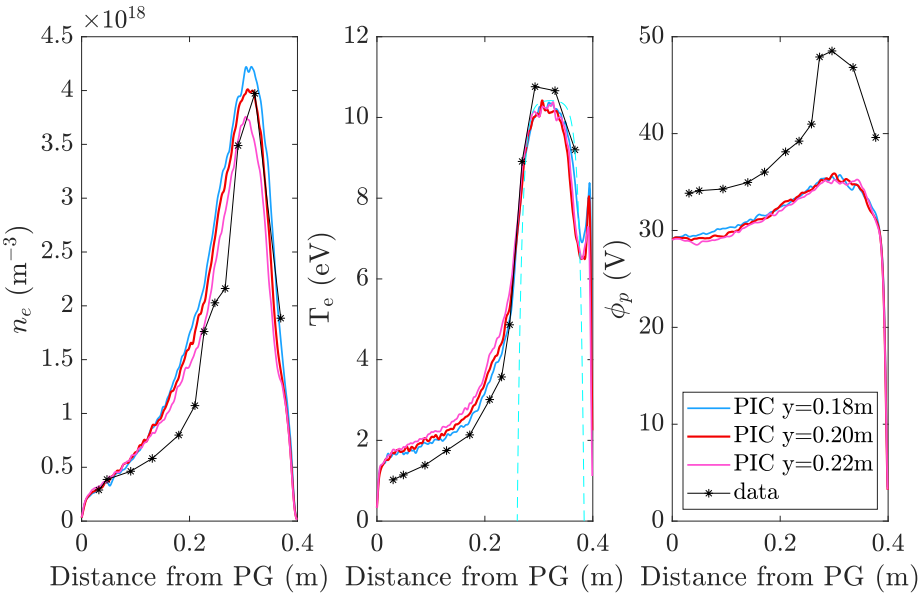

Figure 5.6: High p_{bg} regime: comparison between simulated and measured n_e, T_e and ϕ_p profiles.

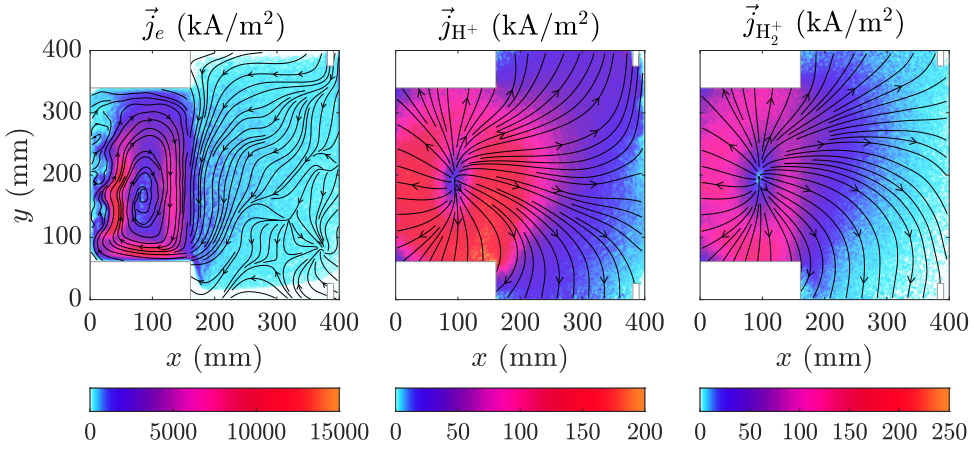

Figure 5.7: High p_{bg} regime: e^-, H^+ and H_2^+ current direction and intensity.

	Low p	High p	
$j_{e^-}^{MAX}$	$9.2 \times 10^3\,\mathrm{kA/m^2}$	$1.24 \times 10^4\,\mathrm{kA/m^2}$	+35%
$j_{H^+}^{MAX}$	$1.73 \times 10^2\,\mathrm{kA/m^2}$	$2.20 \times 10^2\,\mathrm{kA/m^2}$	+27%
$j_{H_2^+}^{MAX}$	$1.80 \times 10^2\,\mathrm{kA/m^2}$	$1.49 \times 10^2\,\mathrm{kA/m^2}$	-17%

Table 5.2: Comparison between the maximum current intensities in the low pressure and high pressure regimes.

Figure 5.7 shows the intensity and direction of plasma currents. The current direction for all the considered species is similar to the low pressure case whereas the current intensities are different, as can be seen from the values listed in Table 5.2. The H^+ and H_2^+ currents have now respectively increased and decreased in a significant way with respect to the low pressure regime: this is possibly related to the plasma composition variation which, in turn, might be due to some changes in the collision rates. Indeed, as can be seen from Figure 5.8, the H^+ density in the driver region increases with higher background gas pressure. The fraction of negative H ions has also increased. This can be explained by comparing the T_e profiles from both regimes: at a distance of 20 cm from the PG, the electron temperature in the low pressure regime is approximately equal to 4 eV, whereas in the high pressure regime $T_e \approx 2$ eV.

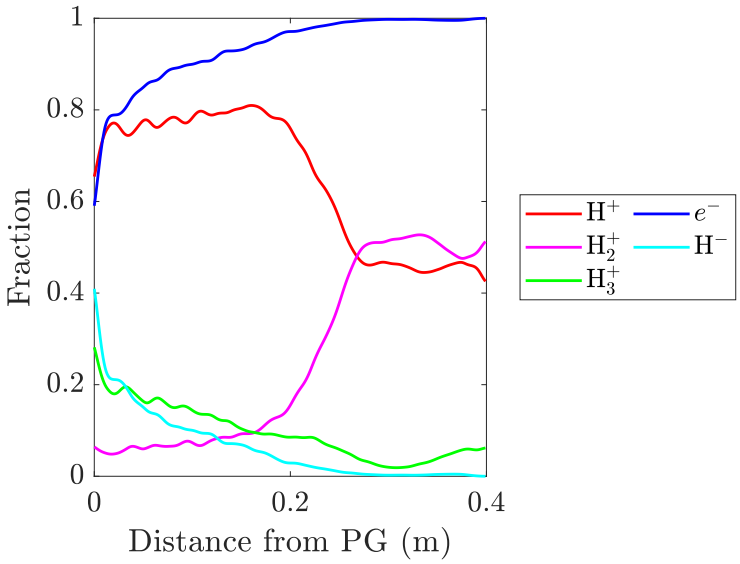

Figure 5.8: High pressure regime: plasma composition. The H^- and H^+ densities are significantly higher with respect to the low pressure regime.

5.2.2 Low vs high PG and BP voltages

The obtained results for PG=BP=43 V and PG=BP=14.3 V are discussed in this section. Figure 5.10 shows the simulated n_e, T_e and ϕ_p profiles in both regimes.

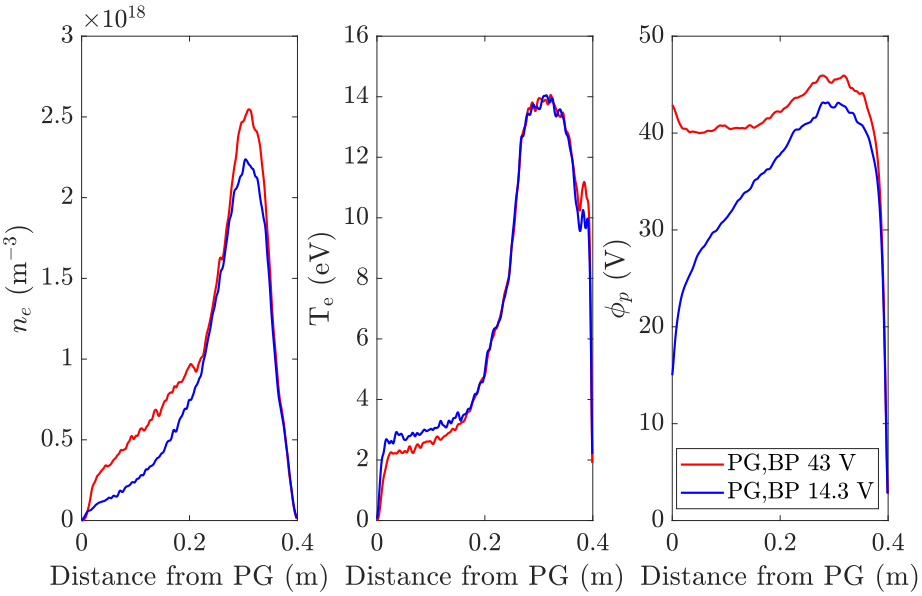

Figure 5.9: Comparison between simulated n_e, T_e and ϕ_p profiles in both bias regimes.

As expected, higher PG and BP voltages result in higher plasma density in the expansion chamber, as the negative charges are attracted towards the extraction region. The discrepancy between the n_e maximum values is likely due to the action of the PI control.

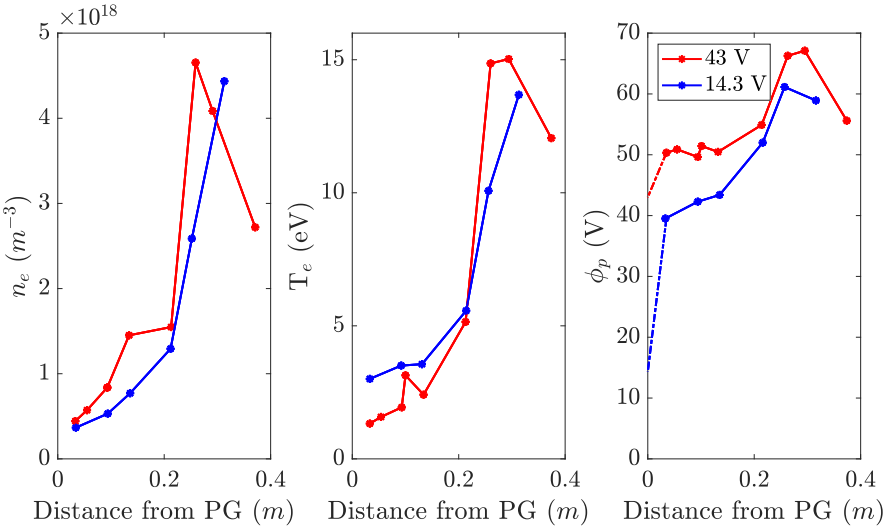

Figure 5.10: Comparison between measured n_e and T_e profiles in both bias regimes.

The electron temperature decreases by $\approx 1\,\text{eV}$, whereas ϕ_p in the driver region increases by $\simeq 2$ or $3\,\text{V}$ in the high voltage regime. A similar behaviour was also deduced from the measured data, which are shown in Figure 5.10. In this case, the experimental and simulated results are not directly comparable because the underlying conditions are different. However, both the electron density and temperature follow the same trends: their values in the expansion chamber are respectively higher and lower in the high voltage regime, as already verified with the simulated profiles.

The electron temperature decrease is possibly related to the significant variation of the plasma composition in the proximity of the grids; as can be seen from Figure 5.11, the ion-ion layer has almost completely formed in the high PG and BP voltage regime. In the last centimeters of the expansion chamber, the plasma is mostly composed of heavy positive ions, H_2^+ and H_3^+, and negative ions H^-.

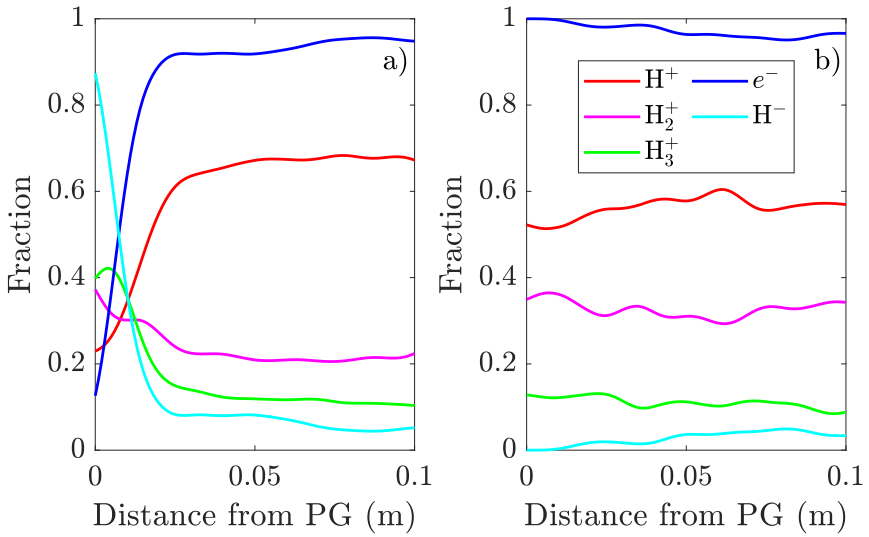

Figure 5.11: Comparison between plasma composition obtained with high (a) and low (b) PG and BP voltages. Only the last 10 cm of the expansion chamber are shown as the plasma composition in the remaining region does not feature significative variations.

5.2.3 Effect of the magnetic filter field

The influence of the magnetic filter field was investigated by letting the low-pressure simulation from Section 5.2.1 evolve after turning off the magnetic filter field $\vec{B}_{filt}$. The obtained results are completely self-consistent, as the PI control was disabled.

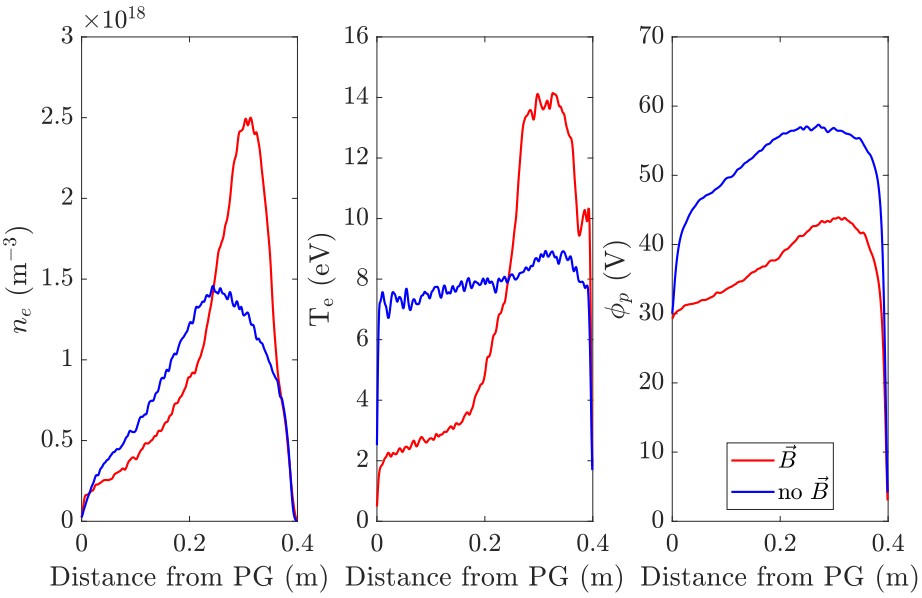

Figure 5.12: Comparison between simulated n_e, T$_e$ and ϕ_p profiles in the magnetised (red) and unmagnetised regimes (blue).

As expected, the T$_e$ value in the expansion chamber has significantly increased since fast electrons can now travel freely towards the PG; for the same reason, the n_e peak in the driver is less pronounced.

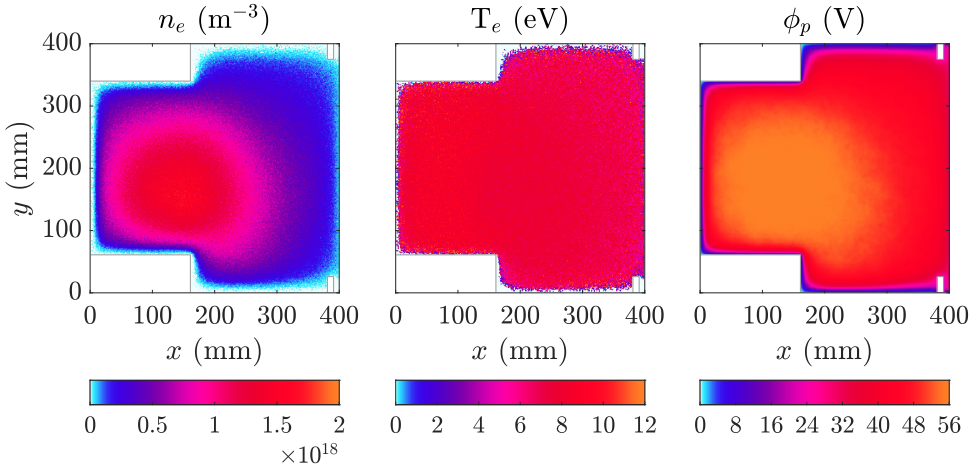

Figure 5.13: No filter field: n_e, T$_e$ and ϕ_p two-dimensional maps.

The absence of $\vec{B}_{filt}$ results in more symmetric maps of both electron density

and temperature and of plasma potential, as can be seen from Figure 5.13. The plasma potential in the unmagnetised case is much higher: the same behaviour was verified in the SPIDER source, as shown in Figure 5.14. This is a direct consequence of the electron temperature increase in the expansion chamber and it is worth to notice that this explanation cannot be straightforwardly deduced from the numerical ϕ_p profile, as in the latter case the plasma potential has significantly increased also in the driver region.

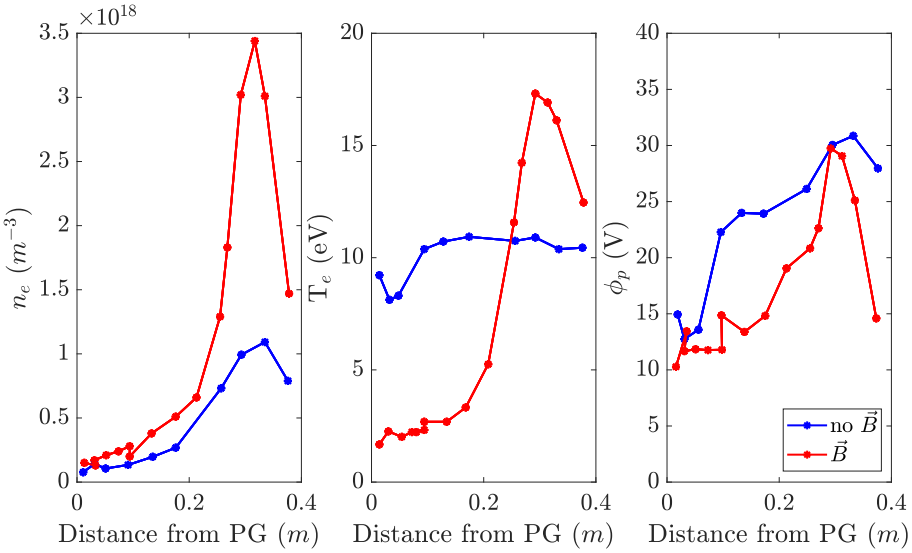

Figure 5.14: Measured n_e, T_e and ϕ_p profiles with and without filter field.

The electron density decreases and the T_e profile becomes flat in both the simulated and measured profiles. Furthermore, the electron current topology is much more similar to the ion one as the plasma is now unmagnetised.

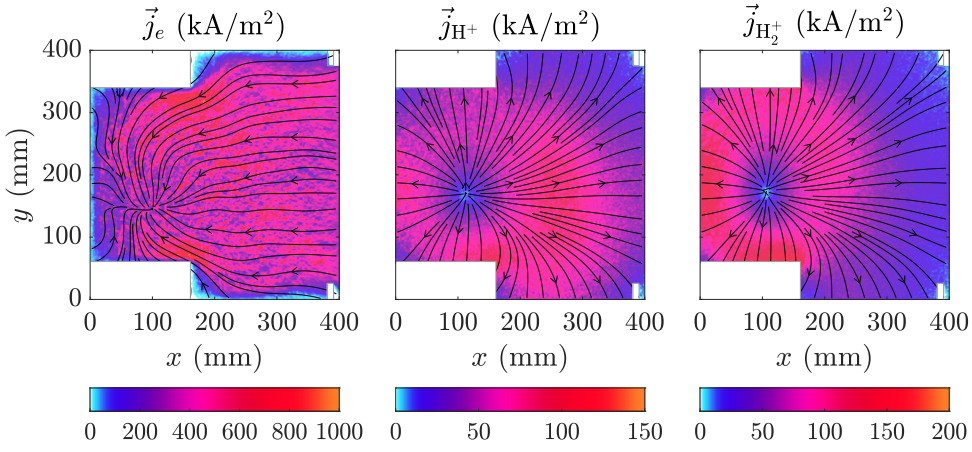

Figure 5.15: No filter field: e^-, H^+ and H_2^+ current direction and intensity.

As fast electrons can destroy H anions through dissociative attachment (see Section 2.2.2), the fraction of negative ions is considerably reduced with respect to previous cases. Figure 5.16 shows the plasma composition obtained in the absence of the magnetic filter field, compared with the same results provided by the magnetised regime.

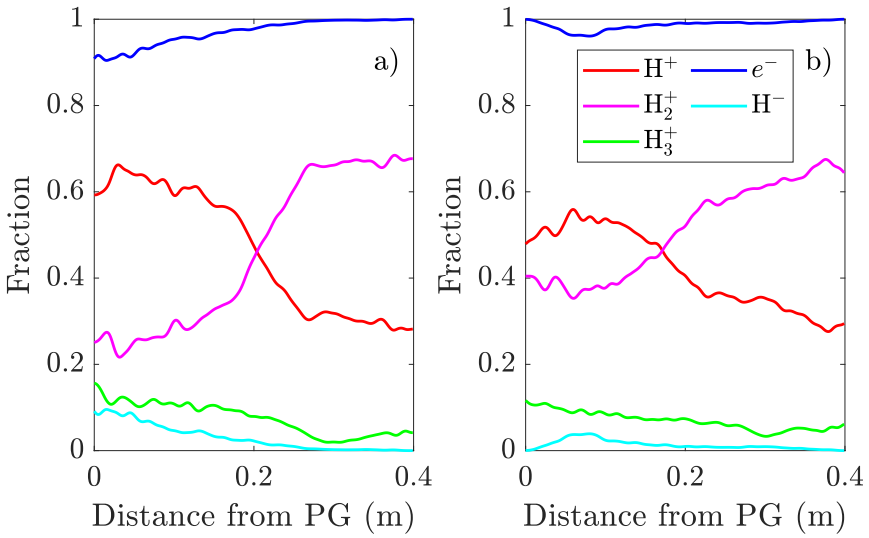

Figure 5.16: Comparison between plasma composition obtained in the magnetised (a) and unmagnetised (b) regimes.

Trajectories

Figure 5.17 shows two sample e^- trajectories. In the magnetised case, the projection on the simulation plane of the gyration motion along the field lines is visible, whereas in the unmagnetised case the e^- motion is driven by the electrostatic and collisional forces.

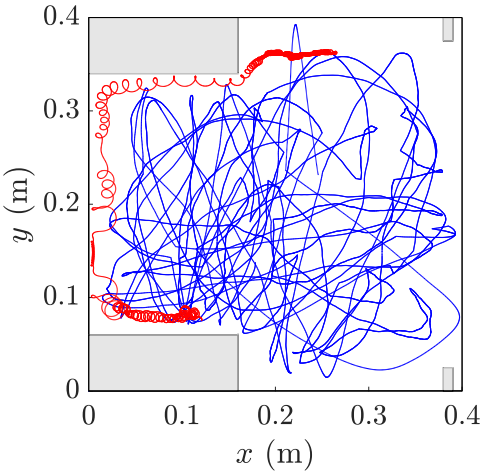

Figure 5.17: e^- trajectories with (red) and without (blue) $\vec{B}_{filt}$.

Chapter conclusion

The numerical results obtained with the `gppic` simulation code and their comparison with the experimental data measured in the SPIDER source have been discussed in this chapter. Three different cases were considered, namely:

- Low and high pressure regimes;
- Low and high plasma grid and bias plate voltages;
- With and without magnetic filter field.

An accurate comparison between the simulated and measured plasma properties was performed only for the first case, whereas a qualitative analysis was provided for the others. The numerical results are overall comparable with the experimental ones, in spite of some major differences between the simulated and real systems. As expected, the plasma asymmetry was found to be related to the drift motions arising because of the magnetic filter field. Some further information on the plasma currents and on plasma composition was deduced.

Chapter 6

Conclusions

A numerical model for the investigation of RF negative ion sources for fusion applications was developed in this thesis work. The simulation code was applied to reproduce the experimental results measured in SPIDER, with the aim of analysing the plasma generation and expansion mechanisms.

The experimental trends were reproduced with good accuracy, despite some relevant differences between the simulated system and the real source: the numerical analysis was based on hydrogen discharges, whereas the measured data were obtained from a deuterium plasma. This undoubtedly introduces some isotope effects which, for instance, might partially account for the discrepancy between the real and simulated filling pressures.

As expected, the plasma behaviour was found to be qualitatively analogous in the low and high pressure regimes: the plasma currents have both comparable intensity and topology, the electron density and temperature profiles have similar shapes. A relevant difference was found in the plasma composition: both the H^- and H^+ densities have increased in the high pressure regime. The growth of the negative ion population can only be related to the increase of the background gas density, that implies higher collision rates, as only volume production was considered in this model. Regarding the H^+ ions increase, there are several possible explanations: for instance, the electron temperature might have reached a value low enough to considerably reduce the H_2 ionization rate, thus decreasing the fraction of molecular ions both inside the driver and in the expansion chamber.

The simulation response to variations of the filter field is completely comparable to the experimental one: in the unmagnetised case, the plasma density decreases as electrons are no longer confined inside the driver, and T_e becomes approximately constant in the whole domain. The plasma composition is not very different between the magnetised and unmagnetised regimes, apart from a difference in the negative ion density. The ion currents are unvaried, whereas the electron current becomes more symmetric. As far as the filter field is concerned, it is worth

noticing that the implemented field profile is not equal to the experimental one in a specific plasma cross-section: this choice was unavoidable as the field gradient inside the driver was found to compromise the simulation stability. This might also explain why the simulated n_e profiles are always slightly more pronounced than the measured ones: by reducing the field intensity at the driver exit, the confinement has inevitably worsened. In future works, it might be interesting to analyse these instabilities on a deeper level, with the aim of understanding whether they can be related to a specific physical phenomenon.

The magnetic filter field inside the driver was set to a non-zero value: this is an important difference between the `gppic` code and the ones used in previous works. By doing so, a more accurate description of the e^- motion inside the driver was provided: more precisely, the electrons seem to follow a circular path on the simulation plane, while gyrating around the field lines. Such behaviour will be much more complex in a three-dimensional topology, and it could be useful to verify if it is also present in the real source, for instance by using movable electrostatic probes.

Finally, the low and high plasma grid and bias plate voltage regimes were investigated: the simulation well reproduces the real source behaviour, even though the obtained electron densities, temperatures and the plasma potential are not directly comparable. In particular, the electron density increases in the expansion chamber for higher values of both the PG and BP voltages, as the plasma potential is now lower than the wall potential. However, it is worth pointing out that this effect might be enhanced by the geometry of the simulation domain, in which the upper and lower surfaces are much closer than in the real source. The electron temperature instead decreases, possibly because fast electrons are lost at the surface. The plasma composition in the few centimeters before the plasma grid is strongly affected by the PG bias, so that when its potential is set at 43 V the negative ions account for almost 90% of the total negatively charged population; the fraction of heavy H_3^+ ions has also increased.

In all cases shown in Chapter 5, the main channel for plasma generation was the ionization of molecular hydrogen by impact of fast electrons. However, this result might be affected by the choice of both the dissociation degree and background gas density profile. In real sources, the fraction of dissociated H atoms is not expected to be constant in the whole volume, as it might depend on the plasma density. On this basis, one might argue that a non-constant dissociation degree could possibly lead to a different plasma composition. Furthermore, the chosen n_{bg} profile might be improved on the basis of experimental evidence, as this would provide a more accurate description of the discharge sustainment.

Because of drift motions, the plasma expansion was found to be strongly asymmetric with respect to the driver axis. While flowing out of the driver, a fraction of fast electrons manages to cross the filter field and reach the expansion chamber bu they are pushed upwards by the diamagnetic drift, which reaches its maximum intensity exactly at the driver exit, where the density gradient is larger. This ex-

plains why the two-dimensional T_e maps display a tail towards the upper part of the domain in the magnetised case. The electron density seems to be shifted away from the lower surface, resulting in a non complete filling of the expansion chamber. When analysing the discharge expansion, it is possible to see that the plasma somehow "rotates" from the upper to the lower region, as briefly shown in Figure 4.13. The direct consequence of the drift motions is that the plasma is not uniformly distributed in front of the plasma grid surface.

To conclude, there are several ways to improve the PIC code used in this thesis work. First of all, the description of the plasma-gas and plasma-plasma interactions can be further expanded by including all possible Coulomb processes and by adding any missing low-energy collisions for the electrons, as the latter might be the reason why the simulated T_e is never lower than 2 eV. The problems regarding the plasma potential inside the driver should also be addressed, as the simulated potential is significantly lower than the measured one. This might be related to the missing description of the inductive coupling, because the potential profile strongly depends on the electron temperature at the walls, as shown in Section 4.2.1. The measured electron temperature can be thought of as the result of the radiofrequency heating and of thermalization processes, thus implying that the actual temperature in the proximity of the driver walls might be even higher than the central one. The simulation instead manages to reach the experimental T_e value through the PI controller, but no information is given on the radiofrequency heating and this might ultimately result in an underestimation of the plasma potential.

The PI control was found to be extremely useful for reproducing the experimental trends. It only requires two boundary conditions, namely the n_e and T_e values at the driver center, and it allows to vary the background gas density and the frequency of the thermostat action to match these target values. In future works, the electron density convergence might be improved by fine-tuning the correction coefficients and, if necessary, by including the derivative contribution. The thermostat might be better exploited too, by implementing a more appropriate probability distribution so as to take the skin effect into account, for instance.

Some additional processes such as the surface production of negative ions and the neutralization and secondary emission at the vessel surfaces could be included with the purpose of comparing the simulation results also with measurements obtained while operating with caesium. A deeper analysis of the influence of the cusp magnetic field at the driver back-plate can be provided with a view to improving the implemented field profile.

Finally, the plasma grid apertures and, possibly, the extraction grid can be implemented: this would be extremely useful for providing the proper boundary conditions to submodels of smaller scale, focused on the extraction mechanism in the proximity of the PG aperture. This in turn could allow to correlate the plasma properties inside the driver with the extracted ion current.

Appendix A

Inductive coupling and skin depth effect

The skin depth parameter δ can be estimated by combining the Faraday and the Ampère-Maxwell equations as follows:

$$\begin{aligned} \nabla \times \nabla \times \vec{E} &= -\frac{\partial}{\partial t}\left(\nabla \times \vec{B}\right) \\ \nabla\left(\nabla \cdot \vec{E}\right) - \nabla^2 \vec{E} &= -\frac{\partial}{\partial t}\left(\mu_0 \vec{j} + \mu_0 \varepsilon_0 \frac{\partial \vec{E}}{\partial t}\right) \\ \nabla^2 \vec{E} &= \mu_0 \sigma_p \frac{\partial \vec{E}}{\partial t} + \mu_0 \varepsilon_0 \frac{\partial^2 \vec{E}}{\partial t^2} \end{aligned} \tag{A.1}$$

In a one-dimensional problem, the electric field can be defined as a plane wave

$$E = E_0\, e^{i(kx - \omega t)} \tag{A.2}$$

and by substituting A.2 in A.1 the dispersion relation is obtained

$$k^2 = \varepsilon_0 \mu_0 \omega^2 \left(1 + \frac{\omega_{pe}^2}{\omega} \frac{1}{\omega - i\,\nu_c}\right) \tag{A.3}$$

According to the ratio between ω and the collision frequency ν_c, two solutions can be identified. If $\omega \gg \nu_c$, also called *un-collisional* regime, one obtains

$$k = \pm i \frac{\omega_{pe}}{c} \tag{A.4}$$

where $c = 3 \times 10^8\,\mathrm{m/s}$ is the speed of light. On the other hand, if $\omega \ll \nu_c$ the *collisional* regime is considered and the wave vector is

$$k^2 = \varepsilon_0 \mu_0 \omega^2 \left(1 + i \frac{\omega_{pe}^2}{\omega\, \nu_c}\right) \tag{A.5}$$

In the un-collisional regime, the wave vector is a purely imaginary number and the electric field will propagate as

$$E = E_0\, e^{-\omega_{pe} x/c}\, e^{-i\omega t} = E_0\, e^{-x\delta}\, e^{-i\omega t} \tag{A.6}$$

that is a time-oscillating function, modulated by an exponential decay. The electrostatic energy carried by the wave is proportional to $|E|^2$, and the absorbed energy will be

$$\begin{aligned} \Delta\mathcal{E} &= \int_0^r dx\ |E(x)|^2 - a\,|E(a)|^2 \\ &\propto \int_0^r dx\, e^{-2x/\delta} - a\, e^{-2a/\delta} \\ &= \frac{\delta}{2}\left(1 - e^{-2a/\delta}\right) - a\, e^{-2a/\delta} \\ &= a\left(\frac{\delta}{2a} - \left(1 + \frac{\delta}{2a}\right) e^{-2a/\delta}\right) \end{aligned} \tag{A.7}$$

and it will be maximized when $\delta \approx a$, that is when the skin depth is approximately equal to the system characteristic dimension. It is important to point out that these results are verified in the un-collisional regime, that is when the heating frequency is much higher than the collision frequency. If instead collisions are not negligible, the skin depth parameter is defined as

$$\delta = \sqrt{\frac{2m_e\,\nu_c}{\mu_0 e^2 n_e \omega}} \tag{A.8}$$

where m_e, n_e and e are the electron mass, density and charge respectively. The difference between collisional and un-collisional regimes can be explained as follows[33]: the characteristic time for the electron to be heated by the RF coupling can be defined as

$$\tau_e = \frac{\delta}{v_e^{avg}} \tag{A.9}$$

where v_e^{avg} is the average electron velocity. If the RF oscillation period T_{RF} is much smaller than τ_e, the electron will be heated before undergoing any collisions. In this case, the heating mechanism can be assumed to take place in a non-collisional RF sheath. On the other hand, if $T_{RF} \gg \tau_e$, a poloidal current will flow in the plasma and the electron heating will take place mainly through collisions with neutrals. These two regimes are referred to as *stochastic* and *ohmic* heating respectively. In the first case, non-local kinetic effects have to be considered as the electrons will acquire a net velocity along the electric field direction; as a result, the EEDF will follow a non-maxwellian distribution. On the other hand, ohmic heating and $e^- - e^-$ Coulomb scattering counterbalance the non-local heating by redistributing the acquired energy. An effective collision frequency ν_m can be defined as the sum of the aforementioned contributions[34].

Appendix B

Collision rates

Of particular interest is the determination of the collision rates for each single process, as this serves to both validate the adopted implementation methods and to identify the most relevant interactions for the plasma formation and sustainment. Generally speaking, the most probable processes between plasma particles and the background gas are elastic scattering and momentum transfer. As already stated in Chapter 4, the dominant plasma generation channel is the (e^-, H_2) ionization, which requires energetic electrons.

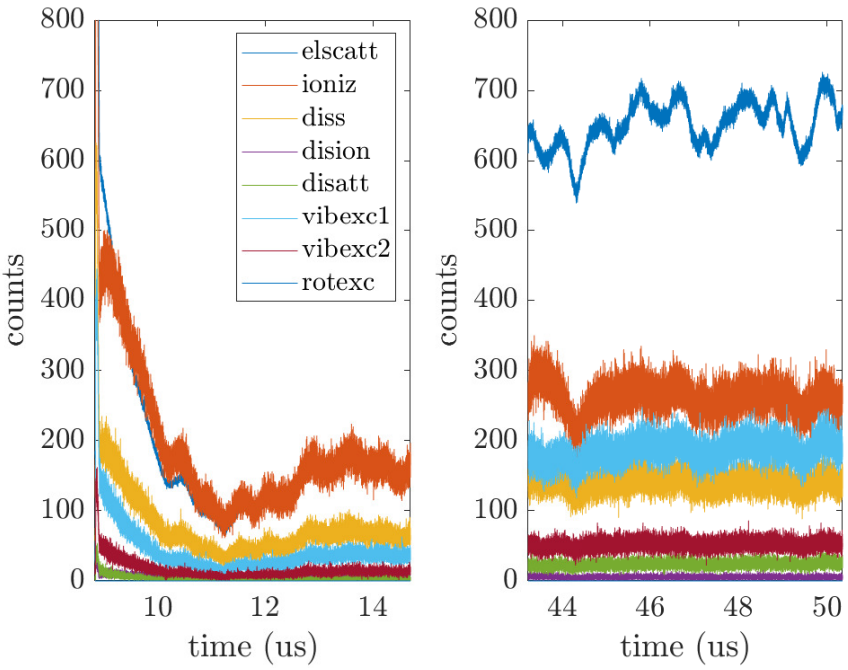

Figure B.1: (e^-, H_2) collisions rates for the low (left) and high (right) pressure regimes.

Figure B.1 shows the collision rates for all the electron impact processes on molecular hydrogen in both the low and high pressure regimes. The initial decrease in the left figure is related to the PI control effect. As one would expect, all the interactions are more probable in the high pressure regime, as n_{bg} is higher. The same trend can be observed for all the collision rates.

In order to understand whether the simulation has reached a stationary state, the net difference between the newly generated and lost MP can be estimated. Figure B.2 shows this "effective" generation rate as a function of the iteration number.

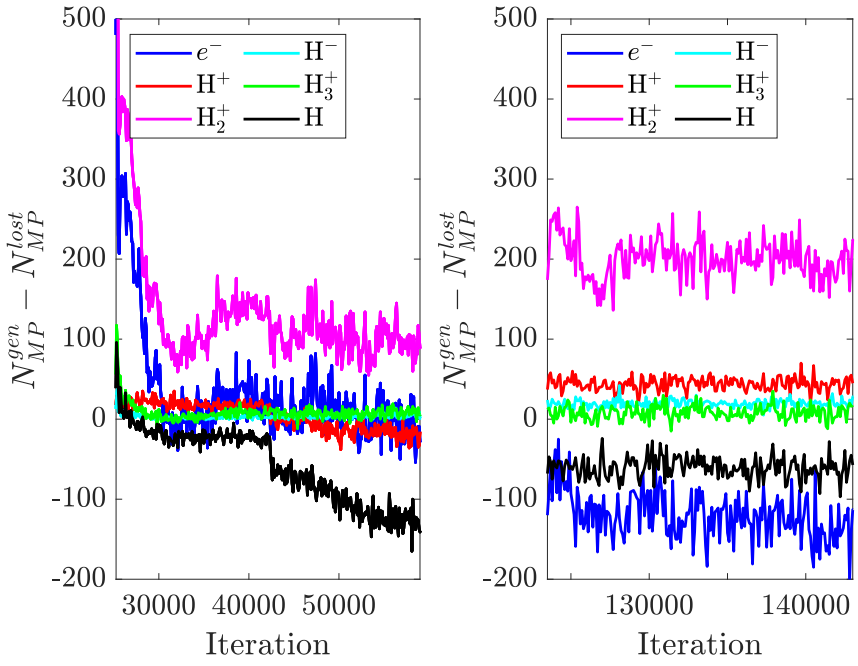

Figure B.2: Effective generation rates for the low (left) and high (right) pressure regimes.

In the low pressure regime, the generation rate of both e^- and H_3^+ cations converges to 0, thus implying that the same amount of macroparticles is produced and lost at each iteration. On the other hand, the loss term prevails for both H and H^+: in the first case, the comments on fast atoms generation from Chapter 4 should be taken into account. Speaking of protons, instead, this effect can arise for different reasons: for instance, there might be some important missing processes. Furthermore, it is important to point out that wall neutralization is not included in the simulations. The high pressure regime rates are overall similar, even though in this case the e^- generation rate is constantly negative, whereas the proton generation rate is slightly positive. In both cases, the H_2^+ rate is significantly larger than all the other ones: this might be sign of some missing destruction channel for heavy positive ions.

Appendix C

Drift motions analysis

This appendix provides a more detailed analysis on the drift motions arising in the source. Three contributions can be distinguished, namely the $\vec{E} \times \vec{B}$ drift, the diamagnetic drift and the $\vec{B} \times \nabla \vec{B}$ drift. These phenomena are the main causes for plasma asymmetry. At first, the intensity and direction of the e^- drift velocities can be analysed by retracing the three contributions on the basis of `gppic` results. Figures C.1, C.2 and C.3 show all three drifts averaged over 100 iterations.

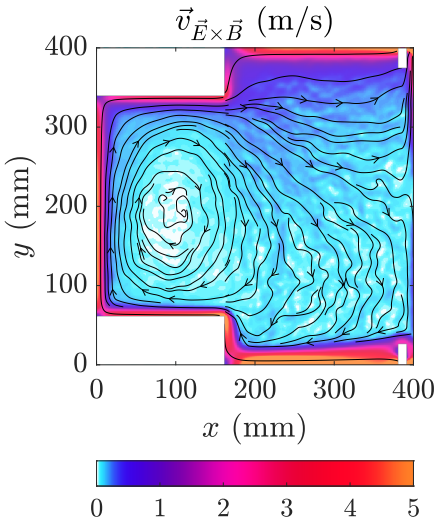

Figure C.1: $\vec{E} \times \vec{B}$ drift streamlines and intensity.

The $\vec{E} \times \vec{B}$ and diamagnetic drift intensities are similar and they are both higher in the proximity of the walls, as the local $\vec{E}$ and ∇p are enhanced. The average drift velocity is less than 0.5 m/s. Speaking of the $\vec{E} \times \vec{B}$ drift, the streamlines form a vortex inside the driver and, furthermore, they are significantly asymmetric in the

expansion chamber; it is worth pointing out that the same asymmetry can be seen in the electron density maps shown in Chapter 5. The electron diamagnetic drift direction is roughly opposite with respect to the $\vec{E} \times \vec{B}$ one.

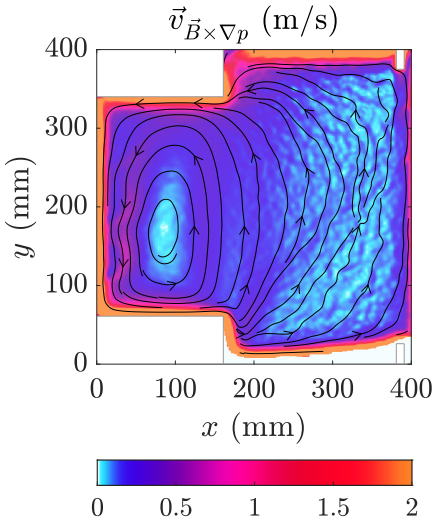

Figure C.2: Diamagnetic drift streamlines and intensity.

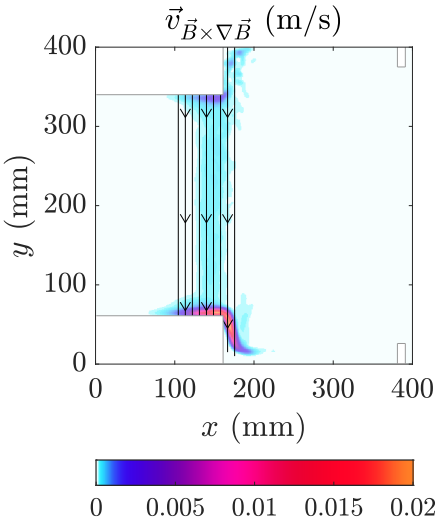

Figure C.3: $\vec{B} \times \nabla\vec{B}$ drift streamlines and intensity.

Finally, the $\vec{B} \times \nabla\vec{B}$ drift is directed along the y direction and it arises because of the magnetic field gradient. This contribution is opposed to the diamagnetic drift one and it is localized in the driver exit region.

In order to determine which one is the dominant contribution, the net drift

velocity can be calculated. To do so, both the x and y components of the electron drift velocities along two vertical paths at $x = 185\,\text{mm}$ and $x = 395\,\text{mm}$ and one horizontal path at $y = 200\,\text{mm}$ are estimated and compared.

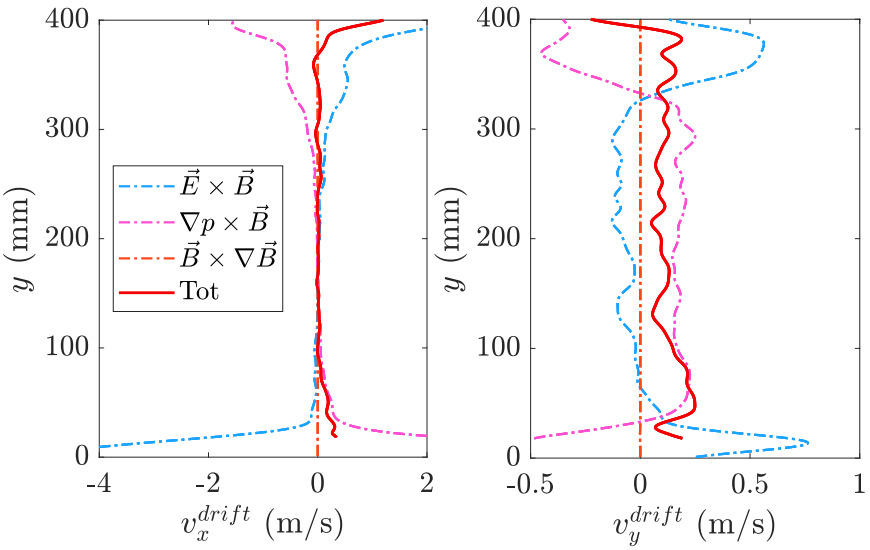

Figure C.4: Electron drift velocities components along a vertical line centered at $x = 185\,\text{mm}$.

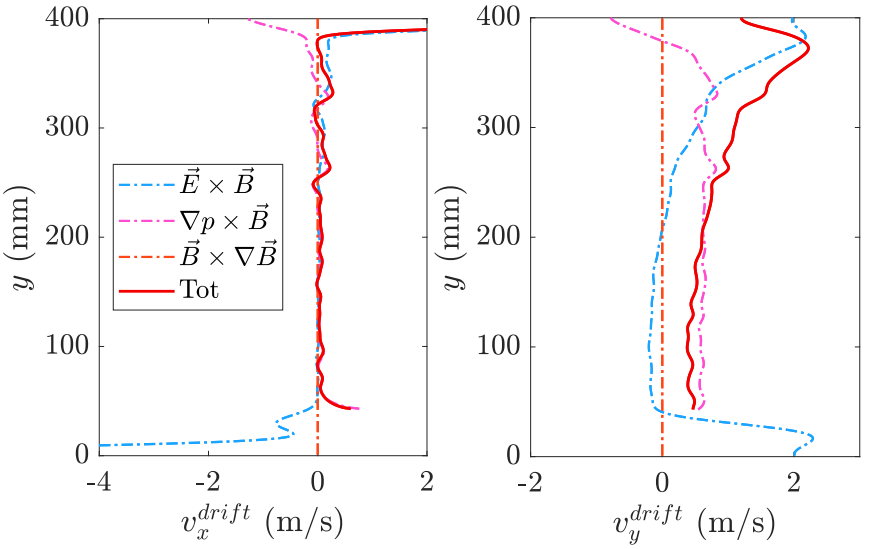

Figure C.5: Electron drift velocities components along a vertical line centered at $x = 395\,\text{mm}$.

As can be seen from Figure C.4, there is a considerable vertical drift at the driver

exit, almost completely given by the diamagnetic drift. There is no net motion along the x direction, with the exception of the lower and upper sections: in the first case, the $\vec{E}\times\vec{B}$ drift is dominant, whereas in the second case the diamagnetic drift prevails on the $\vec{E}\times\vec{B}$ one. The same phenomenology holds for the $x = 395\,\text{mm}$ too, even though the vertical drift is almost twice as intense.

The vertical component of the $\vec{E}\times\vec{B}$ drift velocity changes direction in both cases: this variation can be only related to the local electric field, as the magnetic filter field is always directed along the z direction. Furthermore, the diamagnetic drift seems to stop abruptly for $y < 25\,\text{mm}$; this effect can be related with the electron density asymmetry, as can be seen from Figure 5.5.

To conclude this appendix, Figure C.6 shows the drifts components estimated along a horizontal line centered at $y = 200\,\text{mm}$. The electrons are drifting towards the expansion chamber, even though there is a significant region of space in which they tend to travel back into the driver: this might be due to the presence of the magnetic filter, which restrains fast electrons from approaching the expansion region. The y component of the drift velocity changes sign in the driver, possibly as a consequence of the vortex motion. The vertical diamagnetic drift can also be seen at $x \approx 180\,\text{mm}$, as expected. Electrons are finally accelerated in the proximity of the plasma grid.

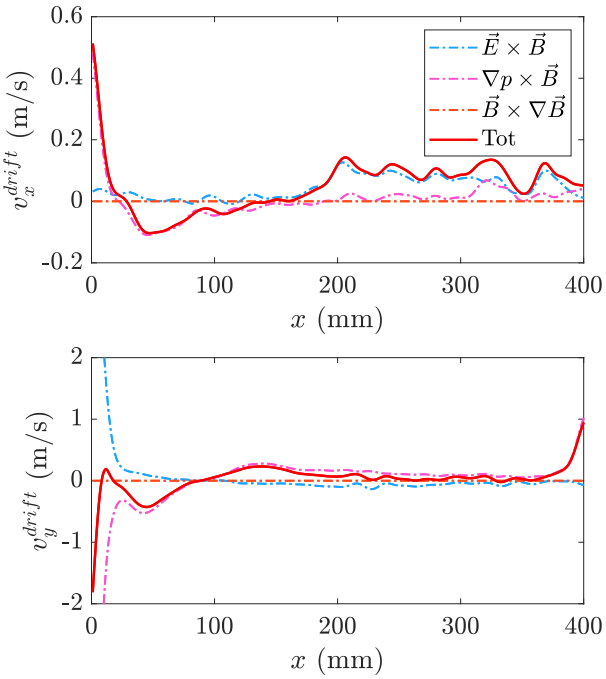

Figure C.6: Electron drift velocities components along a horizontal line centered at $y = 200\,\text{mm}$.

Bibliography

[1] BP Statistical Review of World Energy. URL: https://www.bp.com/en/global/corporate/energy-economics/statistical-review-of-world-energy.

[2] European Space Agency. URL: https://www.esa.int/Applications/Observing_the_Earth/Copernicus/Sentinel-5P/Air_pollution_remains_low_as_Europeans_stay_at_home.

[3] ITER organization. URL: http://www.iter.org.

[4] L. M. Giancarli et al. "Overview of the ITER TBM Program". In: *Fusion Engineering and Design* 87 (2012), pp. 395–402. DOI: https://doi.org/10.1016/j.fusengdes.2011.11.005.

[5] M. Kikuchi et al. "Fusion Physics". In: International Atomic Energy Agency, 2012.

[6] V. Toigo et al. "Overview of the ITER TBM Program". In: *New J. Phys.* 19.085004 (2017). DOI: https://doi.org/10.1088/1367-2630/aa78e8.

[7] D. Rauner et al. "Influence of the extraction frequency on the RF power transfer efficiency of low pressure hydrogen ICPs". In: *Plasma Sources Sci. Technol.* 28.095011 (2019). DOI: https://doi.org/10.1088/1361-6595/ab3d6a.

[8] N. Braithwaite P. Chabert. "Physics of Radio-Frequency Plasmas". In: Cambridge University Press, 2011.

[9] P. McNeely et al. "A Langmuir probe system for high-power RF-driven negative ion sources on high potential". In: *Plasma Sources Sci. Technol.* 18.014011 (2009). DOI: https://doi.org/10.1088/0963-0252/18/1/014011.

[10] F. Taccogna et al. "Modeling of negative ion source. I. Gas kinetics and dynamics in the expansion chamber". In: *Phys. Plasmas* 14.073503 (2007). DOI: https://doi.org/10.1063/1.2752514.

[11] J.P. Boeuf G. Fubiani L. Garrigues. "Modeling of negative ion extraction from a magnetized plasma source: Derivation of scaling laws and description of the origins of aberrations in the ion beam". In: *Physics of Plasmas* 25.023510 (2018). DOI: https://doi.org/10.1063/1.4999707.

[12] P. Franzen et al. "Performance of multi-aperture grid extraction systems for an ITER-relevant RF-driven negative hydrogen ion source". In: *Nucl. Fusion* 51.073055 (2011). DOI: https://doi.org/10.1088/0029-5515/51/7/073055.

[13] K. Miyamoto et al. "Analysis of the beam halo in negative ion". In: *Rev. Sci. Instrum.* 87.02B124 (2016). DOI: https://doi.org/10.1063/1.4932390.

[14] P. Veltri. “Physics of negative ion extraction and acceleration in neutral beam injectors”. In: PhD thesis, 2010.
[15] R. S. Hemsworth and T. Inoue. “Positive and Negative Ion Sources for Magnetic Fusion (invited paper)”. In: *IEEE Transactions on Plasma Science* 33.6 (2005).
[16] Y. Haba et al. “Response of beam focusing to plasma fluctuation in a filament-arc-type negative ion source”. In: *Jpn. J. Appl. Phys.* 59.SHHA01 (2020). DOI: https://doi.org/10.35848/1347-4065/ab7473.
[17] G. Serianni et al. “First operation in SPIDER and the path to complete MITICA”. In: *Rev. Sci. Instrum.* 91.023510 (2020). DOI: https://doi.org/10.1063/1.5133076.
[18] R. Pasqualotto et al. “Diagnostics of the ITER neutral beam test facility”. In: *Rev. Sci. Instrum.* 83.02B103 (2012). DOI: https://doi.org/10.1063/1.3662017.
[19] D. Marcuzzi et al. “Detail design of the beam source for the SPIDER experiment”. In: *Fusion Engineering and Design* 85 (2010), pp. 1792–1797.
[20] P. Sonato et al. “The ITER full size plasma source device design”. In: *Fusion Engineering and Design* 84 (2009), pp. 269–274.
[21] C. K. Birdsall and A. B. Langdon. “Plasma Physics via Computer Simulation”. In: Adam Hilger, 1991.
[22] T. Maceina. “GPGPU application in fusion science”. In: PhD thesis, 2017.
[23] J. P. Boris. “Relativistic plasma simulation-optimization of a hybrid code”. In: *Proceedings of the Fourth Conference on Numerical Simulation of Plasmas* 2.3 (1970), pp. 3–67.
[24] F. Taccogna and P. Minelli. “PIC modeling of negative ion sources for fusion”. In: *New J. Phys.* 19.015012 (2017). DOI: https://doi.org/10.1088/1367-2630/aa5305.
[25] CUDA. URL: https://developer.nvidia.com/cuda-zone.
[26] V. Vahedi and M. Surendra. “A Monte Carlo collision model for the particle-in-cell method: applications to argon and oxygen discharges”. In: *Computer Physics Communications* 87 (1995), pp. 179–198.
[27] U. Samm R.K. Janev D. Reiter. “Collision processes in Low-Temperature Hydrogen Plasmas”. In: EIRENE database, 2003.
[28] H. C. Straub et al. “Absolute partial cross sections for electron-impact ionization of H2, N2 and O2 from threshold to 1000 eV”. In: *Phys. Rev. A* 54.2146 (1996).
[29] K. Nanbu. “Theory of cumulative small-angles collisions in plasmas”. In: *Physical Review E* 55.4 (1997).
[30] R. Cattolica M. Shimada G. R. Tynan. “Neutral gas density depletion due to neutral gas heating and pressure balance in an inductively coupled plasma”. In: *Plasma Sources Sci. Technol.* 16 (2007), pp. 193–199. DOI: https://doi.org/10.1088/0963-0252/16/1/024.
[31] J.P. Boeuf et al. “Physics of a magnetic filter for negative ion sources. II. ExB drift through the filter in a real geometry”. In: *Phys. Plasmas* 19.113510 (2012). DOI: https://doi.org/10.1063/1.4768804.

[32] G. Fubiani et al. “Modelling of plasma transport and negative ion extraction in a magnetized radio-frequency driven source”. In: *New J. Phys.* 19.015002 (2017). DOI: https://doi.org/10.1088/1367-2630/19/1/015002.

[33] M.A. Lieberman et al V. Vahedi. “Analytic model of power depostion in inductively coupled plasma sources”. In: *Journal of Applied Physics* 78.1446 (1995). DOI: https://doi.org/10.1063/1.360723.

[34] M. A. Lieberman and A. J. Lichtenberg. “Principles of Plasma Discharges and Materials Processing”. In: John Wiley and Sons, 2005.

[35] P. McNeely et al. “Neutral depletion in an H- source operated at high RF power and low input gas flow”. In: *Plasma Sources Sci. Technol* 20.045005 (2011). DOI: https://doi.org/10.1088/0963-0252/20/4/045005.